ANALYSIS OF DEFORMATION AND FAILURE IN ALUMINUM TUBE UNDER INTERNAL PRESSURE

ANALYSIS OF DEFORMATION AND FAILURE IN ALUMINUM TUBE UNDER INTERNAL PRESSURE

By YIHAI, SHI, M. ENG.

A Thesis Submitted to the School of Graduate Studies
in Partial Fulfilment of the Requirements for the Degree
Doctor of Philosophy
in Mechanical Engineering

McMaster University

Doctor of Philosophy in Mechanical Engineering (2013)

McMaster University, Hamilton, Ontario

TITLE: ANALYSIS OF DEFORMATION AND FAILURE IN ALUMINUM TUBE UNDER INTERNAL PRESSURE

AUTHOR: Yihai, Shi, M. Eng. (McMaster University)

SUPERVISOR: Professor P. D. Wu

NUMBER OF PAGES: xviii, 152

Abstract

The objective of this research is to develop an understanding of the mechanical behavior, failure and microstructure evolution of aluminum tubes under internal pressure loading, and to delineate the physical and mechanical origins of spatially-localized plastic deformation. Traditional approaches to the study of plastic instabilities, necking and failure have either been based on kinematic considerations, such as finite strain effects and geometric softening, or physics-based concepts. In this study, we develop a framework that combines both approaches to investigate the tube deformation and failure behavior at various loading conditions.

A rate-dependent dislocation-based MTS model has been developed to study the tube hydro-forming process at high temperatures and at various strain rates. The development and application of the MTS model led to an advanced industrial application of PRF bottle forming, which has been fully investigated. This simulation shows a good agreement between experimental results and prediction. The model has been used extensively throughout the PRF bottle development, with several patent applications.

The crystal plasticity based finite element model is selected to simulate surface roughening and localized necking in aluminum alloy tubes under internal pressure. The measured electron backscatter diffraction (EBSD) data are directly incorporated into the finite element model and the constitutive response at an integration point is described by the single crystal plasticity theory. The effects of the spatial grain orientation distribution, strain rate sensitivity, work hardening, and initial surface topography on surface roughening and necking are discussed. It is demonstrated that while localized necking is very sensitive to both the initial texture and its spatial orientation distribution, the initial surface topography has only a small influence on necking, but a large influence on surface roughness of the formed product.

An elastic-viscoplastic based finite element model has been developed to study the necking behavior of tube expansion for rate dependent monolithic materials and laminated materials during dynamic loading. Numerical study shows that a high strain rate sensitivity can significantly delay the onset of necking for both monolithic and laminated sheets, and affect the multiple-neck formation in high speed dynamic loading. The model also shows that higher volume fractions of a clad layer with positive rate sensitivity material in laminated sheet could improve the sheet ductility as well.

A commercial FE package, ABAQUS, is employed as a finite element method solver in this research work, and several user subroutines were developed to model various hydro-forming processes. Interfaces between the ABAQUS user subroutine UMAT and the ABAQUS main code are developed to allow further extension of the current method.

Acknowledgements

Firstly, I would like to thank my advisor Professor Peidong Wu for his guidance, insight, kindness and patience. His continuous encouragement and enthusiasm helped me overcome many difficulties. Without his direction, I would not have been able to complete this project. Indeed, I am very fortunate and grateful to have worked with him in this stage of my education.

Special thanks are extended to Dr. Stuart MacEwen, Dr. David Lloyd and Dr. Mark Gallerneault from Novelis Global Technology Center for their support and valuable contributions to this research.

Lastly, I would like to thank my family for their love and support throughout this challenging work.

Financial support for this research was provided by Novelis Global Technology Center, Novelis Inc..

Table of Contents

List of Figures

List of Tables

Table Page

List of Symbols

1. Symbols used in general constitutive equations for inelastic deformation

$\boldsymbol{\sigma}$: Cauchy stress

$\overset{\nabla}{\boldsymbol{\sigma}}$: Jaumann stress

$\mathbf{E}$: Total strain

$\mathbf{p}$: Surface load

$\mathbf{q}$: Volume load

$\mathbf{F}$: Total deformation gradient

$\mathbf{F}^*$: Elastic deformation gradient

$\mathbf{F}^\mathbf{p}$: Plastic deformation gradient

$\mathbf{R}$: Rigid body rotation

$\mathbf{V}$: Left stretch matrix

$\mathbf{U}$: Right stretch matrix

$\mathbf{L}$: Velocity gradient

$\mathbf{A_0}$: Initial configuration of deformation system

$\mathbf{A}$: Final configuration of deformation system

$\dot{\boldsymbol{\varepsilon}}$: Total strain rate

$\dot{\boldsymbol{\varepsilon}}^\mathbf{el}$: Elastic strain rate

$\dot{\boldsymbol{\varepsilon}}^\mathbf{P}$: Inelastic strain rate

ε^{pl} : Effective plastic strain

$\overline{\sigma}$: Effective stress

Δt : Time increment

μ : Lamé constant

λ : Lamé constant

G : Shear modulu

r^{pl}: Plastic deformation results in a heat flux
$\mathbf{s}^{*}$: State variable
$\mathbf{F}_{\mathbf{r}}$: Relative deformation gradient
$\mathbf{V}_{\mathbf{r}}$: Increment of the stretch matrix computed from the polar decomposition of $\mathbf{F}_{\mathbf{r}}$
$\boldsymbol{\sigma}_{\mathrm{trial}}^{\mathrm{n+1}}$: Trial stress
$\mathbf{S}$: Deviatoric stress
$\mathbf{n}$: Flow direction
$\mathbf{M}$: Tangent stiffness
$\mathbf{J}$: Jacobian matrix
$\mathbf{R}_{a}$: Residual of non-linear constitutive equations

2. Symbols used in the MTS model

$\hat{\sigma}$: Mechanical threshold strength
$\dot{\varepsilon}$: Strain rate
T: Temperature
μ_0: Shear modulus at 0 K
k: Boltzmann’s constant
b: Burgers vector
μ_d: Material constant
T_0: Material constant
g_0: Material constant
$\dot{\varepsilon}_0$: Material constant
p : Material constant
m: Material constant
q : Material constant
$\widehat{\sigma}_s$: Saturation stress

θ_0 : Work hardening rate

σ_{at} : Athermal stress component

S_i : Scalar factor

S_ε : Scalar factor

3. Symbols used in crystal plasticity

φ_1 : Euler angle

φ : Euler angle

φ_2 : Euler angle

$\mathbf{D}$: Rate of total deformation tensors

$\mathbf{D^p}$: Rate of plastic deformation tensors

$\mathbf{D}^*$: Rate of elastic deformation tensors

$\boldsymbol{\Omega}$: Total spin rate

$\boldsymbol{\Omega}^{\mathbf{p}}$: Plastic spin rate

$\boldsymbol{\Omega}^*$: Elastic spin rate

$\mathbf{s}_{\boldsymbol{\alpha}}$: Slip direction

$\mathbf{m}_{\boldsymbol{\alpha}}$: Slip-plane normal

$\mathbf{I}$: Second order identical tensor

$\mathbf{L}$: Tensor of elastic moduli

τ^α : Schmid shear stress

g^α : Deformation resistance in this slip system

$\dot{\gamma}_0$: Reference shear rate

m : Strain-rate sensitivity index

$\dot{\gamma}^\beta$: Plastic incremental rate

ρ_0 : Mass density in the reference state

ρ : Mass density in the current state

q : Latent hardening parameter

τ_s : Hardening parameter

a : Hardening parameter

$h^{\alpha\beta}$: Rate of hardening effect on slip system α due to plastic increment on slip system β

4. **Symbols used in the rate depended elastic-viscoplastic model**

$\dot{\varepsilon}_0$: Initial strain rate

m : Rate sensitivity constant

s : Saturation stress

h_0 : Material parameter

α : Material parameter

s^* Material parameter

n : Material parameter

Chapter 1

Introduction

One topic of current interest to the aluminum sheet forming industry is hydroforming due to its ability to extend the range of formability of sheet. This forming operation provides significant advantages over the currently used D&I (draw and iron) processes (Koc et al. 2001). Fig. 1.1 shows the process for tube hydroforming. A tube is placed in the tool cavity, where the geometry of the die corresponds to the final geometry of the product. In most cases, the tooling is closed by the ram movement of the press. The tube ends are loaded by punches moving along the tube axis, normally the longitudinal direction. During the hydroforming process, internal pressure of the tube is increased until the expanding tube wall comes into contact with the inner surface of the die.

The benefit of numerical simulation of hydroforming is to replace the expensive and time-consuming experimental investigation and subsequent tests which are commonly used in this trial-and-error approach. The simulation of the hydroforming processes becomes especially relevant if the feasibility of metal forming processes has to be checked before expensive tooling is manufactured. In this sense, the finite element simulation can contribute to both understanding of the process, and assistance in process planning and feasibility. In order to accurately capture sheet metal deformation behavior under various forming conditions in the simulation, there is a growing need for more detailed understanding of the material response to loads and strains over loading periods of time, for the mechanical properties may evolve away from those achieved in the final forming step. It is therefore imperative to develop appropriate numerical tools to reliably predict the mechanisms of deformation and failure under hydroforming in order to fully explore its potential.

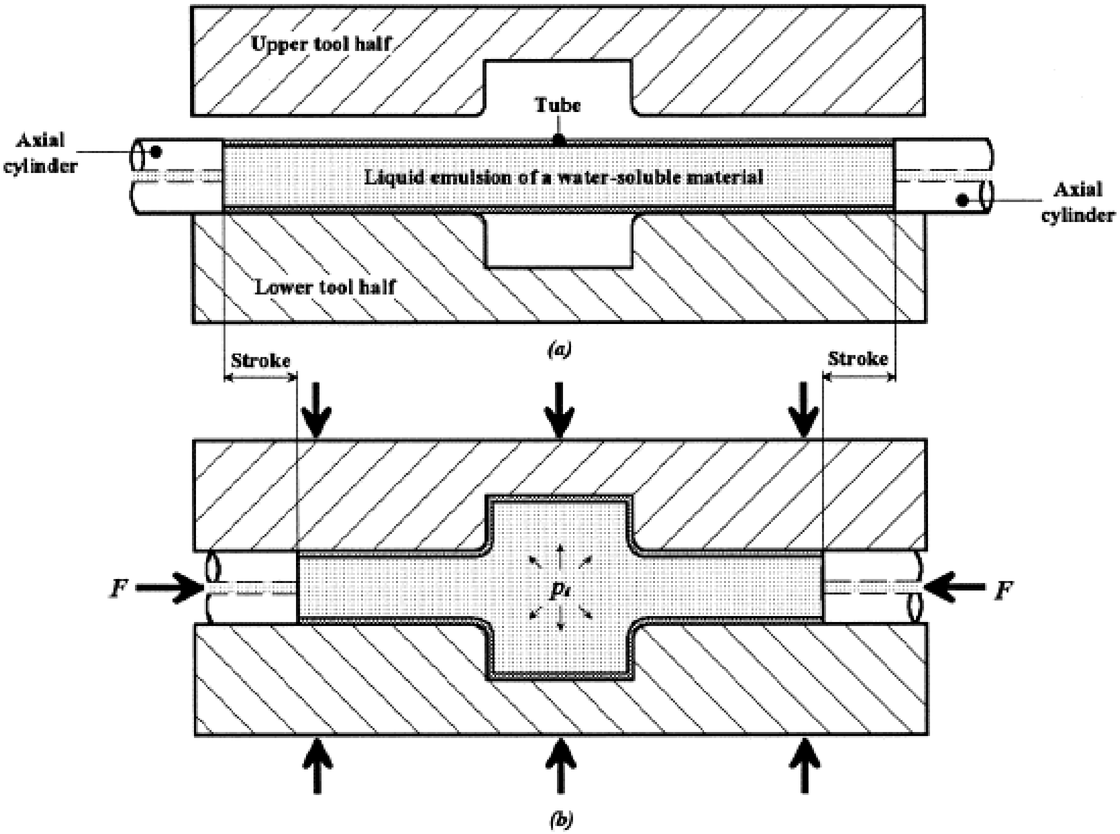

Figure 1.1 Process principle for tube hydroforming

There are many topics related to the hydroforming process in term of deformation and failure that remain to be studied. This research will focus on four major areas, which are directly related to the aluminum industrial interests and applications:

1) Hot/Warm hydroforming process with its application of PRF bottle forming.
2) Prediction of localized necking failure in aluminum tube during hydroforming.
3) Surface roughening analysis in aluminum tube on internal pressure.
4) Effect of rate sensitivity on necking behavior of tube under dynamic internal pressure loading.

As the industrial applications of hydroforming have expanded rapidly, the current study on the mechanism for deformation behavior at various forming conditions is far from complete; further research and contribution to a better understanding of these topics are the task of this thesis.

1.1 Literature review

1.1.1 Hot/Warm hydroforming process with its application of PRF bottle forming

The research of hot/warm hydroforming has been intensely studied in recent years, particular for aluminum alloys. Li and Ghosh (2003 & 2004) studied deformation behaviour of aluminum sheet alloys in the warm forming temperature range of 200°C to 350°C and in the strain rate range of 0.015-1.5 s^{-1}. They observed a significant improvement in biaxial warm forming at temperatures ranging from 200°C to 350°C. More specifically, they found that the formability of the aluminum sheet alloys formed at 250°C, in terms of the forming limit diagrams, are already comparable to those of A-K steels formed at room temperature. Guan (2006) studied the deformation behavior of aluminum extruded tubes under hydroforming with finite element analysis based on empirical data.

In order to capture the thermal and mechanical behavior of the metal deformation at high temperatures and high strain rates, a proper material model needs to be defined. This requires that phenomenological models reflect experimentation. The relations and material parameters will be correlated with from observations. A typical phenomenological material model accounting for the strain rate and temperature evolution is the well-known Johnson-Cook model (1983 & 1985), which has been extensively used in industrial applications.

Physically-based models utilize microscopic mechanics associated with different plastic deformation processes to derive corresponding relations between structure and mechanical performance. The microscopic physical process includes dislocation slip, climb, thermally-activated dislocation glide, grain boundary sliding, diffusion dislocation accumulation and annihilation, and so on. As an example, the Mechanical Threshold Strength (MTS) model, developed and progressively improved by Follansbee and Kocks (1988), Kocks and Mecking (2003), Maudlin et al. (1990) and Chen et al. (1998), describes the constitutive behavior at moderate stress levels and temperature ranges, in which slip is the main deformation process, and plastic deformation occurs by thermally activated dislocation glide. The theory of thermal activation provides a description of kinetics for mobile dislocation interacting with physical obstacles, i.e. forest dislocation, solute atoms and precipitates. The internal state variable is defined by a mechanical threshold, the flow stress at 0K, which is related to the density of obstacles. The physical basis for work hardening lies in the accumulation of stored dislocations. Kocks and Mecking (1998) provided a model for evolution of mechanical threshold to account for work hardening. Verdier et al. (1992) extended the MTS model of Kocks' type by introducing a new state variable to represent the dislocation structure, which provides a detailed explanation for microstructure evolution during recovery. A state variable model was developed by Bammann et al. (1990, 1993 & 1996) for finite inelastic deformation and damage. The total deformation is multiplicatively decomposed into elastic, plastic, damage and thermal portions. A two-defect model provided by Saimoto (1989) is also based on thermally activated flow. That model was developed for a material system with strong barriers and provides a reasonable explanation for the observation in stress evolution which is contradictory with the original thermal activation. Based on the theory of thermodynamics, in the work hardening model by Goerdeler and Gottstein et al. (2001) and by Roters et al. (2000), three microstructure state variables were applied to represent mobile dislocations, immobile dislocation in the cell interiors and immobile dislocations in the cell walls, respectively, and evolution equations for each portion are identified. The micromechanical consideration contributes to predict more precisely work hardening behavior. The physically-based state variable model presented by Ghosh (1980) incorporated specific micro-mechanisms of varied physical processes during inelastic deformation, such as strain hardening, recovery and boundary effects.

From the viewpoint of application, most models are developed for large strain deformations because many manufacturing processes for metals such as forging, sheet metal forming and rolling are associated with larger deformation. The MTS model is intended for bulk plastic flow, while Bammann's state variable model (1990 & 1993) is developed for finite inelastic deformation and damage. In applications of these models, elastic strain is often ignored for it is relatively small compared to the plastic strain. Some models do cover from small to large strains, such as the models by Ghosh (1980) and by Miller (1987). The former model was applied for uni-axial tensile, creep and cyclic loading; the later was for multi-axial plastic deformation, creep, anisotropic effect and a complex deformation history.

High temperature hydrofoming with aluminum sheet is a process involving large strain and a high strain rate under high temperature forming conditions. From this perspective, the MTS model provides a solid fundamental background to address this deformation behavior. In this thesis, a modified MTS model has been developed to simulate aluminum tube deformation under pressurization at a temperature range of 300°C to 400°C. Based on the understanding of existing models and experiments; this modified MTS model has the following requirements:

- This modified MTS model should be phenomenologically sound, with the capability to describe the transient process of aluminum sheet deformation at high temperatures and high strain rates,
- The material parameters should be identifiable through easily performed experiments,
- This material model will be easily implemented into FE codes with practical applications for industrial use without inherent computational difficulties.

In this work, this modified MTS model is investigated to describe the behavior of sheet forming under hydroforming loading at high temperatures. Its application to the Pressure Ram Forming (PRF) process has also been studied in detail.

1.1.2 Prediction of localized necking failure in aluminum tube during hydroforming

The failure of ductile cylindrical tubes under internal pressure has been studied experimentally and theoretically for many years (see e.g. Larsson et al. (1982); Kyriakides and Chang (1990); Korkolis and Kyriakides (2008); Kuwabara et al. (2005)). It has been generally accepted that failure in a pressurized elastic-plastic tube is usually initiated from a strong shear band inside a localized neck on one side of the tube at a stage somewhat beyond the maximum pressure (Larsson et al. (1982)). Early research on the subject had been concentrated on bifurcation analysis based on the approach proposed by Hill (1958). Storakers (1971) studied strain hardening in rigid-plastic tubes and found that bifurcation away from the cylindrically symmetric state of the deformation mode may occur beyond the maximum pressure point. In the analysis for both very thin-walled and relatively thick-walled tubes, Chu (1979) extended Storakers' investigation by including elastic deformation. It was found by Chu (1979) that the predicted failure depends upon the loading conditions. More specifically, if the volume enclosed by the tube is prescribed, the cylindrically symmetric deformation may continue stably beyond the maximum pressure point until a bifurcation point is reached. However, if the internal pressure is an input quantity in the analysis, failure occurs in a cylindrically symmetric mode at the maximum pressure point, prior to a possible bifurcation point. Tadmor and Durban (1995) carried out a large strain analysis for internally pressured multi-layered tubes, and discussed the possibility of locating an optimal two-layer configuration. The finite element method has been widely used to predict instabilities and failure in pressurized tubes. Tomita and Shindo (1981) studied the development of circumferentially non-uniform deformation in cylinders under internal pressure using classical smooth yield surface plasticity theory. They found that in all cases investigated, bifurcation occurs beyond the maximum pressure point. Based on the J_2 corner theory proposed by Christoffersen and Hutchinson (1979), Larsson et al. (1982) carried out a plane strain analysis to numerically reproduce the experimentally observed neck development and the onset of localized shearing in narrow bands of material inside the neck. Since the plane strain analysis could not explain the formation of a localized bulge on one side of the tubes, Tvergaard (1990) reinvestigated the problem without restriction to planar deformation. It was revealed that the first critical bifurcation corresponds to an axisymmetric, non-cylindrical deformation mode, which subsequently develops into an axisymmetric bulge on the tube. The formation of a neck on one side of the bulge occurs as a second bifurcation well beyond the first bifurcation. Tugcu (1996) studied effects of strain rate sensitivity on instabilities and failure in pressurized tubes. Inertial effects in dynamic response of tubes under pressure impact were investigated by Han and Tvergaard (1995) and Tugcu (1995 & 1996) for metals and by Lindgreen et al. (2008) for glassy polymers. The influences of material anisotropy were explored by Jansson et al. (2005) and Korkolis and Kyriakides (2008); strain path changes by Asnafi and

Skogsgardh (2000), Korkolis and Kyriakides (2009) and Sorine et al. (2008); damage evolution by Varma et al. (2007); nonlocal effects by Mikkelsen and Tvergaard (1999). However, these investigations hardly improve our understanding of the effect of material microstructure on instabilities and failure in pressurized tubes. In this research, the goal is to extend the study of tube failure mechanisms through crystal plasticity to better understand the deformation behavior at the microstructure level.

1.1.2.1 Crystal plasticity

Isotropic plasticity modeling based on continuum theory combined with a return mapping algorithm provides a robust numerical method to solve nonlinear boundary value problems caused by material non-linearities with the finite element method; it also provides theoretical guidance for building other types of nonlinear plastic models. However, isotropic plasticity is not able to model heterogeneous plastic behavior observed in experiments. To address this problem, the first model was put forward by Schmid as shown in Fig. 1.2. This figure shows the deformation process of a single crystal. Not only does sliding between slip planes occur, also lattice rotation occurs if the traction boundary is not changed. The method to describe plastic deformation by crystallographic slip was formulated by Taylor and Elam (1923 & 1925), and Taylor (1938a & 1938b). Constitutive equations for the elasto-plastic behavior of single crystal materials were first formulated by Hill (1966) based on modern continuum mechanics, and extended to a finite strain formulation by Rice (1971), Hill and Rice (1972), Asaro and Rice (1977), and Asaro (1983a & 1983b). Modern finite strain crystal plasticity is built closely on a deep understanding of crystal structure, the mechanism of plastic slip, the theory of dislocation and finite strain kinematics and constitutive behavior. A brief introduction to crystal structure and theory of dislocation will be given here since they are indispensable components to building a crystal plasticity model.

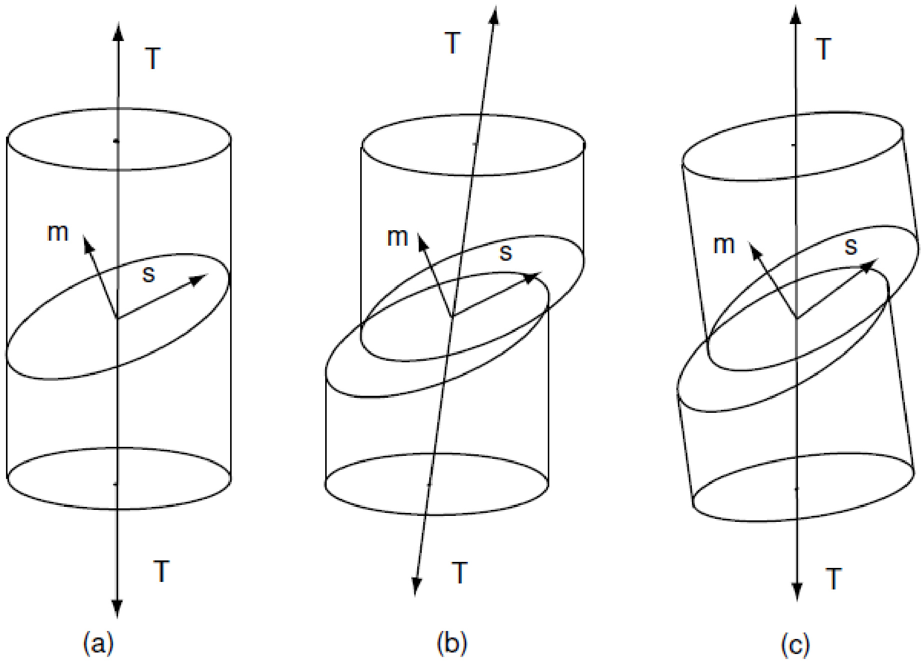

Figure 1.2 Schematic diagrams for a single crystal defined with a single slip system operating

1.1.2.2 Crystal plasticity modeling

Although kinematics and constitutive relations have been used for many years, there are three main problems that need to be solved in the modern rate-independent theory of crystal plasticity, mainly related to the issue of how to solve this system. The first is to determine which slip system is active. The second is to determine the increments of plastic strain in each active slip system. Third, due to the typical multiplicity of slip systems in crystals, the solution of slip systems which satisfy the yield functions is not necessarily unique. When the constitutive theory is applied to the numerical solution of boundary value problems, these three features of the rate-independent plasticity theory generally result in numerical problems as addressed by Anand (1994) and Kalidindi et al. (1992).

The first numerical calculations for a two-dimensional boundary value problem for a rate-independent elastic-plastic single crystal was put forward by Pierce et al. (1982), whose geometry was idealized in terms of a planar double slip model. Due to the lack of a robust solution strategy to determine the active slip systems and the amount of slip on these systems, the element stiffness matrices become singular for a particular choice of a slip system hardening rule resulting in numerical instabilities. To overcome the limitations of the rate-independent crystal plasticity, Asaro and Needleman (1985) developed a rate-dependent crystal plasticity model, which uniquely predicts a constitutive response for an arbitrary deformation history. Asaro and Needleman (1985) proposed that the shearing rate slip system is uniquely defined by:

$$\dot{\gamma}^{\alpha} = \dot{\gamma}_0 \left| \frac{\tau^{\alpha}}{g^{\alpha}} \right|^{\frac{1}{m}} sign\left(\tau^{\alpha}\right) \tag{1.1}$$

In Eq. 1.1, τ^{α} is the Schmid shear stress along slip direction, and g^{α} is deformation resistance in this slip system. The parameter $\dot{\gamma}_0$ is a reference shear rate. The parameter m is the material rate dependence; when m approaches 0, the model reproduces the rate-independent plasticity. Plastic strain rate is uniquely determined by this equation, and is proportional to the Schmid shear stress in that slip system. In crystal plasticity theories, the slip system strain hardening g evolves according to Eq. 1.2.

$$\dot{g}^{\alpha} = \sum_{\beta} h^{\alpha\beta} \left| \dot{\gamma}^{\beta} \right| \tag{1.2}$$

where $\dot{\gamma}^{\beta}$ is the plastic incremental rate and the hardening matrix $h^{\alpha\beta}$ defines the rate of hardening effect on slip system α due to plastic increment on slip system β; the diagonal terms define the self-hardening effect and off-diagonal terms define the latent-hardening effect of the slip systems. All terms in the hardening matrix $h^{\alpha\beta}$ are deformation history-dependent. As mentioned by Anand et al. (1996), the hardening moduli $h^{\alpha\beta}$ are the least well characterized part of the constitutive equations for crystal elasto-plasticity.

In the rate-dependent formulation of Asaro and Needleman (1985), all slip systems are always active and slip occurs at a rate which depends on the resolved shear stress and slip system deformation resistance. No yield surface is defined. When the resolved stress due to the external force is known, the plastic increment on all slip systems is uniquely determined. In their model, no restriction on the form of the hardening matrix $h^{\alpha\beta}$ is required. There has been considerable recent progress made in the extension and application of the rate-dependent crystal plasticity model of Asaro and Needleman (1985) to solve the important boundary value problems (Bronkhorst et al. (1992), Anand and Kalidindi (1994)). However, the rate-dependent constitutive equations for low values of the rate-sensitivity parameter m are very stiff, and the calculations are very time consuming. More research is still needed to develop a robust calculation scheme to determine the active slip systems, the corresponding plastic increments and the unique solutions for rate-independent theory of crystal plasticity.

To avoid the problem mentioned in rate-dependent formulation, Cuttino and Ortiz (1992), Anand et al. (1994 & 1996), and Miehe et al. (2001) have made significant contributions on formulating a numerical algorithm to solve rate-independent crystal plasticity. Cuitino and Ortiz (1992) proposed an algorithmic setting for a multisurface-type viscoplastic model within an elastic domain. Here, the problem of redundant constraints does not occur, due to the viscoplastic regularization effect. Borja and Wren (1993) propose a so-called ultimate algorithm for the rate-independent theory which follows the successive development of active slip within a typical discrete time interval. Anand et al. (1996) solves the system of redundant constraints of rate-independent single-crystal plasticity by using a generalized inverse on the basis of the singular-value decomposition of the Jacobian of the active yield criterion functions. This approach meets the least-square-type optimality conditions by minimizing the plastic dissipation due to the slip activities. Motivated by this development, Schroder and Miehe (1997) have proposed an alternative general inverse where the reduced space is obtained by dropping columns of the local Jacobian associated with zero diagonal elements within a standard factorization procedure.

During the last decade, these solution methods have been further developed and extended to study crystallographic texture and lattice rotation within single and poly crystals under uniaxial monotonic or cyclic loading by Dawson et al. (2002), Marin and Dawson (1998), Turkmen et al. (2002) and Huang et al. (2000) to study strain gradient plasticity. Since the research of Asaro et al. (1977, 1983a, 1983b and 1985) provide the main framework of kinematics and constitutive relations for finite strain crystal plasticity, the theoretical formulations will be discussed in Chapter 4.

The research on crystal plasticity has generated more industrial interest and expanded more understanding of sheet formability at the microstructure level. In the work on predicting surface roughening and roping in aluminum sheet by Wu et al. (2003a & 2003b) and Wu and Lloyd (2004), plastic deformation induced surface roughening was simulated using the finite element method, which was based on crystal plasticity and directly incorporated measured electron backscatter diffraction (EBSD) data. Numerical results were in good agreement with experimental observations. The methodology developed by Wu and Lloyd (2004) was adapted to further study localized necking in sheet metals under in-plane plane strain tension (Wu et al., 2007), which demonstrated that such a surface instability/necking is the natural outcome of the analysis, and the artificial initial imperfection necessitated by the other finite element analyses is not relevant in the analysis. It has been found that localized necking depends strongly on both the initial texture and its spatial orientation distribution.

In the present research, we follow the methodology developed by Wu and Lloyd (2004) and Wu et al. (2007) to study localized necking in an aluminum tube under internal pressure with an incorporated finite element based crystal plasticity model. The tube is assumed to be sufficiently long so that length changes as well as end effects can be ignored and a plane strain analysis can be performed. An EBSD map measured from commercial AA6111-T4 sheet is used as a direct input to define the initial grain orientation, and it is assumed that localized necking is associated with surface instability, the onset of an unstable thinning. The effects of spatial orientation distribution, material strain rate sensitivity, work hardening, and initial surface topography on necking are discussed.

1.1.3 Surface roughening analysis in aluminum tube on internal pressure

Surface roughening is another interesting topic and attracts great attention in the past. Early research showed that surface roughness evolves linearly with imposed strain and that it depends linearly on grain size (Wilson et al. (1981a, 1981b & 1983), Dai and Chiang (1992)). More recently, investigations (Becker (1998), Beaudoin (1998), Stoudt (2002), Banovic (2003), Wu et al. (1996, 2003a, 2003b, 2003c & 2004a) have been largely focused on understanding the origins of surface roughening and on quantitatively associating surface roughening with the spatial grain orientation distribution by using the technique of automated electron backscatter diffraction (EBSD) in the scanning electron microscope; in particular the use of EBSD in conjunction with a field emission scanning electron microscope (FEGSEM). Using the technique of EBSD provides not only the crystallographic orientation of grains, but also their spatial distribution. The FEGSEM now enables grain orientations to be measured over a large specimen area and this information can be directly incorporated into techniques such as the finite element method (FEM). Crystal plasticity based FEM has been used to investigate the role of grain orientation on the development of surface topography during straining (Becker

(1998) & Beaudoin (1998)). These studies were based on the observation that the grains lying on the surface deform differently from the grains in the interior of the sheet. The grain-to-grain incompatibility causes the surface grains to move normally to the surface, leading to surface roughening. The grains in the interior of the sheet are more constrained and deform in a manner consistent with the imposed deformation. In other words, surface roughening is mainly due to the inhomogeneous deformation between surfaces or near surface grains with little contribution from interior grains through interaction between the surface and supporting layers. More recently, Wu and Lloyd (2003a) have developed a FEM based on crystal plasticity and directly incorporated EBSD measured through the entire thickness. Based on a very large-scale EBSD map, the effects of imposed deformation path, strain work hardening, and strain rate sensitivity on surface roughening have been discussed in detail (2003a).

The deformation and failure of ductile cylindrical tubes under internal pressure has been studied experimentally and theoretically for many years (Ahmetoglu et al. (2000), Asnafi et al. (2000), Hartl (2005), Lang et al. (2004), Shi et al. (2010) and Zhang et al. (2011)). It has been generally accepted that failure in a pressurized elastic-plastic tube is usually initiated from a strong shear band inside a localized neck on one side of the tube at a stage somewhat beyond the maximum pressure. Shi et al. (2010) studied the localized necking of an aluminum tube under internal pressure. It was found that the localized necking was associated with a surface instability resulting from the non-uniform deformation of an aluminum tube under pressurization. Zhuang et al. (2011) investigated the localized thinning/necking mechanism in hydroforming of micro-tubes experimentally and numerically with an integrated crystal plasticity finite element (CPFE) modeling system. The analyses demonstrated that the localized thinning observed in hydroforming of micro-tubes is significantly affected by the microstructure and grain orientations of the material.

The overall objective of the present study was to further extend the methodology developed by Wu and Lloyd (2003a, 2003b, 2003c & 2004) and Shi et al. (2010) to study the surface roughening of an aluminum tube during hydroforming with a crystal plasticity based finite element code. The effects of spatial orientation distribution, material strain rate sensitivity, work hardening, and initial surface topography on the surface roughness evolution of an aluminum tube under internal pressurization are discussed.

1.1.4 Effect of rate sensitivity on necking behavior of tube under dynamic loading

The fracture of a ductile metal starts with the onset of necking. The plastic deformation accumulates in the necking zone as the strain level further increases until the fracture point is reached. For a strain rate independent material in uniaxial tension, the Considere criterion, defining that the onset of necking starts when the true stress equals the work hardening rate, gives a good indication of the ongoing localized strain before fracture occurs.

For a specimen under dynamic loading, the deformation and necking behavior are different from static/quasi-static loading. The direct experimental investigation of fracture and fragmentation response at high strain rates was done by Madsen and Niordson (1970);

they studied the stress-strain behavior of ring metal expanding at a very high strain-rates, in which electromagnetic loading is employed to expand the ring specimens very rapidly. Multiple-necks were observed around the circumference. The fracture strain was found to be higher than that in quasi-static loading. Fyfe and Rajendran (1980) examined the influence of strain-rate and dynamic pre-strain on the ductile fracture of thin cylinders, both experimentally and theoretically. A series of quasi-static and dynamic tests were conducted on three materials with different degrees of strain-rate sensitivity and strain-hardening. The expanding ring method was further exploited by Grady and Benson (1983) with experiments on OFHC copper and AA1100-O aluminum, by Altynova et al (1996) on solutionized AA6061, and by Zhang and Ravi-Chandar et al. (2006, 2008 and 2009) on AA6061-O, Al1100-H14 and soft Cu 101 materials. All these experiments reinforced many of the earlier observations that fracture is inhibited at high strain-rates and is in accord with the theory when inertia can no longer be considered insignificant. Grady (1983) found that fragments in ductile material under dynamic expansion have numerous partially developed neck regions where the stain is non-uniform. In terms of defining the fracture strain, Grady (1983) used the total length of all collected fragments to obtain a measure of the strain at fracture and quantified the increase of fracture strain with the increase of the strain rate. Altynova et al (1996) recognized that the partially developed necks tend to bias the average strain over the ring (measured from the total length of the all collected fragments) to a large strain. They measured both the local strain and the average strain, and found the two measures did not show a significant difference. They suggest that the inertia plays a big role for this small difference through numerical simulation with viscoplastic material model. Zhang and Ravi-Chandar et al. (2006 & 2008) examined inside and outside the neck region and found that the high value of the strain to fracture measured in the full length of recovered fragments is really due to the averaging the non-uniform strain variation over the nominal length of the fragment and that the high strains are really accumulated in the neck zones. The region outside the neck zone never experienced a strain larger than the Considere strain. Those experiments also reveal that the number of ring fragments is more likely to have a linear increase with the strain rate for the ductile materials tested.

In terms of understanding the inertia effect and prediction of the occurrence of multiple necking, fragmentation and strain retardation for dynamic necking, various models have been proposed. Mott (1947) used the statistical distribution model of the failure strain with Mott release wave theory to explain the numerical characterization of fragmentation. Kipp and Grady (1985) improved the Mott model through introducing Dugdle-Barenblat type cohesive model to simulate the fracture behavior and evaluate the statistical properties of the failure strain in the material. Grady's model has further be assessed by Miller et al (1999), Sheony and Kim(2003), Grady et al (2003) and Ravi-Chandar et al. (2006 & 2008). These cohesive type numerical analyses imposed an elastic response for the bulk material and are applicable to the fragmentation of brittle materials. A finite element based analysis with strain hardening behavior representing the ductile material was conducted by Han and Tvergaard (1995). Their results agreed well with Madsen and Niordson’s observations. They found that in a specimen with a small initial imperfection, the number of necks developed may exceed the thin-spots defined by the initial imperfection and form multiple necking spots. The dynamic strain localization and multiple neck generation are successfully reproduced, even though the fragmentation behavior has not been explored. Pandolfi et al (1999) incorporated the cohesive model into a finite element analysis, and simulate the expanding ring test under dynamic loading condition. Their results agree with most of the observation by Grady and Benson (1983). Becker (2002) used the Gurson damage model with a Drucker's bifurcation condition for material stability as a failure criterion. It showed, both experimentally and theoretically, that specimen could experience necking strain retardation and multiple-necking during dynamic loading. Recently, Xue and Hutchinson (2007), Xue et al. (2008) and Chen et al. (2010a, 2010b) further studied the deformation behaviors of metal-elastomer bilayer and metal-metal bilayer specimen under quasi-static stretching and impulsive pressure loading. Retardation of necking was observed due to energy absorption through the more ductile cladding layer.

It is well known that a relatively small amount of strain-rate dependence in rate sensitive material will lead to substantially increased strain prior to necking in quasi-static loading (Hutchinson and Neale, 1977; Ghosh, 1977; Hutchinson and Neale, 1978; Piece et al., 1984). Most materials show some strain-rate sensitivity. Limited research work explores how the rate sensitivity influences the localized necking and multiple-necking with rapid dynamic loading. Xue and Hutchinson (2008) studied the material aspect of dynamic retardation for thin plates under the rapid stretching. They found that the interplay between material rate-dependence and inertia in neck retardation is complex and dependent on the precise form of the constitutive model. The rate effects only come into play at higher strain-rates and have no influence on the quasi-static limit.

In the current work, we focus on the study of the rate sensitivity factor in tube expansion under high speed loading through numerical analysis, especially in the prediction of the multiple necks and retardation of the necking strain. In the second part, we will further expand this study to the effect of rate sensitivity in a laminate material system. In this study, we assumed that the tube, which is made of laminated sheet with cladding rate sensitive layer on a rate independent core material, undergoes a rapid dynamic expansion. This study investigates whether laminated material with rate dependent clad layers, which is supposed to be more effective at withstanding the localized necking, is superior to the rate-independent material in terms of delaying necking prior to fracture. In both cases, a plane strain condition is assumed.

1.2 Outline

First, the integration algorithm of a fully implicit elasto-viscoplastic constitutive model is completed in Chapter 2. With this algorithm, the MTS model, crystal plasticity model and rate dependent elasto-viscoplastic model are embedded into an FEA package, ABAQUS/Standard (2006) and ABAQUS/Explicit, with the user material subroutine UMAT (for Standard) and VUMAT (for Explicit).

Secondly, in Chapter 3, The MTS model, developed by Kocks and co-workers which is based on dislocation percolation with the main deformation mechanism of thermal activation, will be implemented into a general FE code, ABAQUS, as a user material subroutine to study the deformation behavior of aluminum sheet at high temperature and high strain rate forming conditions. Its application to PRF forming technology will also be discussed in detail. Thirdly, the single crystal plasticity model with its application on the prediction of tube failure necking under internal pressure will be addressed in Chapter 4 and the influence of texture components, material properties on the surface roughness of hydroformed tube will be studied in Chapter 5. In Chapter 6, we will study the effect of rate sensitivity on the necking behavior of an aluminum tube under dynamic loading, focusing on multiple necking formations and necking strain retardation due to high speed loading. Finally, conclusions and future work are listed in Chapter 7.

Chapter 2

Numerical Integration of Constitutive Equations for Inelastic Deformation

2.1 Introduction

Finite element analysis is an effective method for engineering problems involving inelastic deformation, which is always highly nonlinear. The deformation for the nonlinear problem in continuum mechanics is based on the equilibrium, boundaries and constitutive relations of the material. Based on the principle of virtual work (Bonet and Wood (1997), Cook and Malkus (2002)), the weak form of the equilibrium equation and boundary conditions is expressed as:

$$\int_V \delta \mathbf{E} \boldsymbol{\sigma} dV = \int_V \delta \mathbf{u} \mathbf{q} dV + \int_S \delta \mathbf{u} \mathbf{p} dS \tag{2.1}$$

here $\boldsymbol{\sigma}$ is Cauchy stress; $\delta \mathbf{u}$ is an arbitrary variation in displacement; $\delta \mathbf{E}$ is an arbitrary variation in strain; $\mathbf{p}$ and $\mathbf{q}$ are the surface load and volume load, respectively. The constitutive equation provides the rate dependence and temperature dependence on the flow stress. In the context of the finite element method, the nonlinear problem is discretized in terms of time and space; and the solution to this nonlinear problem is achieved by an iterative technique. The Newton-Raphson method is commonly used in which a sequence of linear equations is solved. With appropriate linearization of Eq. 2.1 around the last solution obtained, a quadratic rate of convergence can be achieved. After convergence, the displacement can be solved with the global FE system in the setting of a displacement-based finite element analysis. In turn, the strain can be calculated by:

$$\mathbf{E} = \frac{1}{2}\left[\nabla\mathbf{u} + \left(\nabla\mathbf{u}\right)^{T}\right] \tag{2.2}$$

For a rate dependent visco-plasticity model, inelastic deformation is an incremental process with a rate-controlled model. The time integration of a constitutive model is required to update the stress and state variables with respect to the driving quantities, strain or strain rate. The equilibrium equation with boundary conditions (Eq.2.1) is re-evaluated with the updated variables, such as stress. If convergence is not achieved, the equilibrium equation is revised and new values of stress at the end of the increment are calculated. Iteration continues until equilibrium is satisfied within an acceptable tolerance.

During the iteration of the global FEM system with the Newton-Raphson method, the tangent stiffness at the end of time increment must be re-evaluated for the linearization of the non-linear virtual work equation. The tangent stiffness is defined by

$$\mathbf{M} = \frac{d\boldsymbol{\sigma}}{d\mathbf{E}} \tag{2.3}$$

a fourth-order tensor based on the constitutive model. As the tangent stiffness is used in the search for incremental variables to balance the equilibrium equation, approximations in evaluation do not affect the accuracy of the final solution. In order to achieve the quadratic convergence which is characteristic of the Newton-Raphson method, it is important to evaluate the stiffness accurately in a way consistent with the time integration method (Simo and Hughes (1998), Simo and Taylor (1985)).

In summary, time integration of a constitutive model plays an important role in elasto-plastic finite element computation. Firstly, faithful simulation of the computational inelasticity is dependent on accurate updates of stress and the state variable. Secondly, the time integration contributes to the convergence of the global FEM system by determining the tangent stiffness during the iteration.

The time integration of a constitutive equation is a typical initial values problem. Normally two types of method are applied: explicit and implicit (ABAQUS 2006). Explicit methods, such as Euler's method, perform the computation with known information from the previous time step, so an iteration problem is involved, but stability is limited. A large step size may cause deviation from the true solution. Implicit methods, such as the backward Euler method, evaluate the function with unknown variables at the current time step; an iterative solution is always required for a nonlinear function. For some cases, an improper initial value may result in the divergence of the iteration. Implicit methods are characterized by unconditional stability, and as a result, a larger time step size may lead to less total analysis time.

In this chapter, the time integration of the constitutive equation is discussed with the implicit method. The procedure is classic and provided for completeness of the MTS model, rate sensitivity model, and crystal plasticity applied in the following chapter. The strain rate decomposition based on the kinematic relation and objective expression for the rate form constitutive models are shown, which are consistent with the framework of ABAQUS. The general description for the radial return integration algorithm and updated tangent stiffness are also introduced.

2.2 Kinematic relations

With the definition of the general constitutive model, the total deformation gradient $\mathbf{F}$ can be multiplicatively decomposed into terms which account for the elastic part $\mathbf{F}^{*}$ and plastic part $\mathbf{F}^{\mathbf{p}}$ respectively:

$$\mathbf{F} = \mathbf{F}^{*}\mathbf{F}^{\mathbf{p}} \tag{2.4}$$

A more general assumption is that the motion defined by $\mathbf{F}$ consists of rigid body rotation $\mathbf{R}$ and deformation:

$$\mathbf{F} = \mathbf{V}\mathbf{R} = \mathbf{R}\mathbf{U} \tag{2.5}$$

where $\mathbf{V}$ and $\mathbf{U}$ are the left and right stretch, respectively. The rigid body rotation $\mathbf{R}$ is an orthogonal matrix with $\mathbf{R}\mathbf{R}^{\mathbf{T}} = \mathbf{I}$. The decomposition is shown in Fig. 2.1. The initial and final configurations are represented by $\mathbf{A_0}$ and $\mathbf{A}$ respectively; the intermediate configuration $\overline{\mathbf{A}}$ is defined as material configuration, which is obtained by pulling the current configuration back to eliminate the effect of rigid rotation. The motion defined by $\mathbf{F}$ consists of rigid body motion and deformation. For the general case there is no advantage in associating rigid body motion with both the inelastic and the elastic deformation: we lose nothing by writing:

$$\mathbf{F} = \mathbf{V}^{*}\mathbf{V}^{\mathbf{p}}\mathbf{R} = \mathbf{R}\mathbf{U}^{*}\mathbf{U}^{\mathbf{p}} \tag{2.6}$$

With the expression of the deformation gradient Eq. 2.6, the velocity gradient $\mathbf{L} = \dot{\mathbf{F}}\mathbf{F}^{-1}$ is expressed as:

$$\mathbf{L} = \dot{\mathbf{F}}\mathbf{F}^{-1} = \dot{\mathbf{F}}^{*}\mathbf{F}^{*-1} + \mathbf{F}^{*}\dot{\mathbf{F}}^{\mathbf{p}}\mathbf{F}^{\mathbf{p}-1}\mathbf{F}^{*-1} = \mathbf{L}^{*} + \mathbf{F}^{*}\mathbf{L}^{\mathbf{p}}\mathbf{F}^{*-1} \tag{2.7}$$

where $\mathbf{L}^{\mathbf{p}} = \dot{\mathbf{F}}^{\mathbf{p}}\mathbf{F}^{\mathbf{p}-1}$.

For the material of concern, with $\mathbf{F}^* = \mathbf{V}^* = \mathbf{I} + \boldsymbol{\varepsilon}^{\mathbf{el}}$:

$$\mathbf{L} = \dot{\mathbf{F}}^*\mathbf{F}^{*-1} + (\mathbf{I} + \boldsymbol{\varepsilon}^{\mathbf{el}})\dot{\mathbf{F}}^{\mathbf{p}}\mathbf{F}^{\mathbf{p}-1}(\mathbf{I} + (\boldsymbol{\varepsilon}^{\mathbf{el}})^{-1}) \approx \mathbf{L}^* + \mathbf{L}^{\mathbf{P}} \tag{2.8}$$

taking the symmetric part:

$$\dot{\boldsymbol{\varepsilon}} \approx \dot{\boldsymbol{\varepsilon}}^{\mathbf{el}} + \dot{\boldsymbol{\varepsilon}}^{\mathbf{p}} \tag{2.9}$$

where $\dot{\boldsymbol{\varepsilon}} = \mathrm{sym}(\mathbf{L})$; $\dot{\boldsymbol{\varepsilon}}^{\mathbf{el}} = \mathrm{sym}(\mathbf{L}^*)$ $\dot{\boldsymbol{\varepsilon}}^{\mathbf{P}} = \mathrm{sym}(\mathbf{L}^{\mathbf{P}})$ are the total, elastic, and inelastic strain rates.

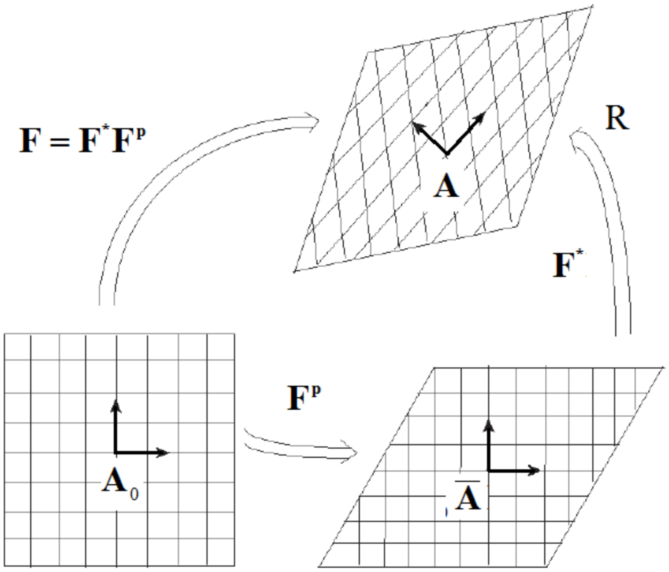

Figure 2.1 Schematic illustration of multiplicative decomposition

2.3 Constitutive relations

With the assumption of small elastic strain (but the plastic strain is allowed to be arbitrary large), the Cauchy stress only depends on the elastic part of the deformation gradient and the relation is isotropic:

$$\boldsymbol{\sigma} = 2\mu\mathbf{E} + \lambda tr(\mathbf{E})\mathbf{I} \tag{2.10}$$

where μ and λ are Lamé constants; and $\mathbf{E}$ is the total strain.

In order to keep the constitutive model "frame indifferent" or "objective", the general applied stress rate is the Jaumann rate, which is defined by:

$$\overset{\nabla *}{\boldsymbol{\sigma}} = \overset{\nabla}{\boldsymbol{\sigma}} + \mathbf{W} \cdot \boldsymbol{\sigma} - \boldsymbol{\sigma} \cdot \mathbf{W} \tag{2.11}$$

Note the skew tensor $\mathbf{W} = \mathbf{R}\mathbf{R}^{\mathbf{T}}$ and $\mathbf{W}^{\mathrm{T}} = -\mathbf{W}$

Generally, the constitutive model of a material is always formulated with respect to the current state of the material (Nagtegall and Veldpaus (1984)), i.e. the material configuration. For the deformation with large strain and rotation, the stress involved in the model is not the Cauchy stress in final configuration, but the stress stored in the material $\overline{\mathbf{A}}$, which is equivalent to the Cauchy stress rotated back to eliminate the rigid rotation by $\mathbf{R} \cdot \boldsymbol{\sigma} \cdot \mathbf{R}^{\mathbf{T}}$. In the finite element code ABAQUS/Standard, the Cauchy stress reported has been rotated back to the previous time frame. As a result, the constitutive equation on co-rotational stress rates is given by:

$$\dot{\boldsymbol{\sigma}} = 2\mu\dot{\boldsymbol{\varepsilon}}^{\mathbf{el}} + \lambda tr(\dot{\boldsymbol{\varepsilon}}^{\mathbf{el}})\mathbf{I} \tag{2.12}$$

with this stress transformation, the material time derivative of stress $\dot{\boldsymbol{\sigma}}$ instead of more complicated Jaumann rate $\overset{\nabla *}{\boldsymbol{\sigma}}$ is involved in evaluation of the constitutive model.

Rearranging the kinematic relation with Eq. 2.9, the constitutive equations applied in the material configuration include:

$$\dot{\boldsymbol{\sigma}} = 2\mu(\dot{\boldsymbol{\varepsilon}} - \dot{\boldsymbol{\varepsilon}}^{\mathbf{p}}(\boldsymbol{\sigma},\mathbf{s}^*)) + \lambda tr(\dot{\boldsymbol{\varepsilon}})\mathbf{I} \tag{2.13}$$

and

$$\dot{\mathbf{s}}^* = \dot{\mathbf{s}}^*(\boldsymbol{\sigma},\mathbf{s}^*) \tag{2.14}$$

Note $\dot{\boldsymbol{\varepsilon}}$ is the driving quantity in this integration problem. Beside the integration of stress $\boldsymbol{\sigma}$, the state variable $\mathbf{s}^*$, which could be a function of $\dot{\boldsymbol{\varepsilon}}^{\mathbf{p}}(\boldsymbol{\sigma},\mathbf{s}^*)$, have to be integrated with the rate form of hardening law. Typically an incremental solution procedure is applied for the non-linear elasto-plastic analysis, with an updated Lagrangian scheme (Cook and Malkus (2002)), i.e. the configuration of material at time t_n is taken as the reference configuration for the time interval [t_n, t_{n+1}]; at the end of the increment, the configuration is taken as the reference configuration for the subsequent time increment. For the time step [t_n, t_{n+1}], time integration is required to update the equilibrium stress field and state variables at the time $\mathrm{t}_{\mathrm{n+1}}$ from the known variables at time t_n. The increment of logarithmic strain is calculated by ABAQUS (2006):

$$\Delta\boldsymbol{\varepsilon} = \ln(\mathbf{V_r}) \tag{2.15}$$

where $\mathbf{V_r}$ is the increment of the stretch matrix computed from the polar decomposition of the relative deformation gradient $\mathbf{F_r}$:

$$\mathbf{F_r} = \mathbf{V_r}\mathbf{R} \tag{2.16}$$

where $\mathbf{F_r}$ is calculated by:

$$\mathbf{F_r} = \mathbf{F^{n+1}}/\mathbf{F^n} \tag{2.17}$$

$\mathbf{F^{n+1}}$ is the deformation gradient at current time step and $\mathbf{F^n}$ is at previous time step. Since the update Lagrangian description is applied, the strain increment is always small, so the strain rate during the time increment can be assumed constant as:

$$\dot{\boldsymbol{\varepsilon}} = \frac{\boldsymbol{\Delta\varepsilon}}{\Delta t} \tag{2.18}$$

2.4 Integration scheme: radial return algorithm

In this section, only time integration of the co-rotated portion in the material frame is considered, the rigid rotation is performed before integration. Eq. 2.13 and Eq. 2.14 are the governing equations for the evolution of the material variables: stress and state variables. Applying the consistent and stable Euler backward method, we obtain:

$$\boldsymbol{\sigma}^{n+1} = \boldsymbol{\sigma}^n + 2\mu\Delta t(\dot{\boldsymbol{\varepsilon}}^{n+1} - \dot{\boldsymbol{\varepsilon}}_{\mathbf{p}}(\boldsymbol{\sigma}^{n+1}, \mathbf{s}^{*n+1})) + \Delta t\lambda(tr(\dot{\boldsymbol{\varepsilon}}^{n+1}))\mathbf{I} \tag{2.19}$$

and

$$\mathbf{s}^{*n+1} = \mathbf{s}^{*n} + \Delta t\dot{\mathbf{s}}^*(\boldsymbol{\sigma}^{n+1}, \mathbf{s}^{*n+1}) \tag{2.20}$$

For the most of the section, the superscript “n” and “n+1” on variables will indicate that the variables are evaluated at the beginning and the end of the time interval $[t_n, t_{n+1}]$, respectively. Then the time integration problem is simplified to calculate $(\boldsymbol{\sigma}^{n+1}, \mathbf{s}^{*n+1})$ by solving the Eq. 2.19 and Eq. 2.20 with the known initial values $(\boldsymbol{\sigma}^n, \mathbf{s}^{*n})$. Logarithmic strain $\dot{\boldsymbol{\varepsilon}}^{n+1}$ is the driving variable, which can be calculated from the known kinematic information in a displacement-based finite element program.

The radial return algorithm is applied as an effective integration procedure (Lush et al. (1989), Simo and Hughes (1998) and Weber et al. (1990)). Its accuracy and effectiveness are shown by Krieg and Kerige (1977). Firstly, a trial elastic state is obtained by freezing plastic flow:

$$\boldsymbol{\sigma}_{trial}^{n+1} = \boldsymbol{\sigma}^{n} + 2\mu\Delta t\dot{\boldsymbol{\varepsilon}}^{n+1} + \lambda\Delta t(tr(\dot{\boldsymbol{\varepsilon}}^{n+1}))\mathbf{I} \tag{2.21a}$$

$$\mathbf{s}_{trial}^{*n+1} = \mathbf{s}^{*n} \tag{2.21b}$$

where the trial stress $\boldsymbol{\sigma}_{\mathrm{trial}}^{\mathrm{n+1}}$ is determined in terms of initial conditions and the given incremental strain; the trial variable $\mathbf{s}_{\mathrm{trial}}^{*\mathrm{n+1}}$ is assumed unchanged from previous results.

Next the trial state is evaluated with Kuhn-Tucker loading/unloading condition (Hughes (1984)): with an elastic step, the trial state is the actual solution: if the trial stress is great than the yield strength, the return mapping algorithm is performed to find the true solution, which is the closed projection on the yield surface (Simo and Hughes (1985)). For a rate dependent visco-plastic material, plastic flow is assumed for all nonzero values of the stress, even at the very beginning of the deformation path, the flow rate may be very small.

Substitutive trial stress (Eq. 2.21) into the constitutive relation (Eq. 2.19 and Eq. 2.20), a system of nonlinear equations for $(\boldsymbol{\sigma}^{\mathrm{n+1}}, \mathbf{s}^{*\mathrm{n+1}})$ are shown by:

$$\mathbf{R}_{\boldsymbol{\sigma}} = \boldsymbol{\sigma}^{n+1} - \boldsymbol{\sigma}_{trial}^{n+1} + 2\mu\Delta t\dot{\boldsymbol{\varepsilon}}_{p}(\boldsymbol{\sigma}^{n+1}, \mathbf{s}^{*n+1}) \tag{2.22a}$$

$$\mathbf{R}_{s^*} = \mathbf{s}^{*n+1} - \mathbf{s}^{*n} - \Delta t\dot{\mathbf{s}}^{*}(\boldsymbol{\sigma}^{n+1}, \mathbf{s}^{*n+1}) \tag{2.22b}$$

Now we define $\mathbf{R}_{a}$ to cover the above two residual equations:

$$\mathbf{R}_a = \begin{bmatrix} \mathbf{R}_{\boldsymbol{\sigma}} \\ \mathbf{R}_{s^*} \end{bmatrix} \tag{2.23}$$

where the unknown variable $\mathbf{X}$ is a vector of stress components and internal state variables:

$$\mathbf{X} = \begin{bmatrix} \boldsymbol{\sigma}^{n+1} \\ \mathbf{s}^{*n+1} \end{bmatrix} = \begin{bmatrix} \boldsymbol{\sigma}_{11}^{n+1} \\ \ldots \\ \mathbf{s}_1^{*n+1} \\ \ldots \end{bmatrix} \tag{2.24}$$

Then Newton-Raphson method is applied to solve the nonlinear system $\mathbf{R}(\mathbf{X}) = 0$ in an iterative way:

$$\Delta\mathbf{X} = -\mathbf{J}^{-1}\mathbf{R} \tag{2.25}$$

where the Jacobian matrix is:

$$\mathbf{J} = \frac{\partial R}{\partial X} = \begin{bmatrix} \dfrac{\partial \mathbf{R}_{\sigma}}{\partial \boldsymbol{\sigma}^{n+1}} & \dfrac{\partial \mathbf{R}_{\sigma}}{\partial \mathbf{s}^{*n+1}} \\ \dfrac{\partial \mathbf{R}_{s^*}}{\partial \boldsymbol{\sigma}^{n+1}} & \dfrac{\partial \mathbf{R}_{s^*}}{\partial \mathbf{s}^{*n+1}} \end{bmatrix} \tag{2.26}$$

Then the variables are updated by:

$$\mathbf{X} = \mathbf{X} + \Delta\mathbf{X} \tag{2.27}$$

2.5 Consistent tangent stiffness

As stated in the introduction of this chapter, the tangent stiffness $\mathbf{M}$ is needed in the linearization of the weak form of the equilibrium equation (Eq. 2.1). It can be obtained directly from co-rotational stress and strain; both are stored in the material configuration:

$$\mathbf{M} = \frac{d\boldsymbol{\sigma}}{d\boldsymbol{\varepsilon}} \tag{2.28}$$

There are two kinds of tangent stiffness. The first is the continuum elasto-plastic tangent stiffness, which is derived only from the constitutive relation (Eq. 2.13) and related to flow rule and inelastic expression. The second is the consistent tangent stiffness, which is obtained by consistent linearization of the response function resulting from the integration algorithm. For large time steps, the difference between the two tangent stiffnesses is distinct. It has been demonstrated that consistent tangent stiffness plays an important role in achieving the quadratic convergence rate of the Newton-Raphson iteration for the global system (Simo and Hughes (1998), Simo and Taylor (1995)).

In order to calculate consistent tangent stiffness, the residual system (Eq. 2.22) applied in the time integration is differentiated with respect to $\boldsymbol{\varepsilon}^{n+1}$ (then the superscript “n+1” is omitted for clarity):

$$\frac{\partial \mathbf{R}_{\sigma}}{\partial \boldsymbol{\varepsilon}} + \frac{\partial \mathbf{R}_{\sigma}}{\partial \boldsymbol{\sigma}}\frac{\partial \boldsymbol{\sigma}}{\partial \boldsymbol{\varepsilon}} + \frac{\partial \mathbf{R}_{\sigma}}{\partial \mathbf{s}^*}\frac{\partial \mathbf{s}^*}{\partial \boldsymbol{\varepsilon}} = 0 \tag{2.29a}$$

$$\frac{\partial \mathbf{R}_{s^*}}{\partial \boldsymbol{\varepsilon}} + \frac{\partial \mathbf{R}_{s^*}}{\partial \boldsymbol{\sigma}}\frac{\partial \boldsymbol{\sigma}}{\partial \boldsymbol{\varepsilon}} + \frac{\partial \mathbf{R}_{s^*}}{\partial \mathbf{s}^*}\frac{\partial \mathbf{s}^*}{\partial \boldsymbol{\varepsilon}} = 0 \tag{2.29b}$$

then with the same Jacobian matrix, the solution is obtained by a simple back substitution:

$$\begin{bmatrix} \dfrac{\partial \boldsymbol{\sigma}}{\partial \boldsymbol{\varepsilon}} \\ \dfrac{\partial \mathbf{s}^*}{\partial \boldsymbol{\varepsilon}} \end{bmatrix} = -\mathbf{J}^{-1} \begin{bmatrix} \dfrac{\partial \mathbf{R}_{\sigma}}{\partial \boldsymbol{\varepsilon}} \\ \dfrac{\partial \mathbf{R}_{s^*}}{\partial \boldsymbol{\varepsilon}} \end{bmatrix} \tag{2.30}$$

2.6 User material subroutine for ABAQUS

The MTS model, crystal plasticity and rate dependent elastic-viscoplastic model used in this research have all been implemented into a general finite element code ABAQUS through the time integration scheme as addressed in this chapter. The subroutine is written in FORTRAN. The commercial FEM package ABAQUS provides an easy way to define mechanical constitutive behavior for a customized material. In the UMAT/VUMAT (UMAT for implicit code and VUMAT for explicit code), all the computations are associated with material configuration. The basis systems in which stress and strain are stored with material, i.e. the stress and strain tensors, have already been rotated to account for rigid body motion in the increment before UMAT is called.

The input information passed into the UMAT by ABAQUS includes: total strain $\boldsymbol{\varepsilon}$, stress $\boldsymbol{\sigma}$ and state variables at the beginning of the increment, strain increment $\Delta\boldsymbol{\varepsilon}$ of the current time increment, and all material constants entered by the "*USER MATERIAL" keyword in the input file.

The main task of the UMAT/VUMAT is to integrate the material constitutive model at each integration point, then update stress and solution dependent state variables; at the same time, the UMAT should provide consistent tangent stiffness, which is required by the global FE system (VUMAT does not need tangent stiffness). The following is the outline for a UMAT/VUMAT:

1. Initialize stress and strain with the information passed in by ABAQUS
2. Compute trial stress by freezing plastic deformation as Eq. 2.21
3. Derive residual based on kinematics and constitutive relations

$$\mathbf{R} = \begin{bmatrix} \mathbf{R}_{\boldsymbol{\sigma}} \\ \mathbf{R}_{s^*} \end{bmatrix} = 0$$

4. Perform Newton-Raphson iteration to solve the nonlinear system

$$\Delta\mathbf{X} = -\mathbf{J}^{-1}\mathbf{R}$$

5. Update stress and state variables at the end of the increment, upon convergence

$$\mathbf{X} = \mathbf{X} + \Delta\mathbf{X}$$

6. Evaluate consistent tangent stiffness (UMAT only)

$$\mathbf{M} = \frac{\mathrm{d}\boldsymbol{\sigma}}{\mathrm{d}\boldsymbol{\varepsilon}}$$

Chapter 3

Hot/Warm Hydroforming Process Simulation

The typical hot forming temperature of can body stock alloy AA3104 for which we are interested is between 300°C and 400°C. This temperature region is dominated by thermal recovery, and the enhanced strain-hardening rate is due to dynamic strain aging. The material experiences both positive work hardening and strain rate sensitivity. The modified MTS model has been chosen to describe the plastic deformation behavior of metal under these loading conditions.

3.1 MTS constitutive equations

The Mechanical Threshold Stress (MTS) model (Kocks 2003) is a physically-based model for rate dependent plasticity with a long-range slip. The model is based on the percolation of mobile dislocations through the slip plane, or areal glide. In turn, the flow stress depends on “hard spots”. The deformation is controlled by the interaction of dislocations with these obstacles. Thermal activation for dislocations to overcome barriers provides rate and temperature dependence. Work hardening and recovery follow from the evolution of an internal state variable, the mechanical threshold (strength at 0K), which is related to dislocation and characterizes the strongest obstacle, or hard spot, in the slip plane. It is important to note that the MTS framework is not intended to describe plasticity at stress below the flow stress. Such flow is associated with the regions of the slip plane that are “soft”, or equivalently, regions where short-range slip may occur at a particular value of stress. This is distinct from long-range slip, associated with the flow stress and characterized by a maximum glide plane resistance, or mechanical threshold.

In the MTS material model, an internal state variable called mechanical threshold stress, $\hat{\sigma}$, is interpreted as the material flow stress at 0K. This state variable describes the lattice structure evolution using a balance of dislocation generation and thermal recovery process that depends on strain rates and temperatures. The flow stress is defined as a function of strength contributing to the mechanical threshold:

$$\frac{\sigma}{\mu} = S_{\varepsilon}(\dot{\varepsilon}, T)\frac{\hat{\sigma}}{\mu_0} \tag{3.1}$$

where $\hat{\sigma}$ is the mechanical threshold strength, $\dot{\varepsilon}$ is strain rate, T is temperature in Kelvin and μ is the shear modulus, which is defined as a function of temperature T:

$$\mu = \mu_0 - \frac{\mu_d}{\exp(\frac{T_0}{T}) - 1} \tag{3.2}$$

where, μ_d and T_0 are constants, and μ_0 is the shear modulus at 0K. The scale factor, S_{ε}, specifying the ratio of the flow stress to the mechanical threshold stress, $\hat{\sigma}$, is a function of temperature T and strain rate $\dot{\varepsilon}$:

$$S_{\varepsilon} = \left[1 - \left(\frac{kT}{g_0 \mu b^3}\ln\left(\frac{\dot{\varepsilon}_0}{\dot{\varepsilon}}\right)\right)^{1/q}\right]^{1/p} \tag{3.3}$$

where, k is Boltzmann’s constant and b is the Burgers vector; g_0, $\dot{\varepsilon}_0$, p and q are material constants.

The work hardening rate is described by:

$$\theta = \frac{d\widehat{\sigma}}{d\varepsilon} = \theta_0 (1 - \frac{\widehat{\sigma}}{\widehat{\sigma}_s})^2 \tag{3.4}$$

where $\widehat{\sigma}_s$ is the saturation value of $\hat{\sigma}$ and θ_0 is the initial work hardening rate.

Compared with the MTS model (Eq. 3.5) proposed by Kocks (2003), there are two terms omitted in this modified MTS:

$$\frac{\sigma}{\mu} = \frac{\sigma_{at}}{\mu} + S_i(\dot{\varepsilon}_p, T)\frac{\sigma_i}{\mu_0} + S_\varepsilon(\dot{\varepsilon}, T)\frac{\hat{\sigma}}{\mu_0} \tag{3.5}$$

The first term of the right hand side of Eq. 3.5, an athermal component, σ_{at}, is typically associated with long range stress developed through dislocation interactions with grain boundaries. The application of this model is aluminum can body stock AA3104 under a re-crystallized state. In this undeformed FCC metal, the contribution of σ_{at} is usually very small and can be ignored. The second term in Eq. 3.5 describes the rate dependence of the yield stress mainly due to intrinsic barriers, such as solute atoms and precipitates in the aluminum system. The scalar S_i specifies the ratio between the contributions to the flow stress and threshold strength contribution. For AA3104 with 1.0-1.1% Mg, solute strengthening introduced by Mg is relatively smaller than strain hardening due to the dislocation accumulation. The second terms has been omitted for simplification.

3.2 Numerical implementation

The modified MTS constitutive equations (Eq. 3.1 to Eq. 3.4) are implemented into the non-linear implicit finite element code in ABAQUS/Standard through a user material subroutine (UMAT). The backward Euler time integration algorithm discussed in Chapter 2 is used during each time interval. The numerical implementation of the MTS constitutive equations will be discussed here.

3.2.1 Elastic trial state:

We assumed that in the interval [t_n, t_{n+1}], no plastic deformation occurs. As a result, we have trial values:

$$\boldsymbol{\varepsilon}^{\mathbf{p,Tr}} = \boldsymbol{\varepsilon}^{\mathbf{p}}_{\mathbf{n}} \tag{3.6}$$

$$\dot{\boldsymbol{\sigma}}^{\mathbf{Tr}} = \boldsymbol{\sigma}_{\mathbf{n}} + 2G\dot{\boldsymbol{\varepsilon}}^{\mathbf{e}} \tag{3.7}$$

$$\dot{\boldsymbol{\varepsilon}}^{\mathbf{P}} = \dot{\gamma}\frac{\mathbf{S}}{\|\mathbf{S}\|}$$

where $\dot{\boldsymbol{\sigma}}^{\mathbf{Tr}}$ is a trial stress rate, G is shear modulus, $\dot{\boldsymbol{\varepsilon}}^{\mathbf{P}}$ is plastic strain rate and $\mathbf{S}$ is deviatoric stress. If the elastic trial state is admissible, i.e. it does not violate the limit of yield, then it represents the new solution at t_{n+1} and next part of the algorithm is skipped. If the elastic trial state is not admissible, a plastic correction is performed.

3.2.2 Plastic correction

We use the Euler backward procedure to integrate constitution equations.

Firstly, the effective stress $\bar{\sigma}$ is defined as follows:

$$\bar{\sigma} = \sqrt{\frac{3}{2}\mathbf{S}:\mathbf{S}} \tag{3.8}$$

The plastic strain increment is written from the flow potential as:

$$\dot{\boldsymbol{\varepsilon}}^{\mathbf{pl}} = \dot{\varepsilon}^{pl}\mathbf{n} \tag{3.9}$$

where $\mathbf{n}$ is the flow direction and ε^{pl} is effective plastic strain.

For the modified MTS model, we can rewrite Eq. 3.1 and Eq. 3.3 as:

$$\dot{\bar{\varepsilon}}^{p} = g(\bar{\sigma}, \hat{\sigma}_{\varepsilon}) \tag{3.10}$$

And

$$d\hat{\sigma}_{\varepsilon} = k(\bar{\sigma}, \hat{\sigma}_{\varepsilon}) \tag{3.11}$$

The effective stress is updated through correcting of trial stress:

$$\sigma_{n+1} = \sigma_{n+1}^{T} - 3G\Delta t\dot{\varepsilon}_{n+1}^{p} \tag{3.12}$$

The mechanical threshold stress is updated through:

$$\hat{\sigma}_{n+1} = \hat{\sigma}_{n} + k(\bar{\sigma}_{n+1}, \hat{\sigma}_{\varepsilon n+1}) \tag{3.13}$$

Through rearranging Eq. 3.8, Eq. 3.12 and Eq. 3.13, we can get the following two non-linear equations:

$$\bar{\sigma}_{n+1} - \bar{\sigma}_{n+1}^{T} + 3Gg(\bar{\sigma}_{n+1}, \hat{\sigma}_{\varepsilon n+1})\Delta t = 0 \tag{3.14}$$

and

$$\hat{\sigma}_{n+1} - \hat{\sigma}_{n+1} - k(\bar{\sigma}_{n+1}, \hat{\sigma}_{\varepsilon n+1})\Delta t = 0 \tag{3.15}$$

The Newton-Raphson method is used to solve these two equations to find the updated $\bar{\sigma}_{n+1}$ and $\hat{\sigma}_{n+1}$. In this work, the consistent tangent stiffness has been adopted and derived into the ABAQUS UMAT.

3.2.3 Heat generation

To capture the heat generation caused by mechanical dissipation associated with plastic straining, a fully thermal-mechanical coupled analysis is adopted. In this thermal-mechanical coupled model, it assumes that plastic deformation results in a heat flux, r^{pl}:

$$r^{pl} = \eta \boldsymbol{\sigma} : \dot{\boldsymbol{\varepsilon}}^{\mathbf{pl}} \tag{3.16}$$

where η is the factor defining how much plastic work is converted to thermal energy, $\boldsymbol{\sigma}$ is the Cauchy stress and $\dot{\boldsymbol{\varepsilon}}^{\mathbf{pl}}$ is the plastic strain rate.

ABAQUS uses a backward Euler scheme to integrate the plastic strain, r^{pl} at the end of the increment is approximated as:

$$r^{pl} = \frac{1}{2\Delta t} \eta \Delta \varepsilon^{pl} \mathbf{n} : (\boldsymbol{\sigma}_{\mathbf{n+1}} + \boldsymbol{\sigma}_{\mathbf{n}}) \tag{3.17}$$

This term is used as the contribution to the thermal energy balance equation. In the ABAQUS user subroutine, when Newton's method is used to solve the nonlinear equations, the above coupling term gives rise to four contributions to Jacobian matrix for the Newton method:

$$\frac{\partial \boldsymbol{\sigma}}{\partial \boldsymbol{\varepsilon}}, \frac{\partial \boldsymbol{\sigma}}{\partial \theta}, \frac{\partial r^{pl}}{\partial \boldsymbol{\varepsilon}}, \frac{\partial r^{pl}}{\partial \theta}$$

All these terms must be properly defined in order to get a solution that converges quickly.

The heat flux term generated by the plastic work is then added to the basic energy balance as:

$$\int_V \rho \dot{U} dV = \int_S q dS + \int_V r dV \tag{3.18}$$

where V is a volume of solid material with surface of S; ρ is the density of material; $\dot{U}$ is the material time rate of internal energy; q is the heat flux of the body, flowing into the body; and r is the heat supplied externally into the body.

The material model is implemented into ABAQUS as a user subroutine UMAT and the energy balance is satisfied using the ABAQUS user subroutine UMATTH.

3.3 Identification of material parameters

Identification of material parameters associated with this modified MTS plasticity models is a critical issue for the FE simulation of the sheet forming process. We use a traditional Fisher plot (Banerjee (2007)) to calibrate the material constants. The experiments required to evaluate the parameters of the Fisher plot equation are straightforward. All that is required is a set of tensile test data covering most of the range of temperatures and strain rates of interest. It is significant and important to note that with this approach, and its incumbent formulation, it is not necessary to have experimental data to cover the entire range of temperature and strain rates that might be encountered in a forming operation. It is sufficient to extrapolate the fit to temperature and strain rates outside the range of experiment. Here, we just briefly list the procedures for this AA3104-O temper alloy.

All the material constants needed to be determined are fitted from the flow stress Fisher plot and $\theta^{\exp eriment}$ Fisher plot. Here we assume that σ_{yield}, $\sigma_{saturation}$, $\theta^{\exp riment}, T, \dot{\varepsilon}$ can be extracted from the raw data of the experiment. All the following calculations are from these known variables.

3.3.1 Fitting the flow stress parameter $g_{0\varepsilon}$

1 Calculate μ according to Eq. 3.2, $\mu = \mu_0 - \dfrac{\mu_d}{\exp(\frac{T_0}{T}) - 1}$

2 Calculate $\dfrac{kT}{\mu b^3}$ and Fisher parameter $[\dfrac{kT}{\mu b^3}\ln(\dfrac{10^7}{\dot{\varepsilon}})]^{\frac{1}{q_\varepsilon}}$

3 Calculate $(\dfrac{\sigma_{yield}}{\mu})^{p_\varepsilon}$ and $(\dfrac{\sigma_{saturation}}{\mu})^{p_\varepsilon}$

4 Plot the Fisher plot $(\dfrac{\sigma_{yield}}{\mu})^{p_\varepsilon}$ and $(\dfrac{\sigma_{saturation}}{\mu})^{p_\varepsilon}$ vs Fisher parameter

$[\dfrac{kT}{\mu b^3}\ln(\dfrac{10^7}{\dot{\varepsilon}})]^{\frac{1}{q_\varepsilon}}$ as shown Fig. 3.1

5 From Eq. 3.2 and Eq. 3.3, we have:

$$\frac{\sigma}{\mu} = \left[1 - (\frac{kT}{g_{0\varepsilon}\mu b^3})^{1/q_\varepsilon}\right]^{1/p_\varepsilon} \frac{\hat{\sigma}}{\mu_0} \tag{3.19}$$

$$\frac{\sigma}{\mu}\frac{\mu}{\hat{\sigma}} = \left[1 - (\frac{kT}{g_{0\varepsilon}\mu b^3})^{1/q_\varepsilon}\right]^{1/p_\varepsilon} \tag{3.20}$$

and we can convert Eq. 3.20 as:

$$(\frac{\sigma}{u})^{p_\varepsilon} = (\frac{\hat{\sigma}}{\mu_0})^{p_\varepsilon} - (\frac{\hat{\sigma}}{\mu_0})^{p_\varepsilon}(\frac{1}{g_{0\varepsilon}})^{\frac{1}{q_\varepsilon}}\left[\frac{kT}{ub^3}\ln\frac{10^7}{\dot{\varepsilon}}\right]^{\frac{1}{q_\varepsilon}} \tag{3.21}$$

In Eq. 3.20, $[\dfrac{kT}{\mu b^3}\ln(\dfrac{10^7}{\dot{\varepsilon}})]^{\frac{1}{q_\varepsilon}}$ is the Fisher parameter.

We can use step (4) Fisher plot to fit Eq. 3.21. With $(\frac{\sigma_{yield}}{\mu})^{p_\varepsilon}$ curve, we can get initial mechanical threshold stress $\hat{\sigma}_{initial}$ and $g_{0\varepsilon 1}$, and using $(\frac{\sigma_{saturation}}{\mu})^{p_\varepsilon}$ curve, we can obtain $\hat{\sigma}_{\varepsilon s}$ and $g_{0\varepsilon 2}$. The physical meanings of $\hat{\sigma}_{initial}$ and $\hat{\sigma}_{\varepsilon s}$ are mechanical threshold stress and saturation stress at 0 K, which are values of the two curves intercepted at the Y axis.

6 Material constant $g_{0\varepsilon}$ can be obtained from taking the average of $g_{0\varepsilon 2}$ and $g_{0\varepsilon 1}$.

$$g_{0\varepsilon} = \frac{(g_{0\varepsilon 1} + g_{0\varepsilon 2})}{2} \tag{3.22}$$

3.3.2 Fitting the hardening parameter θ_0

1 Convert hardening law (Eq. 3.5), $\theta = \frac{d\hat{\sigma}}{d\varepsilon} = \theta_0 (1 - \frac{\hat{\sigma}}{\hat{\sigma}_{\varepsilon s}})^2$ as follows:

$$\theta_0 = \frac{\theta}{(1 - \frac{\hat{\sigma}}{\hat{\sigma}_{\varepsilon s}})^2} \tag{3.23}$$

2 Define θ in term of $\theta^{expriment}$:

Take derivative of Eq. 3.1 $\frac{\sigma}{\mu} = S_\varepsilon \frac{\hat{\sigma}}{\mu_0}$ with respect to the strain:

$$\frac{d\sigma}{d\varepsilon}\frac{1}{\mu} = S_\varepsilon \frac{d\hat{\sigma}}{d\varepsilon}\frac{1}{\mu_0} \tag{3.24}$$

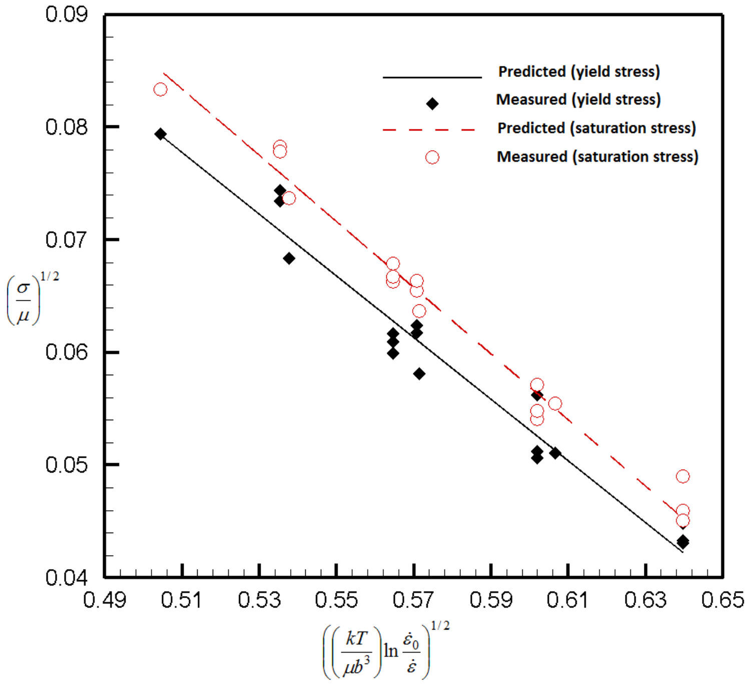

Figure 3.1 Fisher plot (Yield Stress)

Since $\theta = \frac{d\hat{\sigma}}{d\varepsilon}, \theta^{\text{experiment}} = \frac{d\sigma}{d\varepsilon}$, Eq. 3.24 can be converted to:

$$\theta^{\text{experiment}}\frac{1}{\mu} = S_\varepsilon \theta \frac{1}{\mu_0}\text{, or,} \quad \theta = \frac{\mu_0}{\mu}\frac{\theta^{\text{experiment}}}{S_\varepsilon} \tag{3.25}$$

3 Substitute Eq. 3.24 into Eq. 3.25, we get:

$$\theta_0 = \frac{\dfrac{\mu_0}{\mu}\dfrac{\theta^{\text{experiment}}}{S_\varepsilon}}{(1-\dfrac{\hat{\sigma}}{\hat{\sigma}_{\varepsilon s}})^2} \tag{3.26}$$

4 Since θ_0 represents the work hardening at 0 K, $\hat{\sigma}_{initial}$ is used and equation becomes:

$$\theta_0 = \frac{\frac{\mu_0}{\mu}\frac{\theta^{\text{experiment}}}{S_\varepsilon}}{(1-\frac{\hat{\sigma}_{initial}}{\hat{\sigma}_{\varepsilon s}})^2} \tag{3.27}$$

where, $\hat{\sigma}_{initial}$, $\hat{\sigma}_{\varepsilon s}$ and S_ε are from the previous section.

5 Take the average of θ_0 at sample points with different temperature and strain rate:

$$\theta_0 = (\sum_i^n (\theta_0)_i)/n \tag{3.28}$$

θ_0 is plotted in Fig. 3.2 and represents the work hardening at 0 K.

The material parameters of modified MTS model through data fitting are listed Table. 3.1. These parameters will be used in the following PRF simulation.

Table 3.1 Values of material parameters for AA3104-O

Parameter	Unit	AA3104	Parameter	Unit	AA3104
E	*GPa*	58.5	μ_0	*GPa*	2.8815E+4
μ		0.3	μ_d	*GPa*	3440
k		1.38E-20	T_0	*K*	215
b		2.86E-7	$g_{0\varepsilon}$		0.63
m		0.005	$\dot{\varepsilon}_{0\varepsilon}$	s^{-1}	1E+7
p_ε		0.5	q_ε		2
θ_0		89565.53	$\hat{\sigma}_{initial}$	*MPa*	1363
$\hat{\sigma}_{\varepsilon s}$	*MPa*	1587	S_ε	*MPa*	30

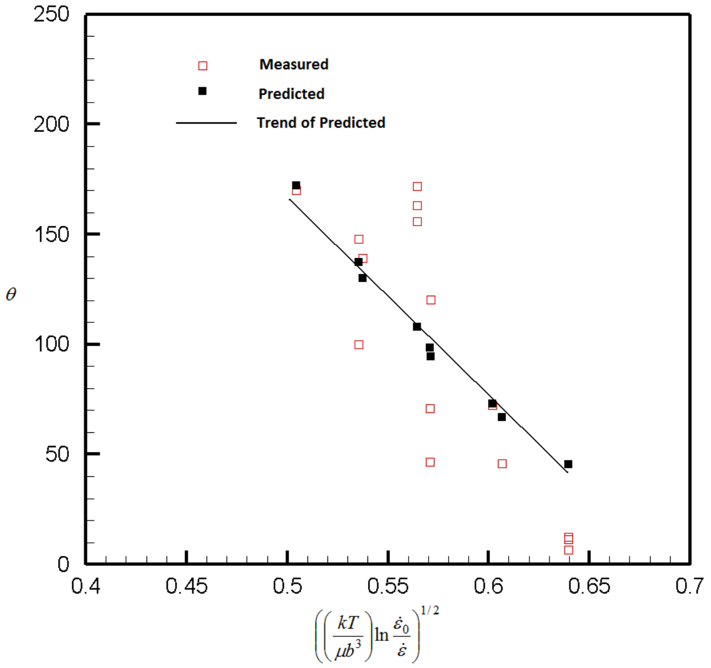

Figure 3.2 Fisher plot (θ)

3.4 Model validation

The formulations discussed in the previous section have been implemented into the general finite element code ABAQUS as user subroutines UMAT and UMATH. The uni-axial tension experimental data for AA3104-O temper aluminum alloy at different strain rates and temperatures have been fitted to the MTS flow law according to the Fisher plot. The uni-axial tensile tests for AA3104-O temper with the same strain rates ($0.127s^{-1}$, $0.0127s^{-1}$ and $0.00127s^{-1}$) at three temperatures (250°C, 300°C and 350°C) are validated against the predicted data through the ABAQUS UMAT. To simplify validation, the temperature increase due to plastic work is ignored in this test. In Fig. 3.3, 3.4 and 3.5, the predicted flow stresses show good agreement with experimental tensile data, at all three temperatures and three strain rates.

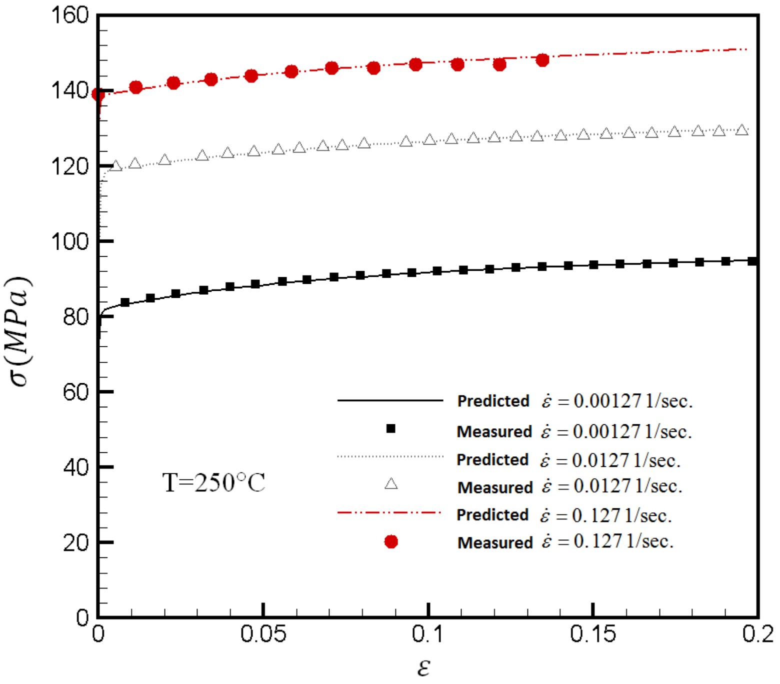

Figure 3.3 Tensile stress response of the sheet under uniaxial tension along the RD, predicted vs measured at T=250°C with various strain rates

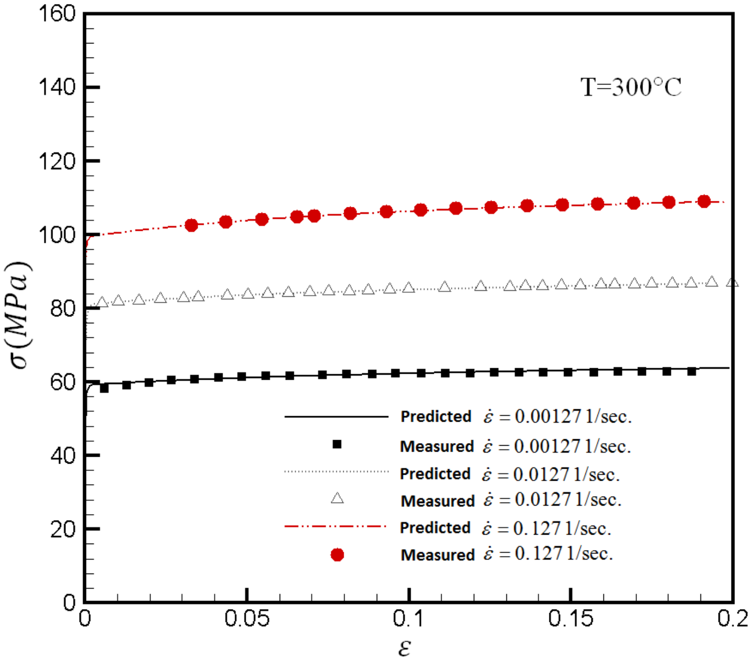

Figure 3.4 Tensile stress response of the sheet under uniaxial tension along the RD, predicted vs measured at T=300°C with various strain rates

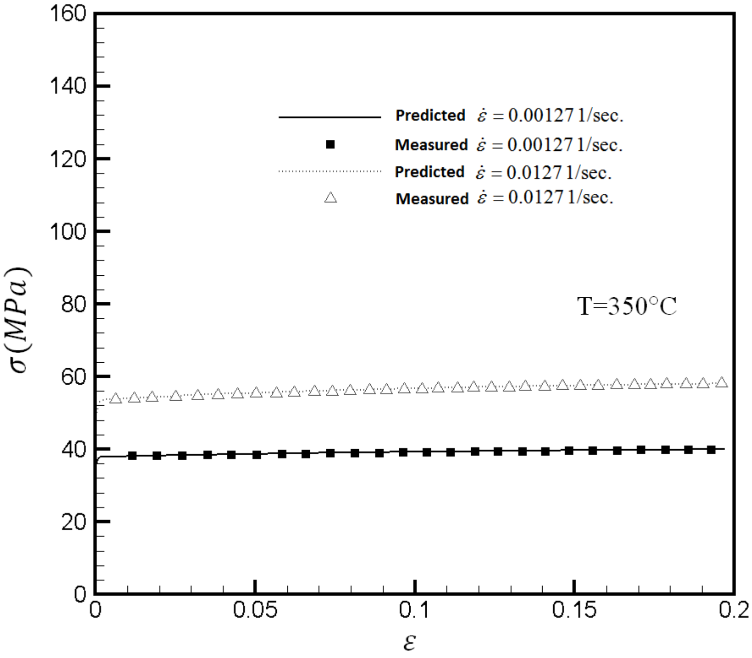

Figure 3.5 Tensile stress response of the sheet under uniaxial tension along the RD, predicted vs measured at T=350°C with various strain rates

3.5 PRF forming

Pressure Ram Forming (PRF^{TM}) is a newly developed, patented hydroforming process for making shaped containers from rolled sheet (Gong et al. (2004)). The first step to make the PRF container is to make a cylindrical preform from a flat sheet using a sequence of forming operations that starts with a blank-and-draw operation and is followed by a series of redraw operations. Then through a series of necking stations, the preform is necked to fit into a PRF mould. A schematic view of draw/redraw operation is shown in Fig. 3.6, and Fig. 3.7 shows the plastic strain accumulation from the first redraw to the third redraw operation during preform manufacture. The second step is to force the preform to expand into the mould under the combined actions of internal pressurization and the motion of a backing ram. The backing ram is a crucial component of the process, as it first ensures that the PRF process proceeds without blowing out the bottom of the preform and finally produces the desired base profile of the container.

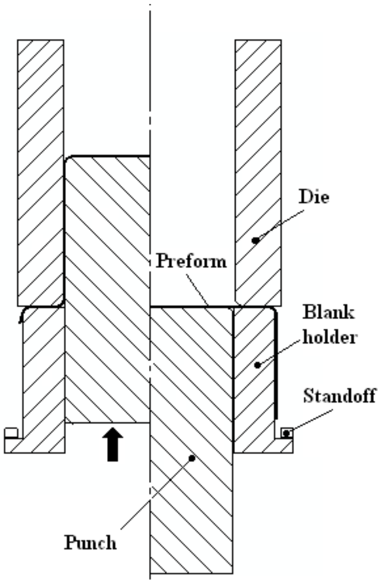

Figure 3.6 Schematic representation of draw/redraw

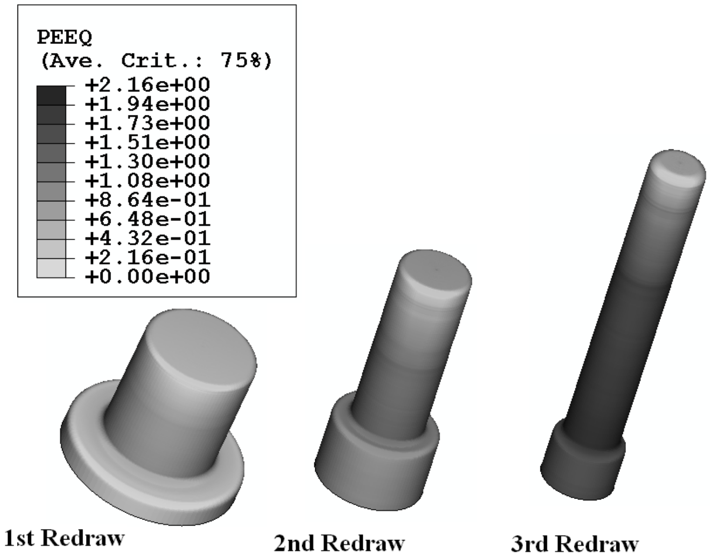

Figure 3.7 Evolutions of plastic strain in the three redraw operations

While the operations in the first step are all conducted at room temperature, the second step is done at high temperatures (a typical PRF forming temperature is between 300°C and 400°C) under various strain rates. The PRF container is formed by using the pressure ram forming apparatus as shown in Fig. 3.8. The apparatus was designed to be flexible for research purposes. Users can easily change the forming time, pressure rate, temperature and temperature distribution to achieve different forming options. The PRF die set was developed to suit various designs. Basically, the die set consists of a mould, seal ram, backing ram and inside heater. Before forming, the mould and backing ram are cleaned and coated with graphite molybdenum sulfide to reduce sticking between the dies and container at elevated temperatures.

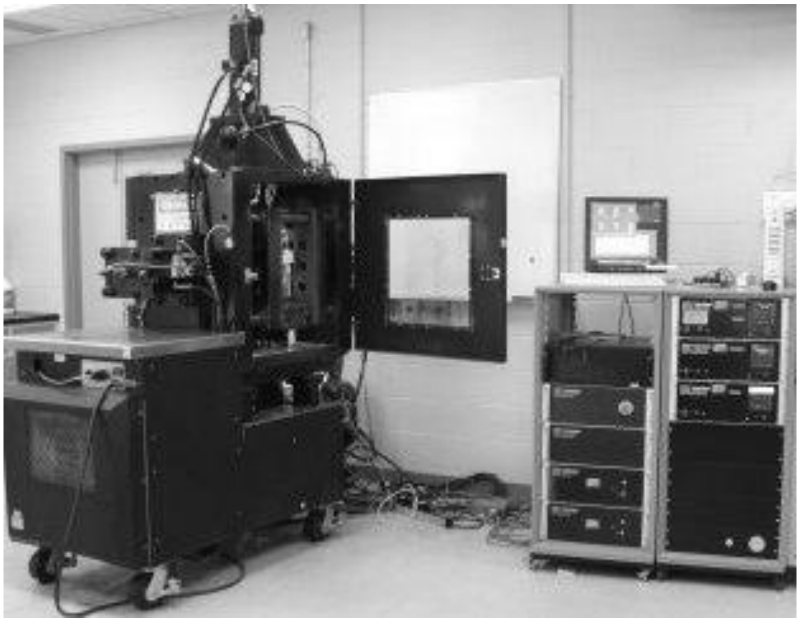

Figure 3.8 Experimental PRF apparatus

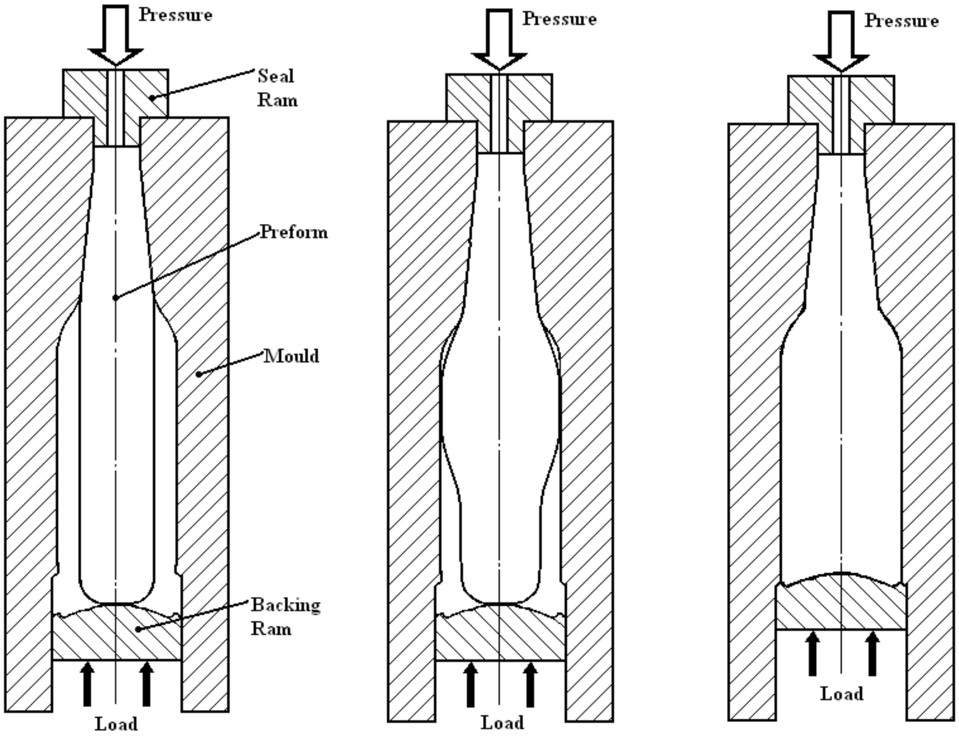

a) Beginning b) During c)Finished

Figure 3.9 Schematic representation of PRF forming procedures

Fig. 3.9 shows the forming procedures for a typical generic PRF container. First, the preform is placed into the shaped cavity formed by the mould and backing ram. This cavity determines the final shape of the body of the PRF container.

The seal ram then closes the preform opening with a preload so that pressure can be applied to the inside. To increase the formability, the preform is fully annealed. The inside heater (not shown) heats the preform to the forming temperature and applies a vertical temperature distribution to the preform at the same time. The temperature distribution determines the location of the onset of bulging and its evolution, since the region of higher temperature is softer and more easily deformed. After the forming temperature is reached, the pressure valve is opened and pressurized gas enters the preform through the inlet of the seal ram (Fig. 3.9a). The preform is forced to expand into the mould under the combined actions of internal pressurization and the motion of the backing ram. The section with higher temperature bulges out first (Fig. 3.9b). Then, this initial bulge propagates along the preform sidewall to fill the mould. At the same time, the backing ram moves up to maintain contact with base of the preform until the whole bottom of the container has been formed (Fig. 3.9c). The backing ram motion is a crucial component of the process, as it first ensures that the PRF process proceeds without blowing out the bottom of the preform and finally produces the desired base profile of the container.

Fig. 3.10 shows the formed generic PRF bottle after forming.

Figure 3.10 Generic PRF bottle

3.6 Finite element modeling of PRF forming

Finite element analysis and simulations have been vital tools in the development of the PRF process. Since the generic container is cylindrical, an axi-symmetric model is used to simulate the PRF process. The preform before PRF forming is about 250 mm long and 38 mm in diameter. The preform has a non-uniform thickness distribution because of the three die necking operations after draw-redraw, which increase the thickness in the neck region. It is expected that this thickness distribution might have a significant effect on the subsequent PRF process. A three-stage die necking model is therefore developed to calculate the metal thickness distribution. The necking model starts with an initial uniform gauge, which is 0.66 mm. The calculated thickness distribution after necking indicates the thickening effect around the neck as shown in Fig. 3.11. This thickness distribution is then assigned to the preform as the initial gauge in the neck region for the PRF forming model. In the PRF model, the preform is meshed using 4-node bilinear axi-symmetric quadrilateral elements with three elements through thickness. The mould and backing ram are treated as rigid bodies. The interfaces between the preform and mould, preform and backing ram are modeled as kinematic contact in ABAQUS/Standard. An elastic Coulomb friction law with coefficient of friction of 0.1 is applied to all contact pairs.

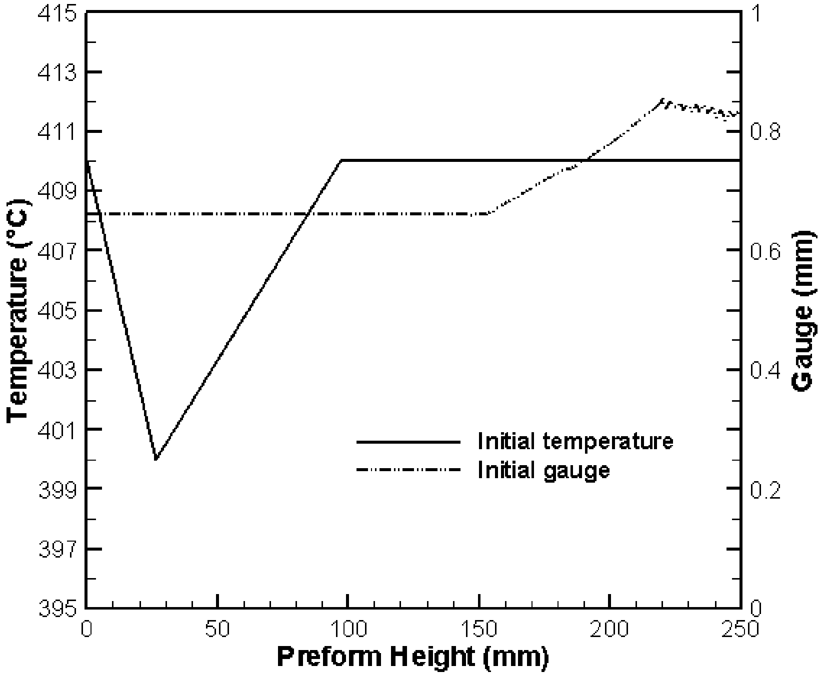

Figure 3.11 Initial temperature distribution and initial gauge on preform, preform initial gauge determined from die necking model

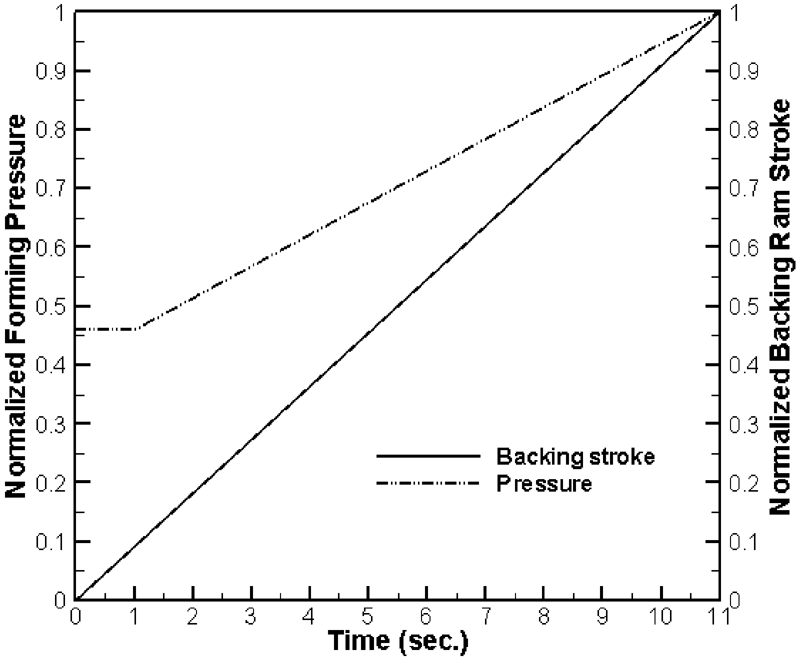

Figure 3.12 PRF loading conditions: normalized forming pressure and backing stroke

The sheet used to make the PRF container is can body stock alloy, AA3104. The values of the material parameters in the MTS model are determined by Fisher plots using elevated temperature tensile tests over a range of strain rates, and are listed in Table 3.1. The boundary and loading conditions are chosen to be the same as the actual forming conditions of the generic PRF container. The normalized forming pressure and normalized backing stroke during the 11 second forming time is shown in Fig. 3.12. The measured initial temperature distributions are assigned to the preform in the model (Fig. 3.11).

Figure 3.13 PRF bottle progression

To validate the FE analysis, a PRF bottle progression is made by stopping the PRF forming process at every second. Fig. 3.13 shows the actual PRF bottle progression during the 11 second period, while Fig. 3.14 presents the predicted generic bottles under the same forming conditions. It is found that the predicted shape evolution agrees well with the experiment. It is also observed, from both the experiment and simulation, that bulging is initiated at the top of the preform, where the section has the highest temperature and is more likely to experience a possible instability due to the preload and backing ram motion. In addition, Fig. 3.14 shows the predicted distributions of the effective plastic strain at different stages. The maximum plastic strain in the final bottle is higher than 0.7.

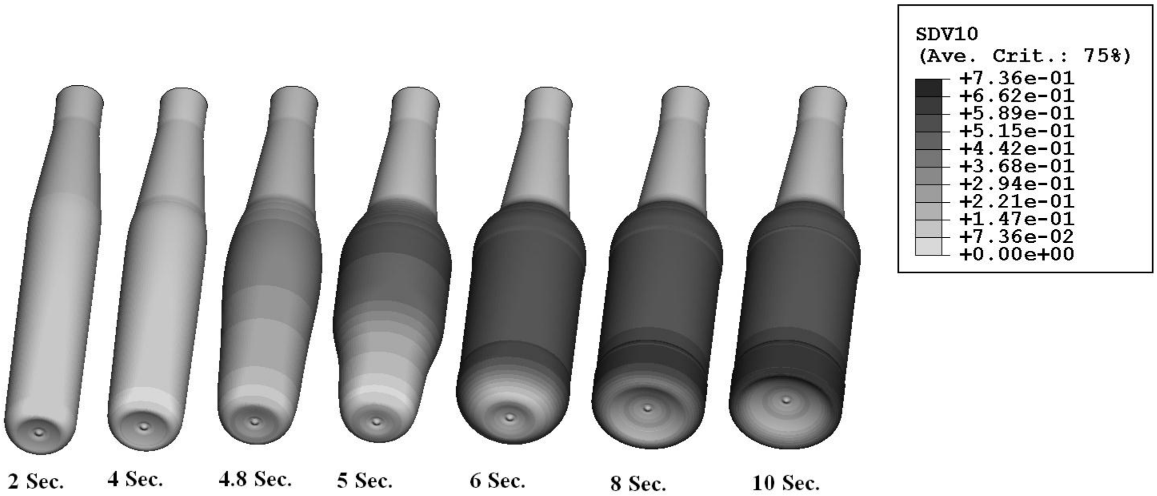

Figure 3.14 Predicted shape and distribution of effective plastic strain during PRF process

Figure 3.15 shows the predicted temperature evolution during the PRF process. To track the temperature evolution at different locations, three elements on the body, shoulder and neck, respectively, are selected. It is found that the element on the body experiences a 13°C increase compared to 9°C on the shoulder although the starting temperatures are the same. This is because the element on the body experiences a larger plastic strain than the element on the shoulder does. After both elements contact the die (after 6 seconds), they cool down a bit due to the heat loss through conduction. The temperature on the neck, however, increases slowly but monotonically during the whole forming process. This is because of the relatively small plastic deformation that this element experiences. These results agree well with experimental observations.

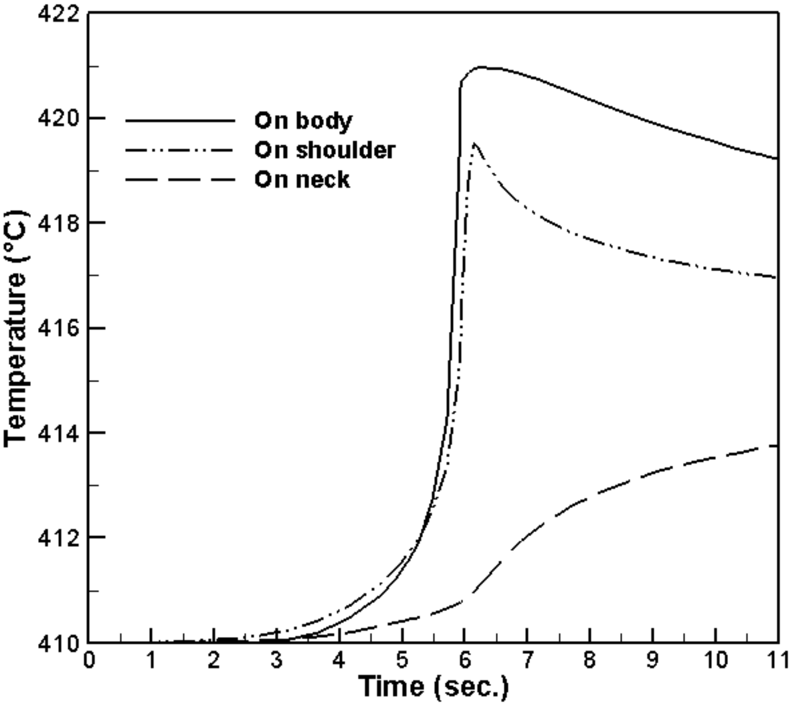

Figure 3.15 Calculated temperature evolution during PRF process

The development of strain components in the sidewall during the forming process is shown in Fig. 3.16. It is found that the hoop strain is always positive (expansion), while the radial strain is always compressive (thinning). The axial strain is compressive at the beginning due to the force of the backing ram motion. It becomes positive when the sidewall starts to bulge out (around 6 seconds).

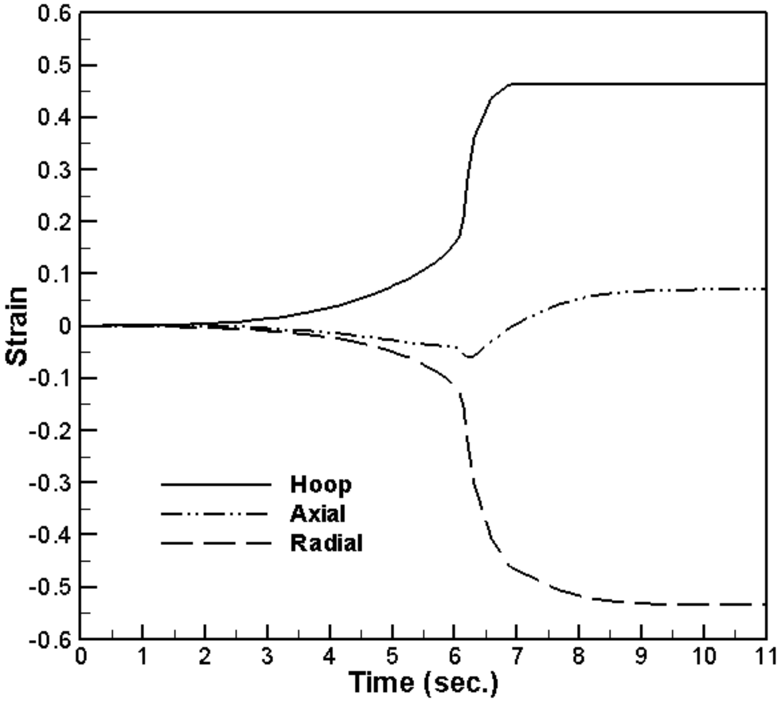

Figure 3.16 Predicted strain evolution on the sidewall

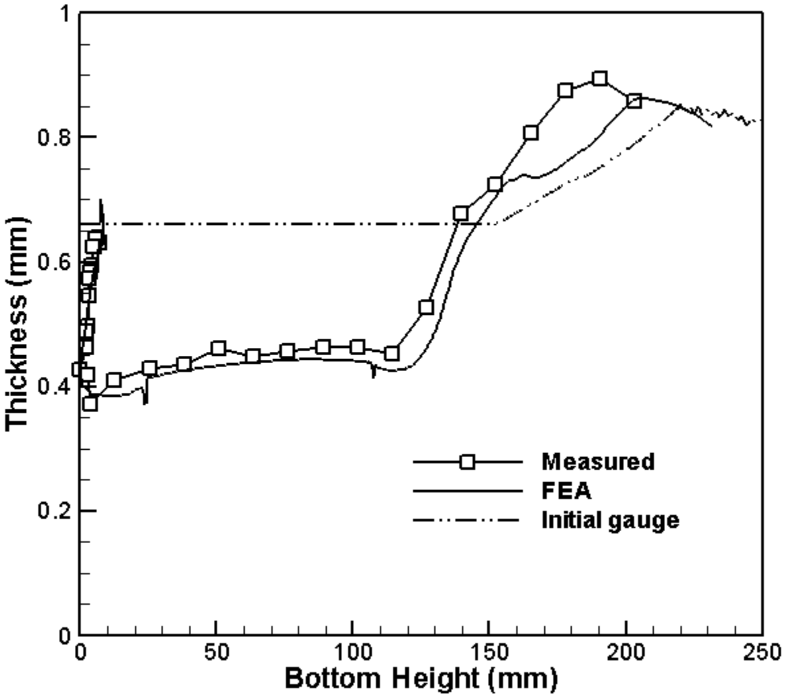

Figure 3.17 Measured and calculated thickness profiles

To study the thickness profile after forming, a formed PRF bottle is cut longitudinally to facilitate thickness measurement. Fig. 3.17 shows the measured and predicted thickness versus bottom height. It is clear that the predicted thickness is in reasonably good agreement with the measurement. Both measured and FE predicted bottles are shorter than the preform since the backing ram pushes up the preform to fill the metal into the mould during PRF process. Also, the predicted thickness is less in the shoulder and neck region (bottom height: 130mm to 240mm) than measured. The reason for the thickness difference in the neck is that the measured bottle was shortened slightly by excessive compression during a subsequent crowning operation after PRF forming. Since the independent axis in Fig. 3.17 is the distance from the bottom, the points at which the neck thickness is measured have been shifted to the left on the graph. The FEA simulation does not include the crowning operation.

The measured bottle also shows more thinning at the bottom nose region compared with the simulation because of the thinning effect during draw and redraw operations. The simulation doesn’t take into account thinning introduced during draw-redraw operations.

The reaction force on the backing ram during the forming process also serves as a signature of the PRF process. Fig. 3.18 shows the comparison of backing load between the simulation and experiment. Generally speaking, the prediction gives a reasonably good agreement with the measurement. More specifically, both experiment and simulation indicate that the backing load increases, from the preload (600 N), when the internal pressure is on and the ram pushes up.

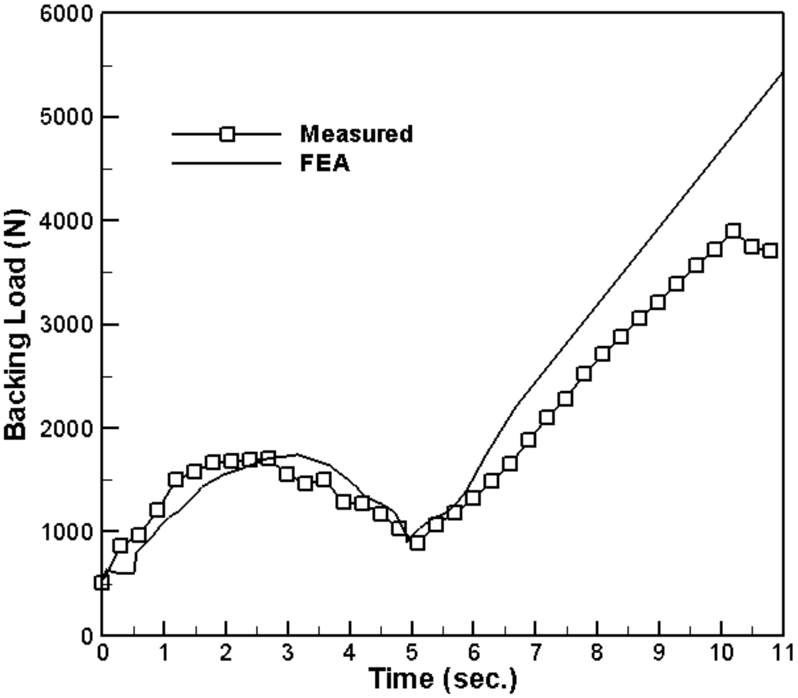

Figure 3.18 Measured and calculated backing loads

When the preform starts to expand at the middle of the container, the backing load decreases slightly until the preform contacts the mould and backing load increases again. It is also observed, from Fig. 3.18, that the container bottom profile has been fully formed in the last 5 seconds. However, the simulation tends to over-predict the backing load. This is because the perform is thinner at the bottom nose due to the draw-redraw operations. The thinner gauge at the bottom nose makes it easier to form the whole base profile. However, the finite element prediction starts with uniform gauge (0.66 mm) at the preform base region (preform drawing-redrawing simulations are not performed) and more force is required on the backing ram to form the base of the PRF container.

3.7 Conclusion of PRF modeling

The pressure ram forming process has been simulated by implementing the MTS model in ABAQUS through a user material subroutine (UMAT). The predicted shape, thickness distribution and backing load of the PRF aluminum bottle were found to be in good agreement with measurements. It has been demonstrated that the MTS model is able to accurately describe the coupled thermal-mechanical behavior for can body stock at elevated temperatures (300°C to 400°C) under various strain rates.

This research work has been published (Shi et al. (2007)) and its industrial patent applications was issued in 2011 (Mallory & Shi (2011)).

Chapter 4

Prediction of Localized Necking Failure in Aluminum Tube

4.1 Review of elastic-plastic constitutive formulation for single crystal plasticity

4.1.1 Introduction

A crystal plasticity based constitutive model has been developed to explain heterogeneous plastic deformation, large lattice rotation within shear bands when a sample is subjected to stress. In this method, the continuum mechanical behavior of the material is specified by finite strain crystal plasticity, while the self-hardening and microstructure evolution within each slip system is defined by a local crystal orientation with respect to the global system due to global deformation. The model is also extended to simulate plastic deformation in poly-crystals.

Convention of crystallographic orientation:

In the face centered cubic aluminum crystal structure, twelve slip systems can be initiated. The initial crystallographic orientation is defined with three angles, $\varphi_1, \varphi, \varphi_2$ to track its evolution. These three angles are defined as the rotation angle of [100], [010] and [001], respectively. Four slip planes and three slip directions on each slip plane are defined as in Fig. 4.1. This combination gives twelve slip systems as listed in Table 4.1

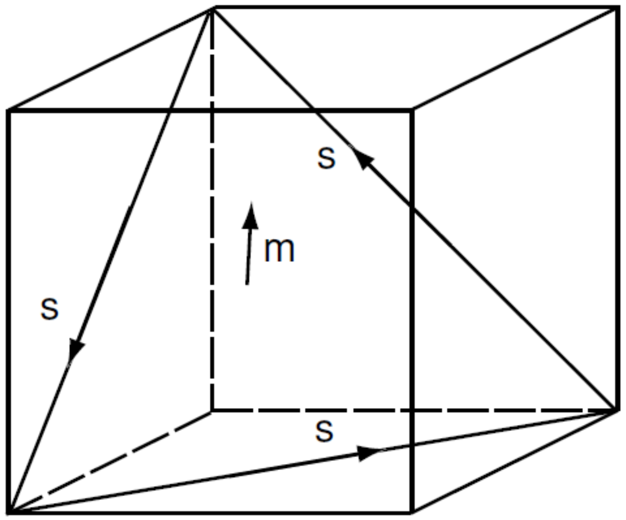

Figure 4.1 Slip planes and slip direction in a single crystal

Table 4.1 Slip direction s^α and slip planes m^α for 12 slip systems

α	s^α	m^α	α	s^α	m^α	α	s^α	m^α
1	$[01\bar{1}]$	(111)	**5**	$[101]$	$(\bar{1}11)$	**9**	$[\bar{1}\bar{1}0]$	$(\bar{1}1\bar{1})$
2	$[\bar{1}01]$	(111)	**6**	$[\bar{1}\bar{1}0]$	$(\bar{1}11)$	**10**	$[011]$	$(11\bar{1})$
3	$[1\bar{1}0]$	(111)	**7**	$[011]$	$(\bar{1}1\bar{1})$	**11**	$[1\bar{1}0]$	$(11\bar{1})$
4	$[01\bar{1}]$	$(\bar{1}11)$	**8**	$[10\bar{1}]$	$(\bar{1}1\bar{1})$	**12**	$[101]$	$(11\bar{1})$

4.1.2 Kinematics

The kinematical theory for the mechanics of crystal plasticity follows the work of Taylor and its precise mathematical theory developed by Hill (1966), Rice (1971) and Hill and Rice (1972). The following is a simple summary of the theory, followed Asaro and Rice (1977), Aeroso (1983) and Huang (1991).

A crystalline material is embedded on a lattice which undergoes elastic deformation and rotation. The inelastic deformation of a single crystal is assumed here to arise solely from crystalline slip in Fig. 4.1. The material flows through the crystal lattice via dislocation motion. The total deformation gradient $\mathbf{F}$ is given by:

$$\mathbf{F} = \mathbf{F}^{*}\mathbf{F}^{\mathbf{p}} \tag{4.1}$$

where $\mathbf{F}^{\mathbf{p}}$ describes the flow material by slip while the crystal lattice and its elastic properties remain unaffected and $\mathbf{F}^{*}$ represents the elastic as well as any rigid body deformation of the lattice and material together. Thus, when the elastic deformation and the rotation of the lattice are removed (restoring the lattice to its unreformed state), the permanent deformation of the material is represented by $\mathbf{F}^{\mathbf{p}}$. The velocity gradient, $\mathbf{L}$, is then defined and decomposed according to:

$$\mathbf{L} = \dot{\mathbf{F}}\mathbf{F}^{-1} = \mathbf{L}^{*} + \mathbf{L}^{\mathbf{p}} \tag{4.2}$$

with

$$\mathbf{L}^{*} = \dot{\mathbf{F}}^{*}\mathbf{F}^{*-1},\ \mathbf{L}^{\mathbf{p}} = \mathbf{F}^{*}\dot{\mathbf{F}}^{\mathbf{p}}\mathbf{F}^{\mathbf{p}-1}\mathbf{F}^{*-1} \tag{4.3}$$

where a superposed dot is used to denote derivatives with respect to time at a fixed material point, and the superscript -1 to denote the inverse. The symmetric and anti-symmetric parts of the velocity gradients will be identified by the rate of deformation tensors $\mathbf{D},\mathbf{D}^{\mathbf{p}},\mathbf{D}^{*}$ and spin rates $\mathbf{\Omega},\mathbf{\Omega}^{\mathbf{p}},\mathbf{\Omega}^{*}$, given by:

$$\mathbf{D}^{*} + \mathbf{\Omega}^{*} = \dot{\mathbf{F}}^{*}\mathbf{F}^{*-1}, \quad \mathbf{D}^{\mathbf{p}} + \mathbf{\Omega}^{\mathbf{p}} = \mathbf{F}^{*}\dot{\mathbf{F}}^{\mathbf{p}}\mathbf{F}^{\mathbf{p}-1}\mathbf{F}^{*-1} \tag{4.4}$$

which also implies the decompositions:

$$\mathbf{D} = \mathbf{D}^{*} + \mathbf{D}^{\mathbf{p}}, \qquad \mathbf{\Omega} = \mathbf{\Omega}^{*} + \mathbf{\Omega}^{\mathbf{p}} \tag{4.5}$$

The particular slip system α is identified by the orthonormal vectors $\mathbf{s}_{\boldsymbol{\alpha}}$ and $\mathbf{m}_{\boldsymbol{\alpha}}$, along the slip direction and slip-plane normal, respectively. The current values of the slip system vectors and their evolutions are given by:

$$\mathbf{s}_{\boldsymbol{\alpha}}^{*} = \mathbf{F}^{*}\mathbf{s}_{\boldsymbol{\alpha}}, \qquad \dot{\mathbf{s}}_{\boldsymbol{\alpha}}^{*} = \mathbf{L}^{*}\mathbf{s}_{\alpha}^{*}$$

$$\mathbf{m}_{\boldsymbol{\alpha}}^{*} = \mathbf{m}_{\boldsymbol{\alpha}}\mathbf{F}^{*-1}, \qquad \dot{\mathbf{m}}_{\boldsymbol{\alpha}}^{*} = -\mathbf{L}^{*\mathbf{T}}\mathbf{m}_{\alpha}^{*} \tag{4.6}$$

where the superscript T denotes the transpose.

If $\dot{\gamma}_{\alpha}$ denotes the rate of shearing with respect to the current slip system vectors $\mathbf{s}_{\boldsymbol{\alpha}}^{*}$ and $\mathbf{m}_{\boldsymbol{\alpha}}^{*}$ of the slip system α, then:

$$\mathbf{D}^{\mathbf{p}} + \mathbf{\Omega}^{\mathbf{p}} = \sum_{\alpha=1}^{n}\dot{\gamma}_{\alpha}\mathbf{s}_{\boldsymbol{\alpha}}^{*} \otimes \mathbf{m}_{\boldsymbol{\alpha}}^{*} \qquad \text{`} \tag{4.7}$$

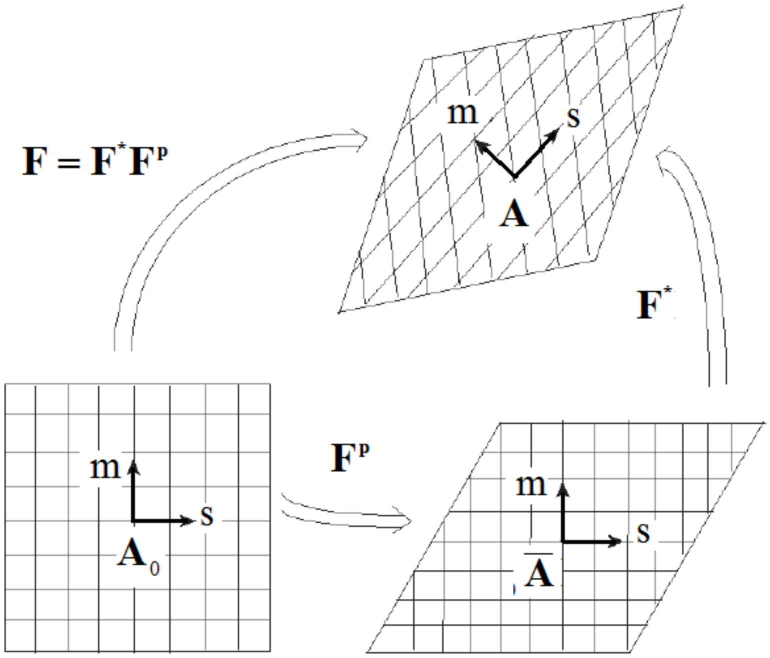

Figure 4.2 Kinematics of elasto-plastic deformation

where the sum extends over the active slip systems. Using Eq. 4.4, Eq. 4.6 and Eq. 4.7 furnishes the evolution equations for $\mathbf{F}^\mathbf{p}$:

$$\dot{\mathbf{F}}^\mathbf{p}\mathbf{F}^{\mathbf{p}-\mathbf{1}} = \sum_{\alpha=1}^{n} \dot{\gamma}_\alpha \mathbf{s}_\alpha^* \otimes \mathbf{m}_\alpha^* \tag{4.8}$$

Define the sysmmetric and anti-symmetric tensors $\mathbf{P}_\alpha$ and $\mathbf{W}_\alpha$ for each slip system as:

$$\mathbf{P}_\alpha = \frac{1}{2}\left(\mathbf{s}_\alpha^* \otimes \mathbf{m}_\alpha^* + \mathbf{m}_\alpha^* \otimes \mathbf{s}_\alpha^*\right),\ \mathbf{W}_\alpha = \frac{1}{2}\left(\mathbf{s}_\alpha^* \otimes \mathbf{m}_\alpha^* - \mathbf{m}_\alpha^* \otimes \mathbf{s}_\alpha^*\right) \tag{4.9}$$

and

$$\mathbf{D^p} = \sum_{\alpha=1}^{n} \dot{\gamma}_\alpha \mathbf{P_\alpha}, \qquad \mathbf{\Omega^p} = \sum_{\alpha=1}^{n} \dot{\gamma}_\alpha \mathbf{W_\alpha} \tag{4.10}$$

4.1.3 Constitutive model

In the rate-dependent crystal plasticity model employed, the elastic constitutive equation for each grain is specified by:

$$\overset{\nabla *}{\boldsymbol{\sigma}} + \boldsymbol{\sigma}(\mathbf{I} : \mathbf{D}^*) = \mathbf{L} : \mathbf{D}* \tag{4.11}$$

where $\mathbf{I}$ is the second order identical tensor, $\mathbf{L}$ is the tensor of elastic moduli having the full set of symmetries, $\overset{\nabla *}{\boldsymbol{\sigma}}$ is the Jaumann rate of true stress, which is the corotational stress rate on axes that rotate with the crystal lattice, and is related to the corotational stress rate on axes rotating with the material, $\overset{\nabla}{\boldsymbol{\sigma}}$ by:

$$\overset{\nabla *}{\boldsymbol{\sigma}} = \overset{\nabla}{\boldsymbol{\sigma}} + \left(\mathbf{\Omega} - \mathbf{\Omega}^*\right) \cdot \boldsymbol{\sigma} - \boldsymbol{\sigma} \cdot \left(\mathbf{\Omega} - \mathbf{\Omega}^*\right) \tag{4.12}$$

The crystalline slip is assumed to obey Schmid's law, i.e. the slipping $\dot{\gamma}_{(\alpha)}$ in any particular slip system α is assumed to depend on the current $\boldsymbol{\sigma}$ through the Schmid stress $\boldsymbol{\tau}_{(\boldsymbol{\alpha})}$. The Schmid stress is just the resolved shear stress when elastic lattice distortions are negligible. There are many possible generalizations in the presence of the finite elastic distortions as discussed by Asaro and Rice (1977). Here, Rice's (1971) version has been used as:

$$\boldsymbol{\tau}_{(\boldsymbol{\alpha})} = \mathbf{m}^{*}_{(\boldsymbol{\alpha})} \cdot \frac{\rho_0}{\rho} \boldsymbol{\sigma} \cdot \mathbf{s}^{*}_{(\boldsymbol{\alpha})} \tag{4.13}$$

Where ρ_0 and ρ are the mass density in the reference and current states. The rate of change of this Schmid stress is given by:

$$\dot{\boldsymbol{\tau}}_{(\boldsymbol{\alpha})} = \mathbf{m}^{*}_{(\boldsymbol{\alpha})} \cdot \left[\overset{\nabla^{*}}{\boldsymbol{\sigma}} + \boldsymbol{\sigma}(\mathbf{I} : \mathbf{D}^{*}) - \mathbf{D}^{*} \cdot \boldsymbol{\sigma} + \boldsymbol{\sigma} \cdot \mathbf{D}^{*} \right] \boldsymbol{\sigma} \cdot \mathbf{s}^{*}_{(\boldsymbol{\alpha})} \tag{4.14}$$

4.1.4 Hardening law of rate-dependent crystalline materials

It has been noted by Peirce, Aero and Needleman (1984) that rate-independent plasticity may be treated as the limit of rate-dependent viscoplasticity. The hardening of a single crystal has been discussed by many authors (Asaro, 1983, Wu, 1997 &2004b). Base on the Schmid law, the slipping rate $\dot{\gamma}_{(\alpha)}$ of the n$^{\text{th}}$ slip system in a rate dependent crystalline solid is determined by the corresponding resolved shear stress $\tau_{(\alpha)}$. Using the simple power law relation, the slip rates can be governed by the power-law expression:

$$\dot{\gamma}_{(\alpha)} = \dot{\gamma}_{(0)} \mathrm{sgn} \left| \frac{\tau_{(\alpha)}}{\mathrm{g}_{(a)}} \right|^{1/m} \tag{4.15}$$

where $\dot{\gamma}_{(0)}$ is a reference shear rate taken to be the same for all the slip systems, τ is the resolved shear stress on slip system α , $\mathrm{g}_{(\alpha)}$ is its hardness and *m* is the strain-rate sensitivity index. The $\mathrm{g}_{(\alpha)}$ characterizes the current strain hardened state of the crystal.

The strain hardening is characterized by the evolution of strengths $\mathrm{g}_{(\alpha)}$ through the incremental relation. For multiple slips, the evolution of the hardness is governed by:

$$\dot{\mathrm{g}}_{(\alpha)} = \sum_{\beta} \mathrm{h}_{(\alpha\beta)} \left| \dot{\gamma}_{(\beta)} \right| \tag{4.16}$$

where $\mathrm{g}_{(\alpha)}(0)$ is the initial hardness, taken to be a constant τ_0 for each slip system, and $h_{(\alpha\beta)}$ is the hardening moduli. The form of these moduli is:

$$h_{(\alpha\beta)} = q_{(\alpha\beta)} h_{(\beta)} \tag{4.17}$$

where $h_{(\alpha\beta)}$ is a single slip hardening rate and $q_{(\alpha\beta)}$ is the matrix describing the latent hardening behavior of the crystal. The latter is determined by a latent hardening parameter $q \geq 1$, if $q = 1$, the hardening is isotropic. The following slip hardening rate is used:

$$h_{(\beta)} = h_{(0)} \left(1 - \frac{g_{(\beta)}}{\tau_s} \right)^a \tag{4.18}$$

where $h_{(0)}$, a and τ_s are the slip system hardening parameters, which are taken to be identical for all slip systems.

In this formulation, there is no explicit yielding. If the resolved shear stress on a system is non-zero, then plastic shearing occurs.

4.2 Simulation of tube hydroforming with crystal plasticity

A plane strain crystal plasticity based finite element model has been developed to simulate localized necking in an aluminum tube under internal pressure. The measured EBSD data for the sheet are mapped to the tube and then directly incorporated into the finite element model and the constitutive response at an integration point is described by the single crystal plasticity theory.

4.2.1 Problem formulation and method of solution

Fig. 4.3a shows a rolled sheet with the rolling direction denoted by RD, the transverse direction TD and the normal direction, ND. We assume that the EBSD was performed on a small region in the ND-TD section (N.T. section), as illustrated in Fig. 4.3a. The EBSD step sizes were taken to be the same as the grain sizes in the TD and ND, respectively. An orientation in the EBSD map thus represented a grain. The model region (marked in Fig. 4.3a), with the initial length L_0 along the TD and the initial thickness H_0 in the ND, is mapped into one quadrant of a tube with the inner radius $R_I = \frac{2L_0}{\pi} - H_0$ and thickness H_0 (Fig. 4.3b). During this mapping, the orientation of a grain is rotated α degrees around the RD according to the initial position of the centre of the grain in the marked region and the corresponding position in the tube. To permit inhomogeneous deformation within the grains, each grain in the tube is further sub-divided into $N_{g_\alpha} \times N_{gR}$ elements (N_{g_α} elements in the hoop direction and N_{gR} in the radius direction). The mapped region (one quadrant of the tube) is meshed with $N_{g_\alpha} \times N_{gR}$

regular elements (N_{g_α} elements in the hoop direction and N_{gR} elements in the radius direction), as showed in Fig. 4.3b. Rotated orientations from the measured EBSD data are assigned to the grains in the mesh according to their corresponding positions. All $N_{g_\alpha} \times N_{gR}$ elements within each grain are assigned the same initial orientation. In other words, a set of $N_{g_\alpha} \times N_{gR}$ elements of the mesh represents an orientation/grain from the measured EBSD data, which has a total of $\lfloor (N_\alpha / N_{g\alpha}) \times (N_R / N_{g\mathrm{R}}) \rfloor$ orientations/grains.

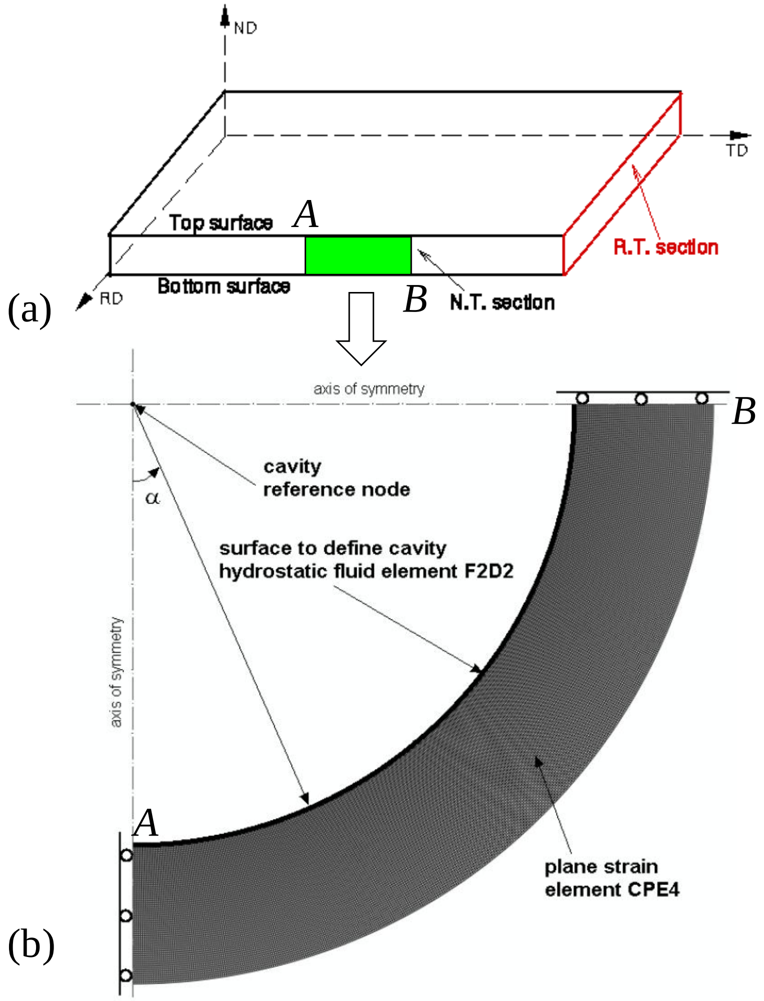

Figure 4.3 Schematic representations of a marked region in a sheet (a), and one quadrant of a tube mapped from the marked region (b)

We assume that across grain boundaries there is perfect bonding without sliding, but across the boundaries the initial lattice orientations experience a jump. The single crystal constitutive model gives the constitutive response at an integration point.

It is worth mentioning that grains in the sheet are modeled as squares. It is noted that if the EBSD step size is much smaller than the grain size, the effect of grain shape on surface instability and necking can be included in the simulation. This implies that a very fine mesh with many elements must be used. However, a computation with a very large number of elements and based on the crystal plasticity theory exceeds the computer capabilities for most research institutes. On the other hand, the effect of grain shape on surface roughening and necking in the sheet under plane strain tension along the TD was found to be small (Wu and Lloyd, 2004; Wu et al., 2007). It is thus expected that the influence of grain shape on necking in the present paper should be small. We assume that the tube under internal pressure is very long and that there is no deformation in the axial direction, i.e. the tube is in a plane strain deformation state. The overall response of the tube under internal pressure is represented by pressure p and the normalized minimum cross sectional area $(A_{\min}/A_0)$ as functions of the volume strain, $\varepsilon_V = \ln\sqrt{\frac{V}{V_0}}$. Here, A_0 and V_0 are the initial cross-sectional area and volume enclosed by the inner surface of the tube. The volume per unit tube length is computed by

$$V = \frac{1}{2}\int_S \alpha^{ij} n_j (x_i + u_i) dS \tag{4.19}$$

where S is the inner surface of cylinder in the initial state; x_i are the initial Cartesian coordinates of the point on the surface; n_j is the normal vector and α^{ij} is the configuration tensor (Sewell, 1967). It is noted that the volume strain ε_υ is actually the averaged hoop strain on the inner surface of the tube.

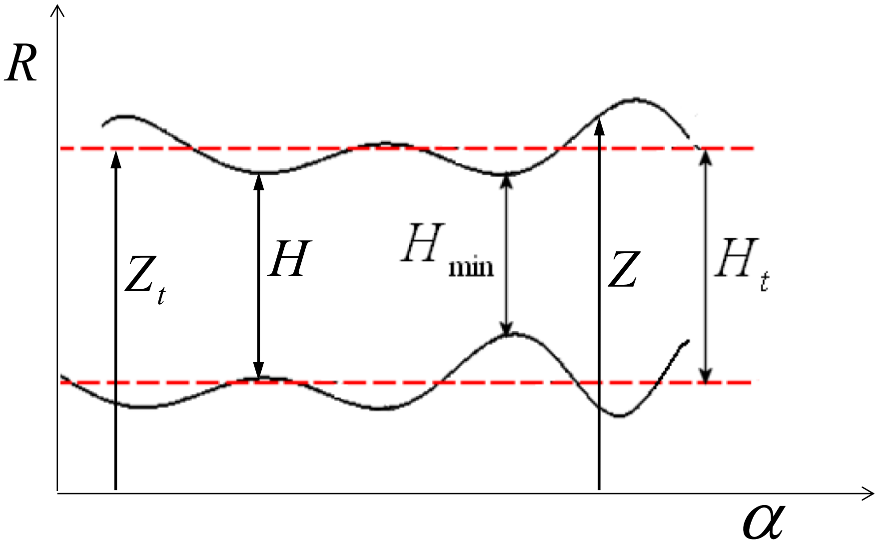

Figure 4.4 Schematic representations of surface topographies of a tube in deformed state

For the plane strain deformation considered, we have

$$A_{\min}/A_0 = H_{\min}/H_0 \tag{4.20}$$

where $H_{\min}$ is the minimum thickness as shown in Fig. 4.4 and H_0 is the initial thickness. For further reference, we define H and H_t as local thicknesses at α and the averaged thickness, respectively. In Fig. 4.4, Z and Z_t are respectively the radius of the outer surface at α and the averaged outer radius. The surface profile of the outer surface is defined as:

$$\Delta Z = Z - Z_t \tag{4.21}$$

The hydrostatic fluid enclosed by the inner surface of the tube is modeled by the hydrostatic fluid elements (F2D2 in ABAQUS/Standard), while the tube is meshed by plane strain elements (CPE4 in ABAQUS/Standard). The hydrostatic fluid elements define the cavity enclosed by the inner surface of the tube and provide coupling between deformation of fluid-filled tube and the pressure exerted by the contained fluid on the inner surface of the tube. The response of the tube depends on the pressure exerted by the fluid, which in turn is affected by the deformation of the tube. The hydrostatic fluid elements and solid elements share their nodes with the inner surface of the tube. Fig. 4.3b shows the quadrant of the tube to be studied with $\alpha = 0$ and 90^0 as symmetric planes.

4.2.2 Results and discussions

We consider commercial AA6111-T4 sheet at a gauge of about 0.9 mm. The sheet is recrystallized, with an average grain size of the order of 30 μm along the TD and 20 μm in the ND. The initial texture of the sheet is shown in Fig. 4.5 in terms of the {111} pole figure. It is generated from the measured EBSD data, which was obtained from a region about 5.89 mm by 0.89 mm in the N.T. section of the sheet (see Fig. 4.2a). It is noted that the sheet has an extremely high Cube texture. Fig. 4.6 shows the volume fraction profile of texture component Cube along the TD in the N.T. section. Here, we define the volume fraction profile as the averaged volume fraction over the thickness (in the ND) and this is plotted against the TD in Fig. 4.6. It is clear that the spatial distribution of Cube is inhomogeneous.

The values of the hardening parameters were determined by curve-fitting numerical simulations of uni-axial tension in the RD to the corresponding experimental data. Fig. 4.7 shows that the curve fitting is very good. In the simulation deformation is assumed to be homogeneous, and the Taylor-type polycrystal plasticity is performed on textures measured by X-ray and EBSD. It is found that the results based on the X-ray and EBSD are very similar, indicating both texture measurements are reliable. The values for the material parameters in the crystal plasticity analysis are listed in Table. 4.2 below.

Table 4.2 Values of material parameters for AA6111-T4

Parameter	Unit	AA6111	Parameter	Unit	AA6111
C_{11}	*GPa*	236	τ_0	*MPa*	48
C_{12}	*GPa*	135	h_0	*MPa*	432
C_{44}	*GPa*	62	τ_s	*MPa*	122.4
$\dot{\gamma}_0$	s^{-1}	0.001	a		1.3
m		0.007	q		1.4

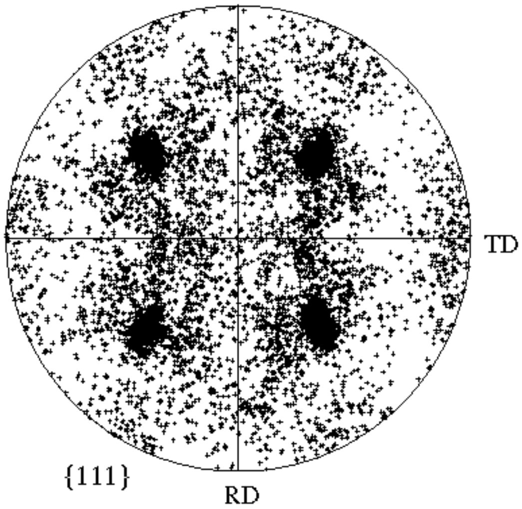

Figure 4.5 Initial texture represented in terms of {111} pole figure

It is noted that the crystal elastic constants, the strain-rate sensitivity, m, and the slip system reference plastic shearing rate, $\dot{\gamma}_0$, are in the typical range for rolled aluminum alloys. The values of the hardening parameters were determined by curve-fitting numerical simulations of uni-axial tension in the RD to the corresponding experimental data. It should be emphasized, however, that the main purpose of this paper is to develop a crystal plasticity based finite element model to predict localized necking in a tube under internal pressure, and the overall conclusions are not particularly dependent on the values of the material parameters.

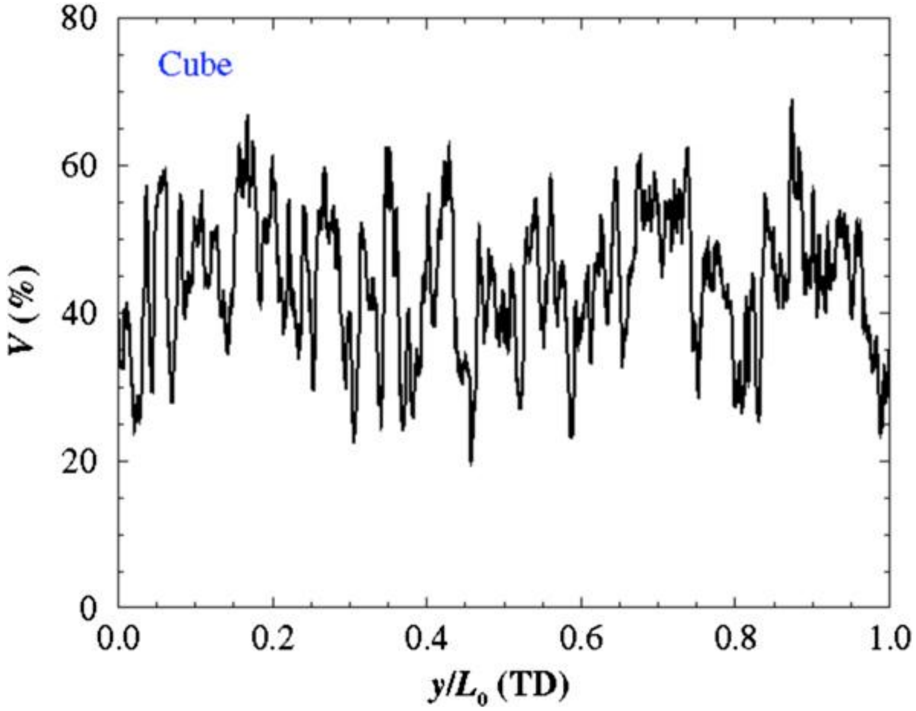

Figure 4.6 Volume fraction profile of Cube along the TD in the N.T section

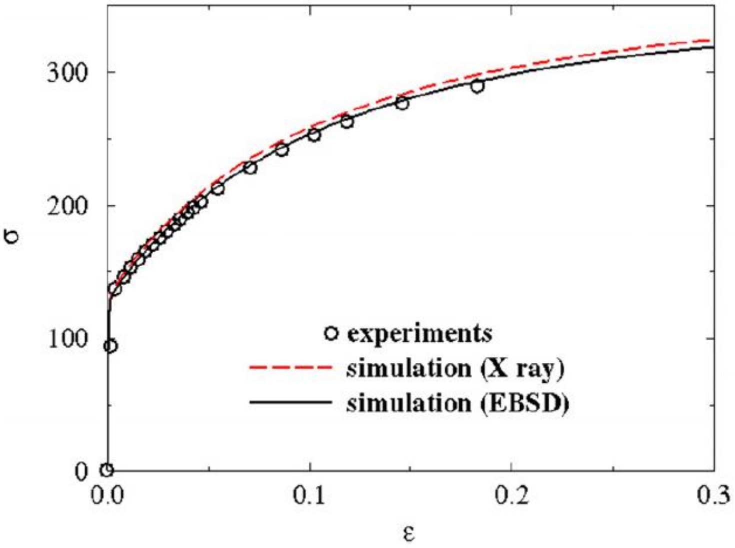

Figure 4.7 Tensile stress response of the sheet under uniaxial tension along the RD

The EBSD measurements are mapped onto one quadrant of a tube with the inner radius $R_I = \frac{2L_0}{\pi} - H_0 \cong 2.86$ mm and thickness $H_0 = 0.89$ mm. The tube is assumed sufficiently long, so that length changes as well as end effects can be ignored and hence a plane strain analysis can be performed. Pressurization is controlled by prescribing a function of the volume strain ε_V . In this simulation, each initial orientation/grain is represented by $N_{g\alpha} \times N_{g\mathrm{R}} = 3 \times 2$ elements in a mesh with a total of $N_\alpha \times N_R = 456 \times 68$ elements for a total of $\lfloor (N_\alpha / N_{g\alpha}) \times (N_R / N_{g\mathrm{R}}) \rfloor = 152 \times 34$ orientations/grains. In Fig. 4.8, the maximum pressure and onset of necking are marked by solid square and open circle, respectively. The reason for defining the location of the open circle as the surface instability point or localized necking point is highlighted in Fig. 4.9, which shows the predicted minimum cross sectional area $A_{\boldsymbol{min}} / A_0$ as a function of the volume strain ε_V .

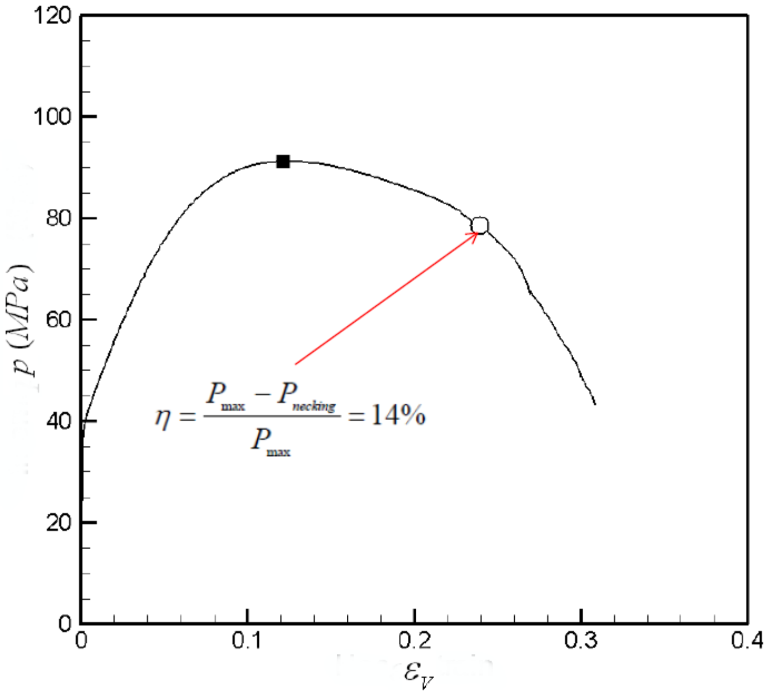

Figure 4.8 Predicted internal pressure p as a function of volume strain ε_V

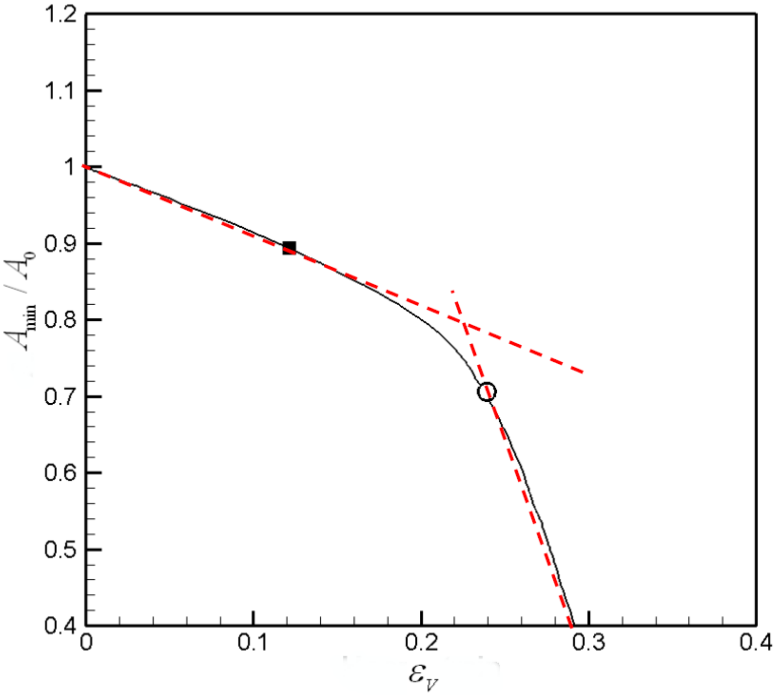

Figure 4.9 Predicted normalized minimum cross-sectional area A_{min}/A_0 as a function of volume strain ε_V

It is observed, from Fig. 4.9, that there is a bi-linear relationship between the minimum cross sectional area and the volume strain. The first straight line ends at a point somewhat beyond the maximum pressure point (solid square). The second straight line, with a higher slope, starts at the open circle. There is a transition region between the two straight lines. From Fig. 4.9, it is found that the surface instability point or localized necking point is at $\varepsilon_V \cong 0.24$. The corresponding necking point in the pressure volume curve in Fig. 4.8 gives:

$$\eta = \frac{P_{\max} - P_{necking}}{P_{\max}} = 14\% \tag{4.22}$$

This implies that localized necking in the tube under internal pressure is assumed to occur when the pressure drops 14% from its maximum pressure. Subsequently, Eq. 4.22 will be used as the criterion for the onset of localized necking for tubes under internal pressure.

Fig. 4.10 shows the contour plots of the major principle strain at different deformation stages. It is observed that the deformation within the finite element model is quite inhomogeneous and the inhomogeneity starts when the volume strain is small. The inhomogeneous deformation gradually evolves with increasing volume strain and forms a localized neck at $\varepsilon_V \cong 0.24$. After localized necking, the applied deformation is almost all concentrated in the neck.

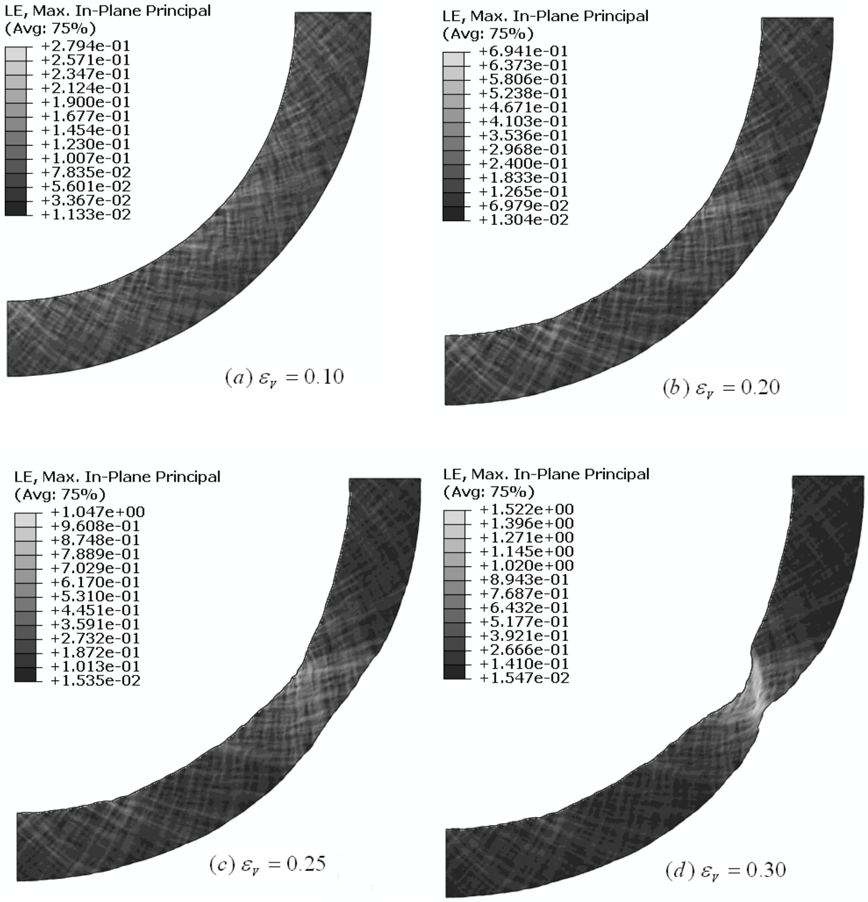

Figure 4.10 Predicted contours of the maximum principal strain at different deformation stages

The development of the localized neck is further demonstrated in Fig. 4.11, which shows the normalized tube thickness $H(\alpha)/H(0)$, for various stages of deformation. It is important to point out that necking is the natural outcome of the present analysis. More specifically, in the present finite element analysis localized necking is associated with a surface instability triggered by the severe surface roughening associated with the orientational difference between adjacent grains.

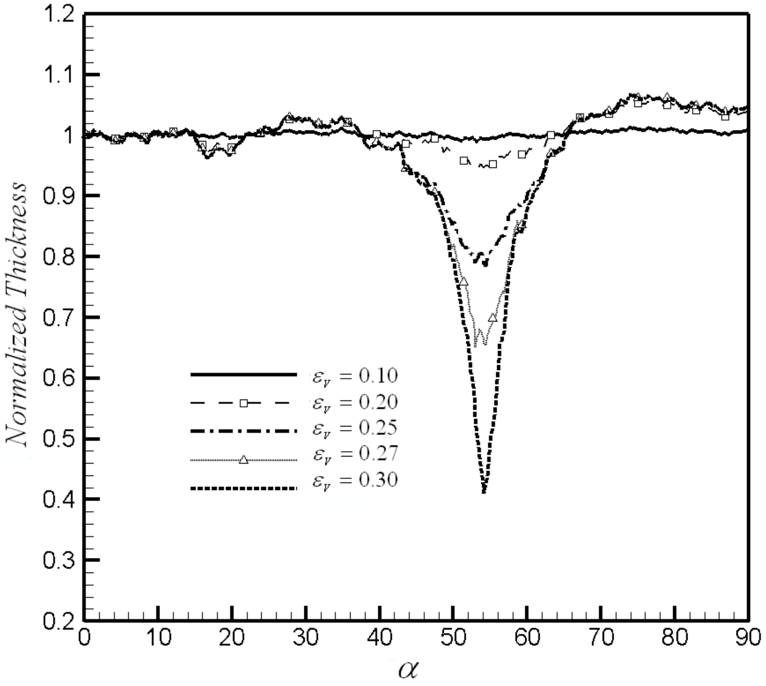

Figure 4.11 Predicted normalized thickness at different deformation stages

It has been generally recognized that predicting localization is usually sensitive to the mesh used. In the present study, however, the mesh sensitivity is equivalent to the dependency of deformation on the number of elements per orientation. Figs. 4.8-4.10 showed the numerical results based on a regular mesh with $N_{g_\alpha} \times N_{gR} = 3\times 2$. We have carried out a mesh sensitivity study using meshes with with $N_{g_\alpha} \times N_{gR} = 1\times 1$, 2×2, 3×3 and 6×4 in Fig. 4.12. Generally speaking, these numerical results indicate that while the onset of localized necking is not sensitive to the meshes applied, the predicted pattern of the grain-scale shear bands inside the localized neck is found to be dependent on the mesh employed. However, this mesh sensitivity is not very significant. The most significant difference between the meshes was that the predicted pressure, p, based on the mesh with only one element per grain (i.e. $N_{g_\alpha} \times N_{gR} = 1 \times 1$) is noticeably higher than the pressure predicted by the other meshes. It was noted that the aspect ratio of the elements in the meshes $N_{g_\alpha} \times N_{gR} = 3 \times 2$ and 6×4 is about 1, and these meshes favor the development of shear bands. Based on the mesh sensitivity study, and the experience with surface instability and localized necking in aluminum sheets under stretching (Wu et al., 2007), we expect the mesh with $N_{g_\alpha} \times N_{gR} = 3 \times 2$ to be able to capture the prominent features associated with shear banding and necking in the tube under an internal pressure, and this mesh will be used in the rest of the paper; however, it is believed that this mesh is too coarse to resolve grain-scale shear bands.

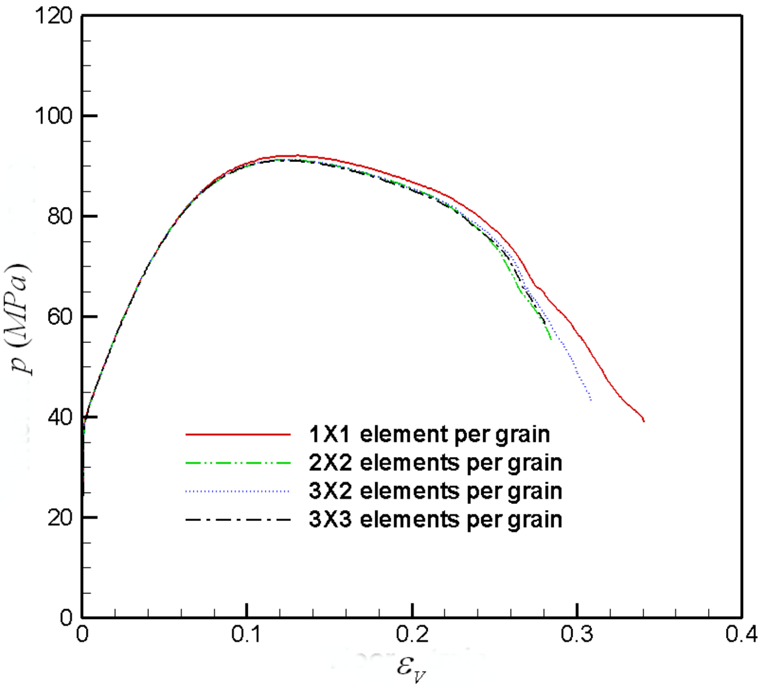

Figure 4.12 Effect of mesh density on pressure curves

Previous studies have indicated that localized necking in a sheet metal under stretching is usually sensitive to the material properties, such as work hardening and material strain rate sensitivity (e.g. Hutchinson and Neale, 1977; Wu et al., 1997; Inal et al., 2002a,b). Figs. 4.13 and 4.14 show the effect of the strain rate sensitivity on the predicted pressure, p , and minimum cross sectional area, A_{min}/A_0 , as functions of the volume strain, ε_V , respectively. It is found that increasing the rate sensitivity, m, from 0.007 to 0.020, increases the maximum pressure and decreases slightly the strain at which the pressure reaches its maximum. In Fig. 4.13, the open circles, indicating localized necking points, are identified according to Eq. 4.22, which states that localized necking in a tube under internal pressure occurs when the pressure drops 14% from its maximum pressure.

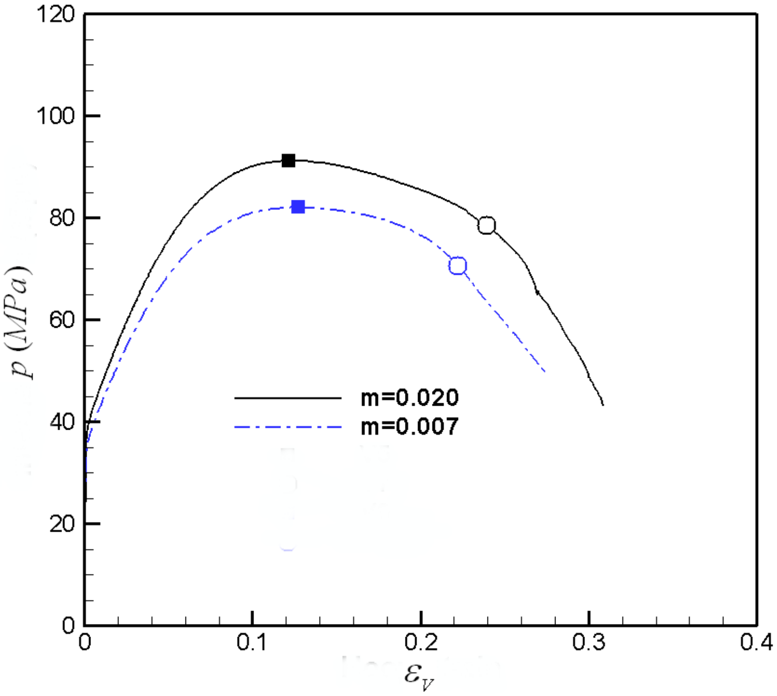

Figure 4.13 Effect of strain rate sensitivity *m* on the predicted pressure *p*

It is found, from Fig. 4.14, that the onset of localized necking is delayed by increasing the strain rate sensitivity. This delay was confirmed by observing differences in deformed meshes and/or distribution of strains between $m = 0.007$ and 0.020 at the same volume strains. These results are consistent with the findings reported by Inal et al. (2002a,b) and Wu et al. (2007). To study the strain hardening effect, we artificially increased the saturation value of the critical resolved shear stress τ_s by a factor of 2 from 112 MPa to 224 MPa. The effect of hardening on the predicted minimum cross-sectional area, A_{min}/A_0 , as a function of the volume strain ε_V is presented in Fig. 4.15. It is observed that localized necking is dramatically delayed by a significant increase in hardening.

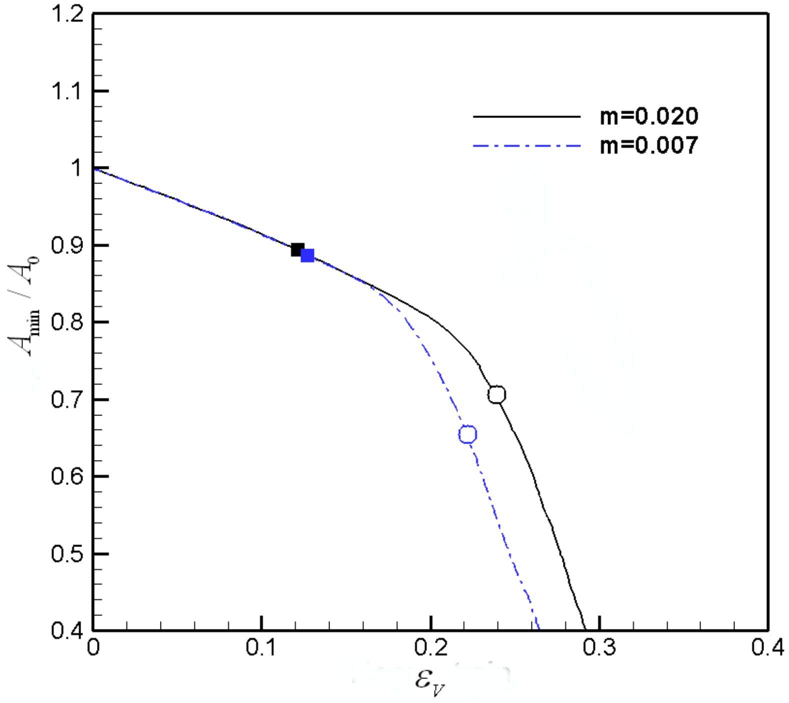

Figure 4.14 Effect of strain rate sensitivity *m* on the predicted minimum cross-sectional area A_{min}/A_0

Wu and Lloyd (2004) have demonstrated that while surface roughening is inevitable when a polycrystal undergoes plastic deformation, severe roughening is primarily due to the inhomogeneous distribution of grain orientations. Also, it has been found that since severe roughening is often a precursor to a surface instability associated with localized necking, localized necking in a sheet metal under stretching is sensitive to the spatial orientation distribution (Wu et al., 2007). It is thus expected that localized necking in a tube under internal pressure will also significantly depend on the spatial grain orientation distribution.

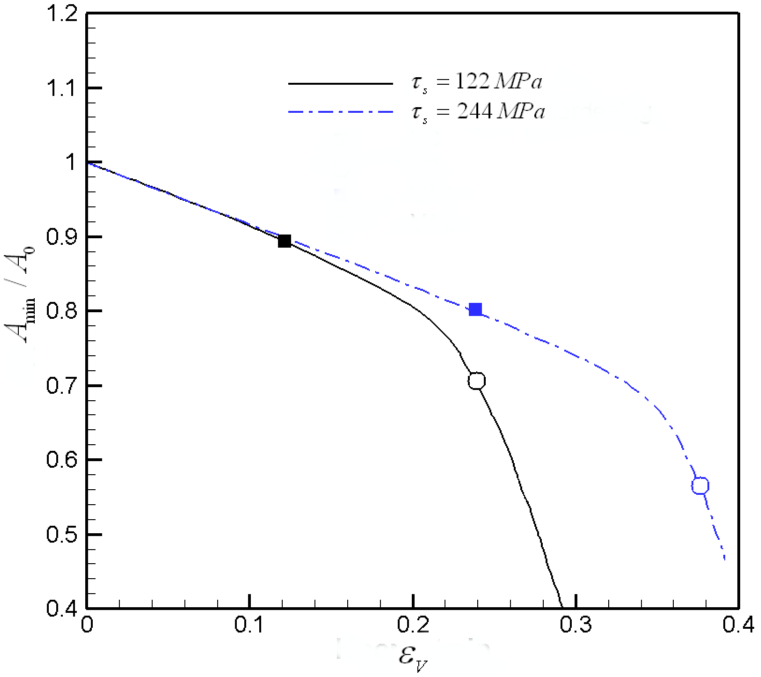

Figure 4.15 Effect of strain hardening on the predicted minimum cross-sectional area A_{min}/A_0

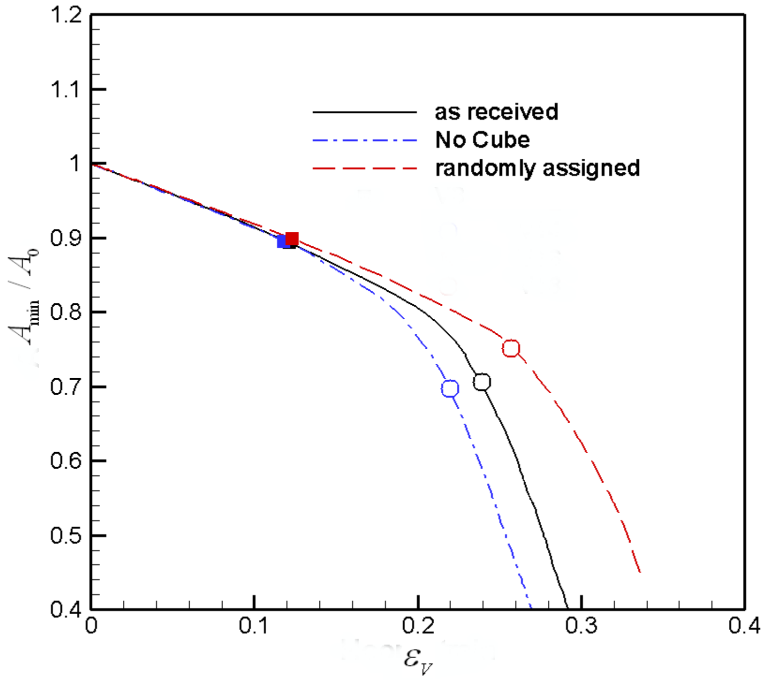

Figure 4.16 Effect of initial texture and its spatial distributions on the predicted minimum cross-sectional area A_{min}/A_0

To explore this aspect, two textural situations have been considered: (1) maintaining the same global texture as in the original sheet but distributing the grain orientations randomly through the mesh. This considers the influence of the spatial grain orientation distribution, and, (2) replacing the Cube oriented grains with random orientations. This case considers the role of the high volume fraction of Cube grains in the original sheet. Fig. 4.16 shows that the random distribution of the grain orientations delays the onset of instability, so the inhomogeneous spatial distribution of grain orientations in the original sheet is promoting instability. Fig. 4.16 also shows that removing the Cube orientated grains enhances the onset of necking. This is consistent with the forming limit diagram analyses by Wu et al. (2004) and Yoshida et al. (2007, 2009), and with the finite element simulation of the sheet under in-plane plane strain tension by Wu et al. (2007). It can be concluded that localized necking in a pressurized tube depends strongly on both the initial texture and its spatial orientation distribution.

In the present study, localized necking results from the evolution of surface roughness due to the spatial grain orientation distribution, and an artificial imperfection is not necessary to initiate necking. However, it is interesting to study the effects of initial surface topography on localized necking in a tube under internal pressure. Fig. 4.17 shows the initial surface topography for the outer surface of the tube. Note that this topography is mapped from the initial surface topography measured from the top surface of the sheet (see Fig. 4.3). The initial surface topography was not measured for the bottom surface of the sheet.

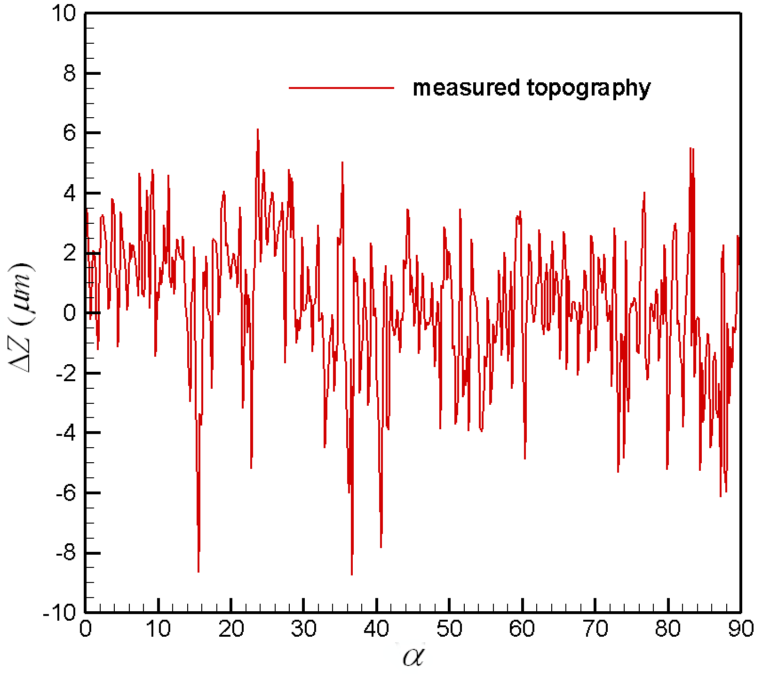

Figure 4.17 Measured initial surface topography

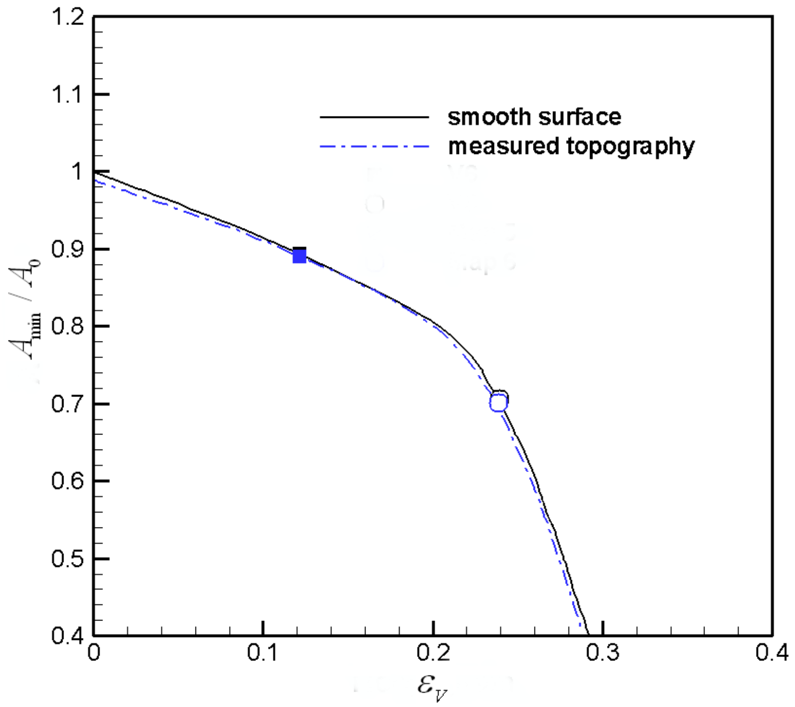

Figure 4.18 Effect of initial surface topography on the predicted minimum cross-sectional area A_{min}/A_0

In retrospect it seems advisable to have done so. In the following simulation we assume that the initial inner surface is perfectly smooth. The effect of the measured initial outer surface topography on the predicted minimum cross sectional area is presented in Fig. 4.18. It is found that the initial outer surface topography has almost no effect on the limit strain to necking. Fig. 4.19 shows the calculated surface profiles, defined in Eqn. 4.21, for the outer surface of the tube at different deformation stages. It is observed that when the deformation is very small, say $\varepsilon_V = 0.01$, the initial surface topography is still recognizable (Fig. 4.19a). At a strain $\varepsilon_V = 0.15$ the effect of initial surface topography on the deformed surface profile is dramatically reduced (Fig. 4.19b), and this effect is almost negligible when $\varepsilon_V = 0.3$ (Fig. 4.19c). Fig. 4.19 also shows that the initial surface topography does not change the location of localized necking. Based on this result, together with Fig. 4.17, it is clear that the initial surface topography has a negligible effect on the strain to necking, and that the initial texture and its spatial orientation distribution are the predominant factors for the development of localized necking. It should be emphasized that the main purpose of this paper is to develop a crystal plasticity based finite element model to predict localized necking in a tube under internal pressure. Although we defined that localized necking in a tube under internal pressure occurs when the pressure drops 14% from its maximum pressure, the overall conclusions are not solely dependent on this definition. The crystal plasticity based finite element model generates the profile of the normalized minimum cross-sectional area Amin/A_0 as a function of volume strain ε_V with different parameters, such as strain rate sensitivity, Fig. 4.14, or work hardening rate, Fig. 4.15, and an alternative necking criterion can be superimposed on these profiles.

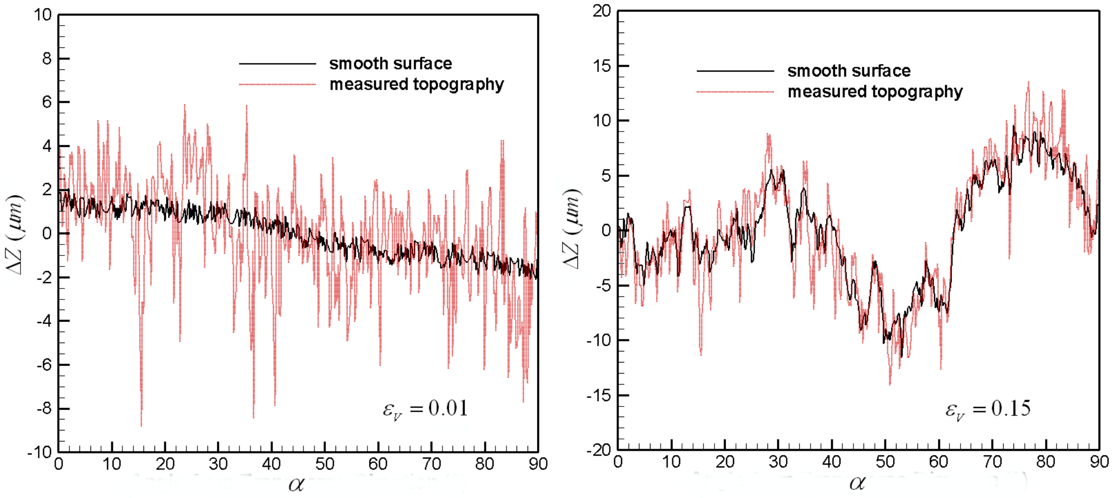

(a) **(b)**

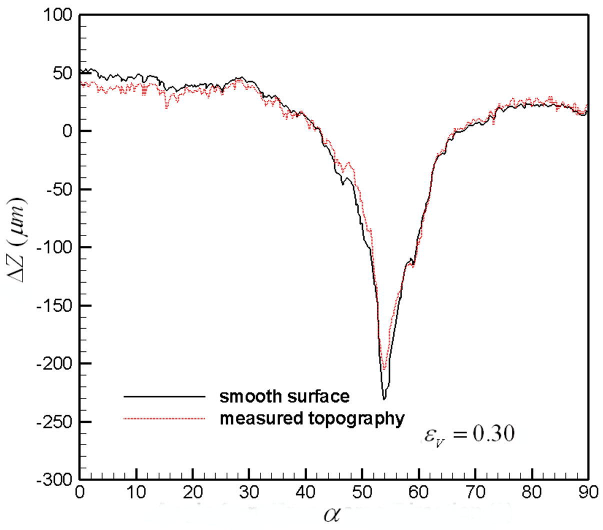

(c)

Figure 4.19 Effect of the measured initial surface topography on the calculated surface profile ΔZ at different deformation stages

4.2.3 Conclusions

A plane strain crystal plasticity based finite element model has been developed to simulate localized necking in an aluminum tube under internal pressure. The measured EBSD data for the sheet are mapped onto the tube and then directly incorporated into the finite element model and the constitutive response at an integration point is described by the single crystal plasticity theory.

Localized necking in tubes under internal pressure has been associated with the generation of a surface instability and the onset of unstable thinning. It has been demonstrated that such a surface instability/necking is the natural outcome of the present approach, and an artificial initial imperfection required by other approaches is not necessary in the present analysis. The effects of spatial orientation distribution, strain rate sensitivity, work hardening, and initial surface topography on necking have been discussed. It has been demonstrated that while the initial surface topography has only a small influence on necking, localized necking depends strongly on both the initial texture and its spatial orientation distribution.

This research work has been published in 2010 (Shi et al. (2010)).

Chapter 5

Surface Roughening Analysis in Aluminum Tube Hydroforming

Crystal plasticity based FEM has been used to investigate the role of grain orientation on the development of surface topography during straining (Wu and Lloyd 2004, and Wu et al. 2003a). These studies were based on the assumption that surface roughening is mainly due to the inhomogeneous deformation between surfaces or near surface grains with little contribution from interior grains through interaction between the surface and supporting layers. Although surface roughening considers a relatively small length scale, a FE analysis with a sampling area or EBSD map similar to that used by Wu et al. (2003a & 2003b) could significantly underestimate or overestimate surface roughening due to the idealization of the boundary condition specifications. Very recently, Wu and Lloyd (2004) have developed the FEM based on crystal plasticity and directly incorporate EBSD measured through the entire thickness. In the current work, we apply a similar approach to investigate the effect on surface roughening by the initial texture during hydroforming. Based on a very large-scale EBSD map, effects of imposed deformation path, strain work hardening, strain rate sensitivity and initial texture and its spatial distribution on surface roughening and development of roughness have been discussed.

5.1 Problem formulation

The same single crystal plasticity constitutive model used in Chapter 4 has been adopted in the study of surface roughening analysis. We consider a rolled sheet with the rolling direction by RD, the transverse direction TD and the normal direction ND. EBSD is performed on a small region in the ND-TD section (N.T. section), as illustrated in Fig. 4.1. An orientation in the EBSD map thus represented a grain. The model region (marked in Fig. 4.1a), with the initial length L_0 along the TD and the initial thickness H_0 in the ND, is mapped into one quadrant of a tube with the inner radius $R_I = \frac{2L_0}{\pi} - H_0$ and thickness H_0 (Fig. 4.1). During this mapping, the orientation of a grain is rotated α degrees around the RD according to the initial position of the grain in the marked region and the corresponding position in the tube. For consideration of plane strain deformation, we define the surface roughness (Fig. 5.1) as:

$$R_a = \frac{1}{N}\sum_{1}^{N} |\, \Delta Z \,| \tag{5.1}$$

Z and H_t are respectively the radius of the outer surface at α and the averaged (mean) outer radius. The detailed problem setup can be found in the section 4.2.

5.2 Results and discussions

A commercial AA6111-T4 at a gauge of about 0.9 mm is modelled with an average grain size of the order of 30 μm along the TD and 20 μm in ND. The initial texture is directly generated from the measured EBSD data, which was performed on a region about 5.89 mm by 0.89 mm in the N.T. section of the sheet. It is noted that the sheet has an extremely high Cube texture. The same values used in the last section are selected for the material parameters in the crystal plasticity analysis (See Table 4.2). Similarly, it should be emphasized, that the main purpose of this work is to develop a crystal plasticity based finite element model to predict surface roughening and its development during hydroforming, and the overall conclusions are not particularly dependent on the values of the material parameters.

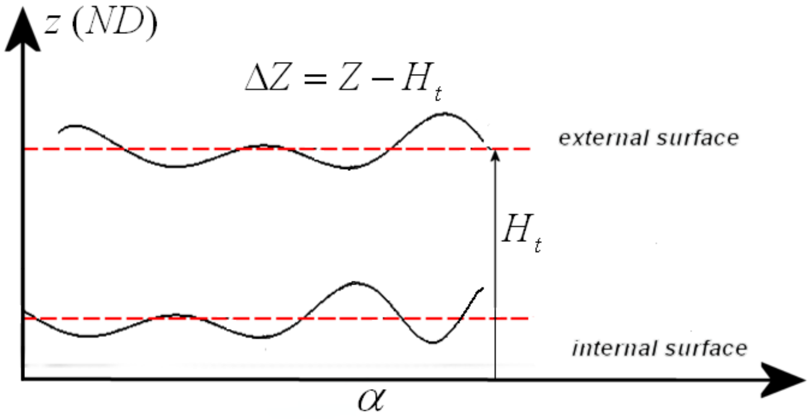

Figure 5.1 Surface roughness definition

Fig. 5.2 shows the outer surface profile evolution at different volume stain levels. As the volume strain increases, the surface profiles tend to become rougher. While surface roughening is inevitable when polycrystal undergoes plastic flow, severe roughening is believed to be primarily due to the inhomogeneous distribution of grain orientations. With the numerical procedures established, the effect of spatial distribution of grain orientations on the topographical development can be studied.

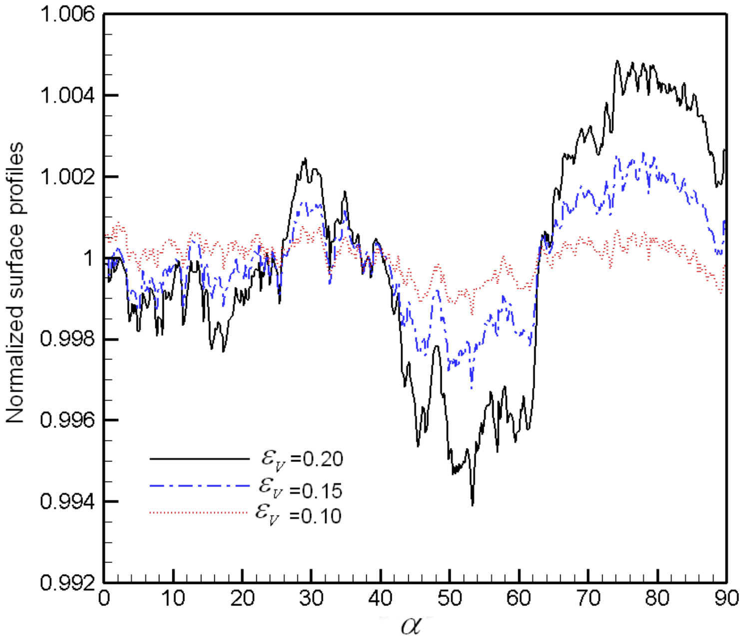

Figure 5.2 External surface profiles

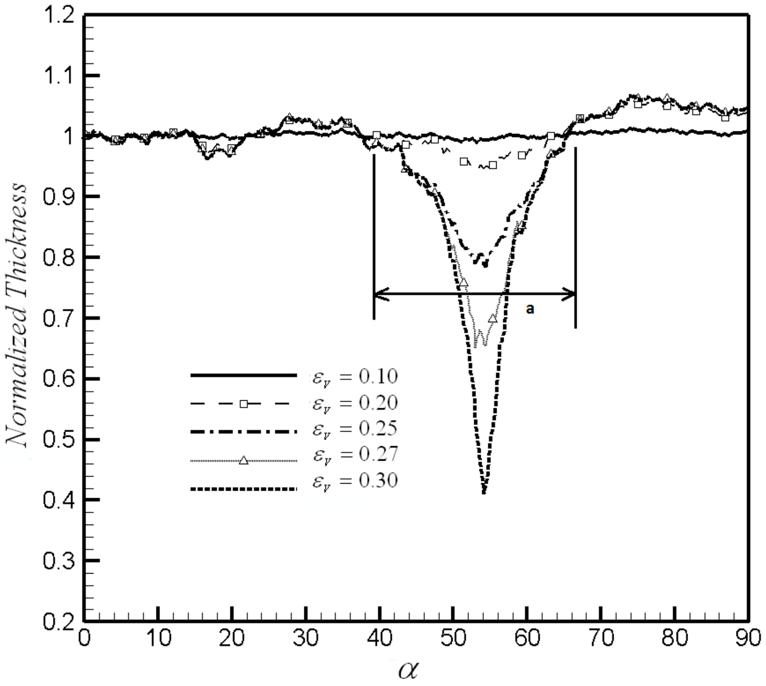

Figure 5.3 Predicted normalized thickness at different deformation stages

As discussed in the previous section, there is a bi-linear relationship between the minimum cross-sectional area and the volume strain in Fig. 4.8 and 4.9. We define the maximum pressure point (solid square) as the onset of diffused necking and the surface instability point or localized necking point (open circle) is at $\varepsilon_V \cong 0.24$ when pressure reaches 14% peak pressure. Obviously, the surface roughening and its development in which we are interested should be in the range over which the volume strain is less than localized necking point. But for a good comparison, we plot the corresponding diffused necking point and localized necking point on the surface roughening plot as well. Wu et al. (2007) have demonstrated that while surface roughening is inevitable when a polycrystal undergoes plastic deformation, severe roughening is primarily due to the inhomogeneous distributions of grain orientations under applied strain. Fig. 5.3 shows the calculated tube thickness $H(\alpha)$, normalized by $H(0)$ i.e. the tube thickness at $\alpha = 0$ (see Fig. 5.1), at various deformation stages. General observation is that the change of normalized thickness has been developed significantly when volume strain ε_V reaches a value of 0.2. The change of normalized thickness can be interpreted as the evolution of the surface roughening under an internal pressure. As the strain level exceeds 0.2, most of the strain development concentrates in this necking zone, which we define as “a” zone. There is little change in terms of thickness outside of this “a” zone. This implies that surface roughening may stop developing outside of the necking region after localized necking occurs.

The predicted mean surface roughness, R_a, based on the Eq. 5.1 is studied and plotted in Fig. 5.4. The surface roughness is calculated by extracting the external surface profile at the different strain levels. We use the MountainsMap™ software to calculate R_a to: 1) filter out the long wave profile (tube circular shape) and 2) subtract the localized necking region, "a" zone from R_a calculation. In Fig. 5.4, both filtered R_a and unfiltered R_a are plotted. It has been found that mean surface roughness has increased almost linearly when strain ε_V is less than 0.22. After passing this strain level (solid diamond), the mean surface roughness R_a stops increasing with respect to the increase of volume strain ε_V and enters a plateau region.

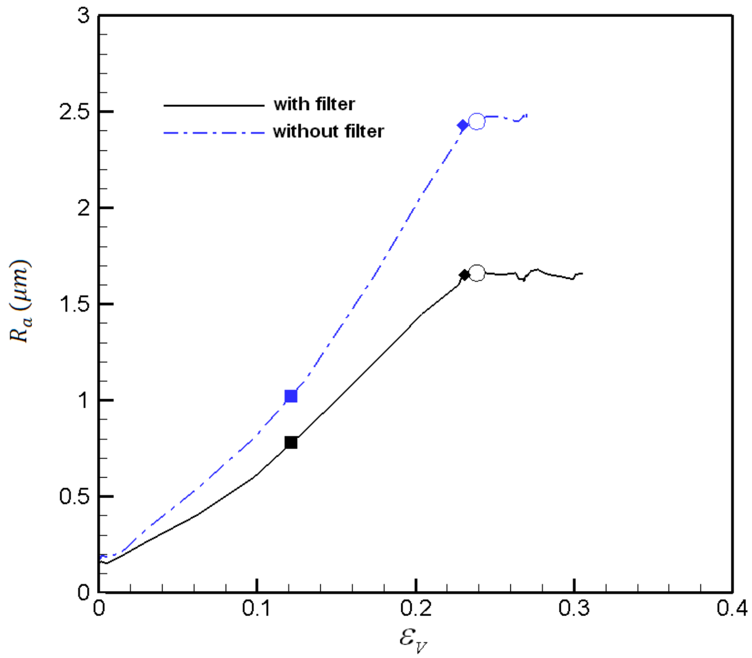

Figure 5.4 Predicted R_a as a function of volume strain ε_V
Localized necking definition: approach A: open circle, approach B: solid diamond

This result confirms that development of the mean surface roughness R_a is influenced by the localized necking strain. After the localized necking occurs, the deformation of the tube concentrates in the necking region, the "a" zone, and the mean surface roughness R_a excluding the "a" zone remains unchanged. It is also found that the starting point of the surface roughness R_a plateau (solid diamond) almost matches the localized necking point (hollow circle) as defined earlier. This confirms the previous localized necking definition to be valid (approach A: the pressure approach). Meanwhile, this finding also provides another indicator to define the onset of tube localized necking during pressurization; which is that localized necking starts when mean surface roughness R_a stops increasing (approach B: the R_a approach). The starting point of the surface roughening plateau is not affected by the filter as shown in Fig. 5.4. It may be useful to point out that the initial roughness at $\varepsilon_V = 0.0$ in Fig. 5.4, is caused by the mesh configuration because we use line segments (CPE4 elements) to represent the smooth round tube circle. This artificial initial roughness can be minimized by increasing the mesh density (467 elements along the arc length are used in this case), but cannot be avoided where line segments are used.

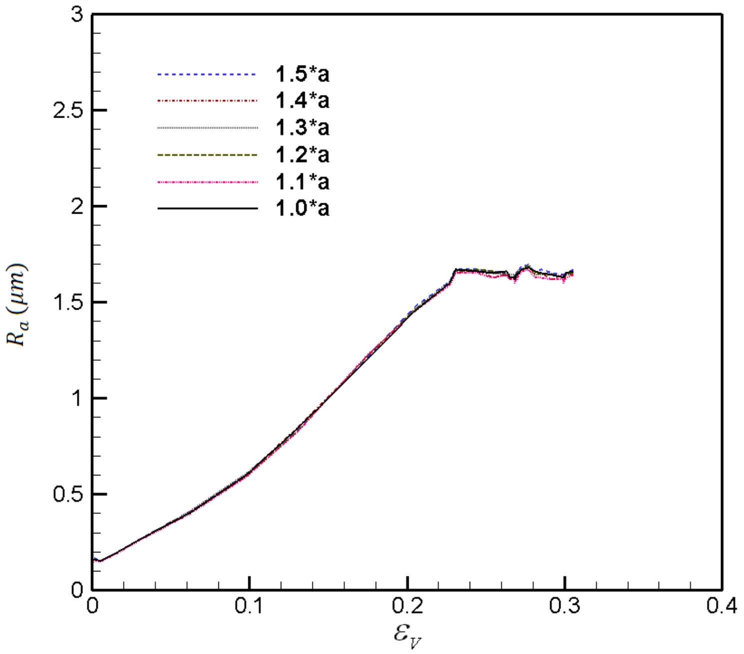

Figure 5.5 Effect of length “a” on the predicted R_a

In order to study the sensitivity of the “a” zone on the mean surface roughness R_a, we increased the original window length “a”, which was already wide enough to cover the necking region, up to 1.5 “a” length incrementally. From Fig. 5.5, it is clear that the length of window “a” has little influence on the surface roughness R_a at all strain levels as long as the “a” zone is wide enough to encompass the necking zone. The length of window “a” has no influence on the starting point of surface roughness plateau as well. It is important to point out that this surface roughening prediction under pressurization is the natural outcome of the present analysis. In the present finite element analysis, surface roughening is associated with the crystallographic orientational difference between adjacent grains under plastic deformation.

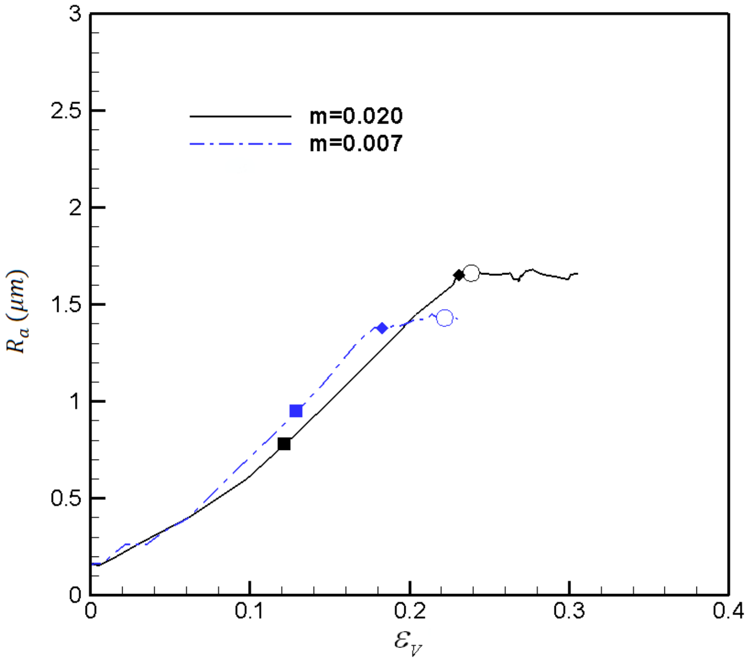

Figure 5.6 Effect of strain rate sensitivity *m* on the predicted R_a

Previous studies have indicated that localized necking in sheet metal under stretching and hydroforming is usually sensitive to the effects of materials properties such as strain hardening and material strain rate sensitivity (e.g. Wu et al. (2006) and Shi et al. (2010)). Fig. 5.6 and 5.7 show the effect of the strain rate sensitivity on the predicted surface roughness R_a and pressure p as functions of the volume strain ε_V, respectively. It is found that an increase of the rate sensitivity *m* (from 0.007 to 0.020) will increase both maximum pressure (solid square) and surface roughness. This is because an increase of the rate sensitivity increases the amount of work hardening at a high strain level, and results in further surface roughening as plastic strain increases. In general, the onset of localized necking has been retarded by increasing the strain rate sensitivity.

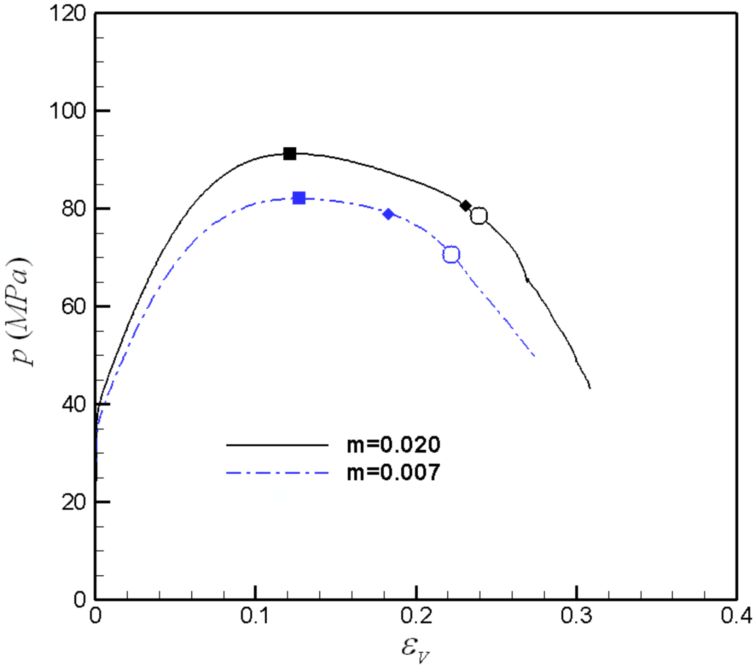

Figure 5.7 Effect of strain rate sensitivity *m* on the predicted internal pressure *p*

In terms of finding the onset of localized necking point, some difference exists between approach A (the pressure approach, open circle) and approach B (the R_a approach, solid diamond). Approach B predicts lower localized necking strain than approach A does. By examining the surface roughness R_a plot (Fig. 5.6), the pressure p plot (Fig. 5.7) and the minimum cross sectional area A_{min}/A_0 plot (Fig. 5.8), it seems that approach A may slightly over-predict the localized necking strain. In a minimum cross sectional area plot (Fig. 5.8), the solid diamond (approach B) is closer to the start of the second line than the open circle (approach A). In other words, approach B (the R_a approach) may give more consistent results than approach A (the pressure approach) in this case study.

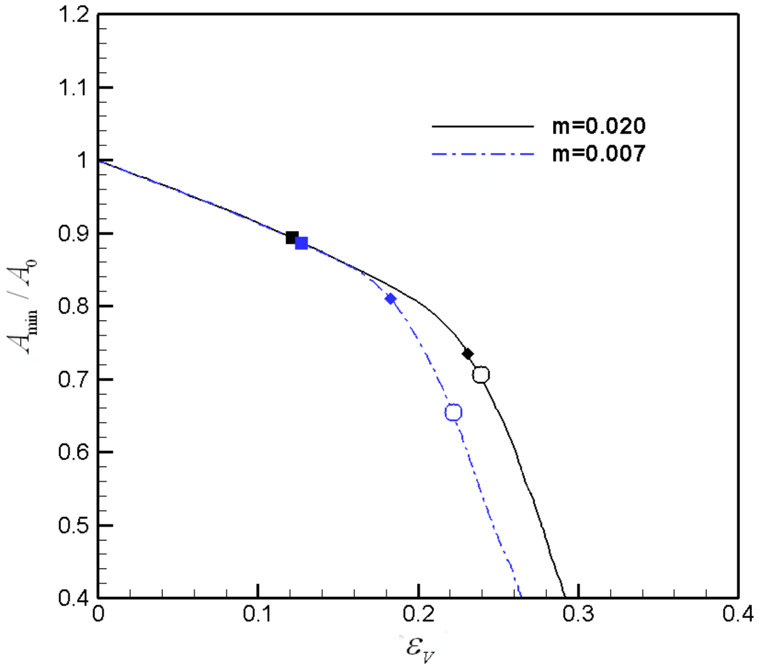

Figure 5.8 Effect of strain hardening on the predicted minimum cross-sectional area A_{min}/A_0

To study the effect of strain hardening, we artificially increase the saturation value of the critical resolved shear stress τ_s by a factor of 2 from 112 MPa to 224 MPa. The effect of changing of hardening on the predicted surface roughness R_a as a function of the volume strain ε_V is presented in Fig. 5.9. It is observed that localized necking and surface roughening (both approach A and B) are significantly delayed by the increase in hardening. There is no significant difference in predicting the localized necking strain in either approach.

Wu (2007) has demonstrated that while surface roughening is inevitable when a polycrystal undergoes plastic deformation, severe roughening is primarily due to the inhomogeneous distribution of grain orientations. It has been also found that severe surface roughening is often a precursor to surface instability, which is very sensitive to the spatial crystallographic orientation distribution. In other words, surface roughening will significantly depend on the spatial orientation distribution. Fig. 5.10 shows the effect of initial crystallographic texture and its spatial orientation distributions on the predicted mean surface roughness R_a. In Fig. 5.10, a case in which the measured orientations are randomly assigned to the elements in the mesh is studied. Since the sheet has a very high Cube texture component, the effect of Cube on surface roughening is investigated by studying the situation where the Cube orientated grains are replaced by random orientations.

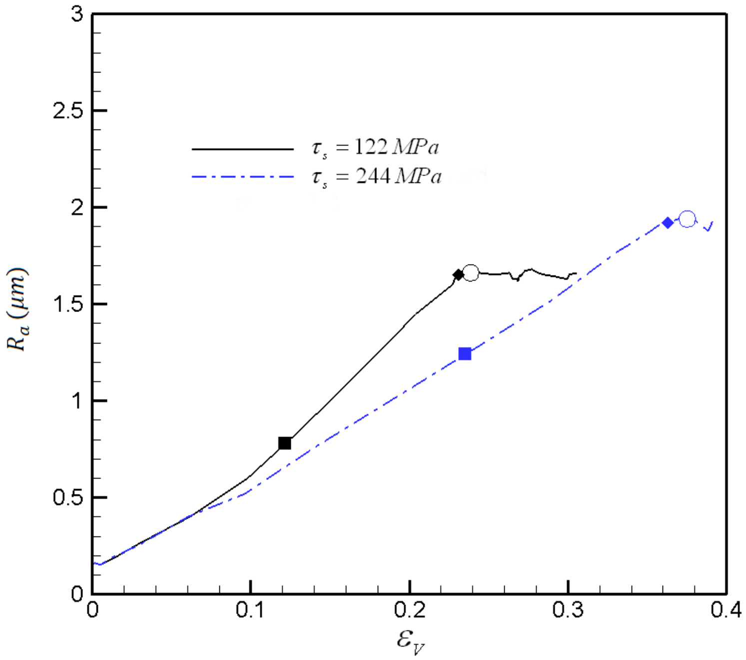

Figure 5.9 Effect of work hardening on the predicted R_a

From Fig. 5.10, it is revealed that the case where orientation is globally randomly assigned has a lower R_a value than that given by as received tube at the same strain level. This observation indicates that there is a very strong inhomogeneity in the spatial distribution of grain orientations. This inhomogenity in the spatial distribution influences tube surface roughness when the tube is under internal pressure loading, even though the grain orientation in both cases generates the same pole figure.

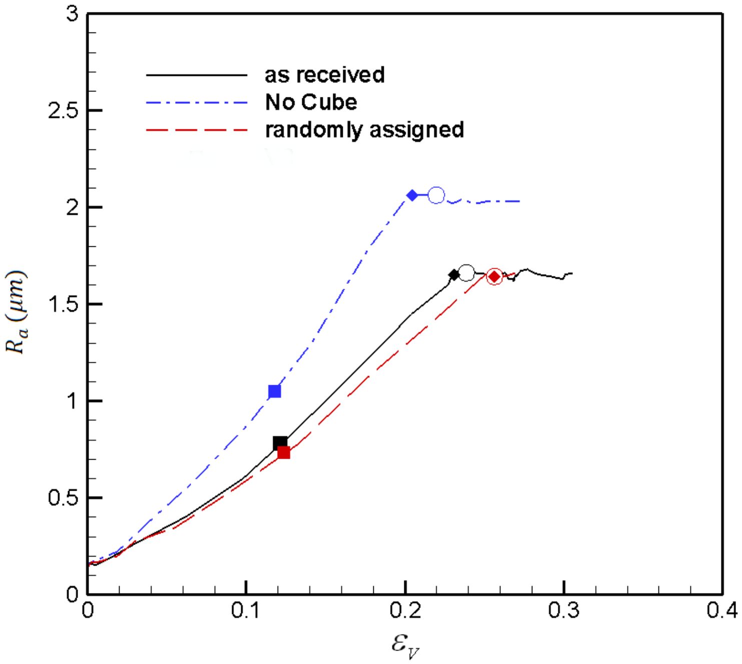

Figure 5.10 Effect of initial texture and its spatial distributions on the predicted R_a

Through comparing the case in which Cube textures have been artificially replaced with random orientations, it is found that the latter has a very high surface roughness under the same strain levels. It is clear that the initiation of localized necking in the case with orientations being globally randomly assigned is significantly delayed compared to the necking strain in the as-received tube. The necking strain in the tube with no Cube case has been drastically reduced. It can be concluded that both surface roughening and localized necking in a pressurized tube depends strongly on both the initial crystallographic texture and its spatial orientation distribution. In this case study, we also found both approach A and approach B give very similar results in defining the localized necking points.

The other case studied is the influence of initial surface roughness on the deformed tube surface roughening. Previous work (Shi et al. (2010)) has shown that initial roughness has little influence on the localized necking for a tube under internal pressurization. This is due to the fact that localized necking results from inhomogeneous deformation due to the spatial grain orientation distribution. Under the larger strain level, the initial surface topography on the deformed surface profile is dramatically reduced, and its effect on necking is almost negligible.

Fig. 4.17 shows the initial surface topography for the external surface of the sheet, which has been mapped to the external surface of the tube, with an initial surface roughness R_a of 1.1 um. The effect of the measured initial surface topography on the predicted mean surface roughness R_a at various strain levels is presented in Fig. 5.11. It is found that the initial surface topography has a major influence on mean surface roughness R_a evolution. Starting with an R_a of around 1.3 um (almost 0.2 um is introduced by the mesh configuration), the surface roughness with measured surface topography slowly increases with an increase of strain. Its slope is gentler than that of the smooth surface case when the strain is below 0.12. However, both cases reach almost the same localized necking strain ($\varepsilon_V = 0.22$), which affirms the previous finding that the initial surface topography has little influence on necking. However, the initial surfaces roughness plays a significant role in determining the mean surface roughness on a deformed tube. The higher the initial R_a, the higher the R_a on deformed tube. This result agrees well with some industrial hydroforming application such as the PRF forming process (Mallory & Shi (2011)), where an ironing operation has been added to preforms before hydroforming to improve the surface quality of final products. Also, the localized necking strains predicted by using approach A and approach B are very similar.

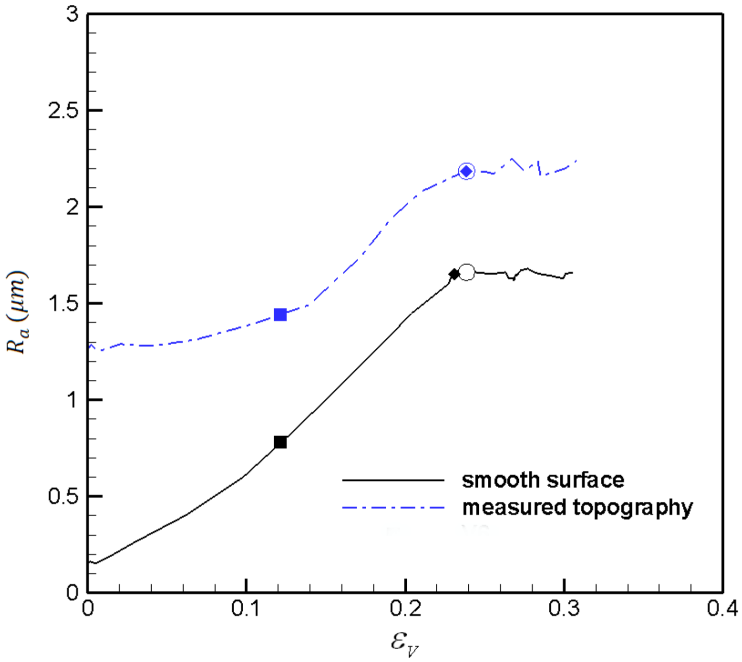

Figure 5.11 Effect of initial surface topography on the predicted R_a

5.3 Conclusions

A plane strain crystal plasticity based finite element model has been developed to simulate tube surface roughening in hydroforming. The measured EBSD data for the sheet are mapped to the tube and then directly incorporated into the finite element model and the constitutive response at an integration point is described by the single crystal plasticity theory.

Surface roughening in tubes in hydroforming has been associated with the crystallographic orientational difference between adjacent grains under plastic deformation. The effects of spatial orientation distribution, strain rate sensitivity, work hardening, and initial surface topography upon the onset of the localized necking and surface roughening have been discussed. It has been found that surface roughening depends strongly on the initial texture, the spatial orientation distribution and the initial surface topography. It has also been found that the starting point of mean surface roughness R_a plateau during tube plastic deformation could be used as another indicator to define the onset of localized necking.

This research work has been published in 2012 (Shi et al. (2012)).

Chapter 6

Effect of Rate Sensitivity on Necking Behavior of Tube under Dynamic Loading

In this section, a numerical study of the effect of rate sensitivity in material on necking behavior, especially in dynamic loading conditions, is considered. The dynamic fracture demonstrates a very different deformation response in terms of limiting necking retardation and deformation modes. We will also investigate rate sensitivity on laminated material in the second part of this analysis, as it is well known that laminated systems can take advantage of various material properties in a single product and have wide applications in the industry.

6.1 Constitutive model

An elastic-viscoplastic model has been chosen for this study. In this section we very briefly review the constitutive framework adopted. For details we refer to Pierce et al. (1984) and Weber and Anand (1990). In the elastic-viscoplastic model employed, the constitutive equations are a generalization of the classical J_2 flow theory to model finite elastic and plastic deformations and rate-dependence of plastic flow. The constitutive equation for elastic response is:

$$\dot{\mathbf{S}} = 2\mathbf{G}\dot{\mathbf{E}}^{\mathbf{e}} \tag{6.1}$$

where $\dot{\mathbf{S}}$ is deviatoric stress rate, $\dot{\mathbf{E}}^{\mathbf{e}}$ is deviatoric elastic strain rate and $\mathbf{G}$ is shear modulus. The flow rule is taken as:

$$\dot{\varepsilon}^{p} = \dot{\gamma}\frac{\mathbf{S}}{\|\mathbf{S}\|} \tag{6.2}$$

Effective stress and effective strain measures are:

$$\bar{\sigma} = \sqrt{\frac{3}{2}S_{ij}S_{ij}}\ ,\ \dot{\bar{\varepsilon}} = \sqrt{\frac{2}{3}\dot{\varepsilon}_{ij}^{p}\dot{\varepsilon}_{ij}^{p}} \tag{6.3}$$

respectively, where $\dot{\gamma}$ is the plastic parameter and $\dot{\varepsilon}_{ij}^{p}$ is the effective plastic strain rate. For the elastic-viscoplastic material model, the strain rate relation by Pierce et al. (1984) can be written as:

$$\dot{\bar{\varepsilon}} = \dot{\varepsilon}_0\left[\frac{\bar{\sigma}}{s}\right]^{1/m} \tag{6.4}$$

where $\dot{\varepsilon}_0$ is the initial strain rate and m is the rate sensitivity constant, and s is the saturation stress. The evolution of saturation stress rate $\dot{s}$ in terms of strain rate change is given by Weber and Anand (1990):

$$\dot{s} = g = h\dot{\bar{\varepsilon}} \tag{6.5}$$

$$h = h_0\left|1-\frac{s}{s_a}\right|^{\alpha}\ ,\ s_a = s^{*}\left(\frac{\dot{\bar{\varepsilon}}}{\dot{\varepsilon}_0}\right)^{n} \tag{6.6}$$

where h_0 , α , s^{*} and n are the material parameters for the viscoplastic material. The integration procedure for elastic-viscoplastic constitutive equations can be completed as follows. Firstly, the current configuration of a body is defined as the configuration at time t, which is indicated by the subscripts 'n' on variables. The current state (σ_n, s_n) is assumed to be known. The objective is to determine the next state (σ_{n+1}, s_{n+1}) by the integration of constitutive equations. Using the backward Euler method of integration as discussed in Chapter 2, the solution of Eq. (6.1) and (6.5) can be written as:

$$\mathbf{S}_{n+1}^{T} = \mathbf{S}_{n} + 2\mu\Delta t\dot{\boldsymbol{\varepsilon}}_{n+1} \tag{6.7a}$$

$$\bar{\sigma}_{n+1} - \bar{\sigma}_{n+1}^{*} + 3\mu\Delta t\dot{\bar{\varepsilon}}_{n+1} = 0 \tag{6.7b}$$

$$\bar{s}_{n+1} - \bar{s}_{n} - \Delta t g = 0 \tag{6.8}$$

where $\mathbf{S}^{T}$ is a trial stress and μ is the elastic shear module. Newton-Raphson iteration can be used to solve the nonlinear equation system (Eq. 6.7-6.8) and is normally quadratically convergent. Upon converging, the Cauchy stress $\boldsymbol{\sigma}$ can be updated through:

$$\boldsymbol{\sigma}_{\mathbf{n}+\mathbf{1}} = \frac{\left\|\mathbf{S}_{\mathbf{n}+\mathbf{1}}\right\|}{\left\|\mathbf{S}_{\mathbf{n}+\mathbf{1}}^{\mathbf{T}}\right\|}\mathbf{S}_{\mathbf{n}+\mathbf{1}}^{\mathbf{T}} + p\mathbf{1} \tag{6.9}$$

where p is hydrostatic pressure. $\mathbf{1}$ is a second identity tensor.

The elastic-viscoplastic model and time integration procedure have been implemented in an explicit finite element code ABAQUS (2006) through a user routine VUMAT.

The transient analyses are carried out by using a finite element approximation of the displacement components u_i in the dynamic principle of virtual work. The resulting equation of motion takes the form:

$$\mathbf{M}\ddot{\mathbf{U}} = \mathbf{P} \tag{6.10}$$

where $\mathbf{M}$ is mass matrix, $\mathbf{U}$ is the nodal displacement vector and $\mathbf{P}$ is the nodal force.

In the explicit time integration procedure, the maximum stable time step is limited by the criterion $\Delta t < \min(L_e / c_d)$, where L_e is characteristic element dimension, c_d is the current effective dilatational wave speed of the material, which is defined as $c_d = \sqrt{(\bar{\lambda} + 2\bar{\mu}/\rho}$ in ABAQUS/Explicit, $\bar{\lambda}$ and $\bar{\mu}$ are the effective Lamé constants and ρ is the density of the material. The minimization is taken over all the elements.

6.2 Problem formulation and method of solution

In studying the deformation behavior of tube expansion, a quarter cross section of a circular tube is considered. Following Shi et al. (2010), we assume that the quadrant of tube is long enough to contain several necks and no deformation is allowed in the axial direction, thus the tube is deformed in plane strain. The overall response of the tube under expansion is represented by the nominal hoop traction (T / σ_0) normalized by yield stress σ_0 and the normalized minimum cross sectional area $(A_{\min} / A_0)$ as a function of nominal hoop strain $\Delta R / R_0$. Here, A_0 and R_0 are the initial cross-sectional area and initial inner mean radius of the tube as shown in Fig. 6.1, respectively. ΔR is the change of tube radii after expansion.

For the plane strain deformation considered, we have

$$A_{\min} / A_0 = H_{\min} / H_0 \tag{6.11}$$

where $H_{\min}$ is the minimum thickness and H_0 is the initial thickness as shown in Fig. 6.2. To assess the effect of an initial surface imperfection on necking, an idealized initial outer surface topography will be implemented into the finite element model through $H_0 = H_0 + \Delta h_0$. Here, H_0 is the initial mean thickness of the tube and Δh_0 is the initial imperfection, which is applied only to the outer surface of the tube. The initial imperfection is taken to be the form:

$$\Delta h_0 = H_0 \delta \cos \frac{2\pi N_y R_0 \gamma}{L_0} \tag{6.12}$$

Here, N_y is the wave number and $H_0\delta$ is the imperfection amplitude, and L_0 is the initial quadrant length of the outer surface.

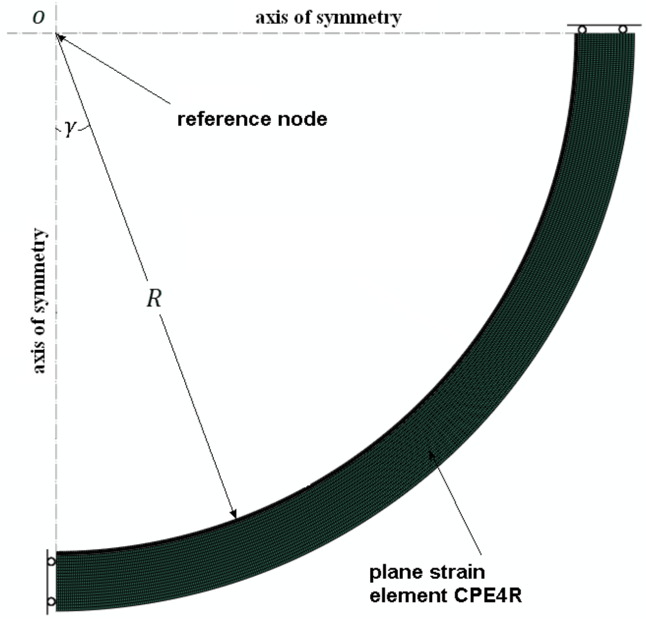

Figure 6.1 Schematic representations of one quadrant of a tube in dynamic expansion

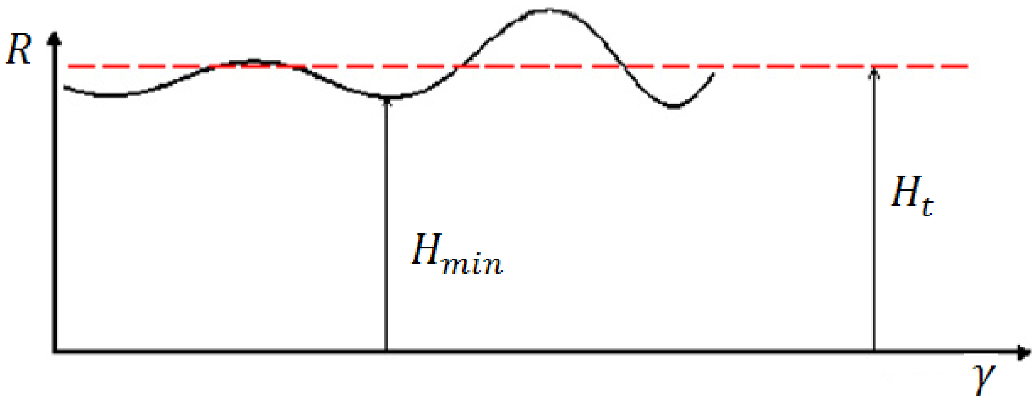

Figure 6.2. Schematic representations of outer surface topographies of a tube in deformed state.

The boundary conditions, which express the zero traction on both internal and external surfaces, are described by the quadrant of the tube with $\alpha = 0^o$ and 90^o as symmetric planes. Here, we take the body forces specified by Han and Tvergaard (1995), which represents the radial velocity history of a ring specimen reported by Madsen (1970) as:

$$\begin{cases} f^a = F_{\max} \sin\left(\frac{\pi t}{t_0}\right)\frac{X^a}{R} = F_{\max}\sin(\pi t \dot{\varepsilon}_0)\frac{X^a}{R}, a = 1,2 \\ f^3 = 0 \end{cases} \tag{6.13}$$

where X^a are the current Catesian coordinates, R is the current distance from the center, t_0 is the length of the time interval in which the non-vanishing body force is applied to the tube and t_0 can be associated with starting strain rate $\dot{\varepsilon}_0$ as $\dot{\varepsilon}_0 = 1/t_0$. $F_{\max}$ is the maximum value of the body force applied. The desired loading speed can be achieved through adjusting the values of $F_{\max}$ and $\dot{\varepsilon}_0$. This body force loading condition is applied via a user subroutine VDLOAD in ABAQUS/Explicit.

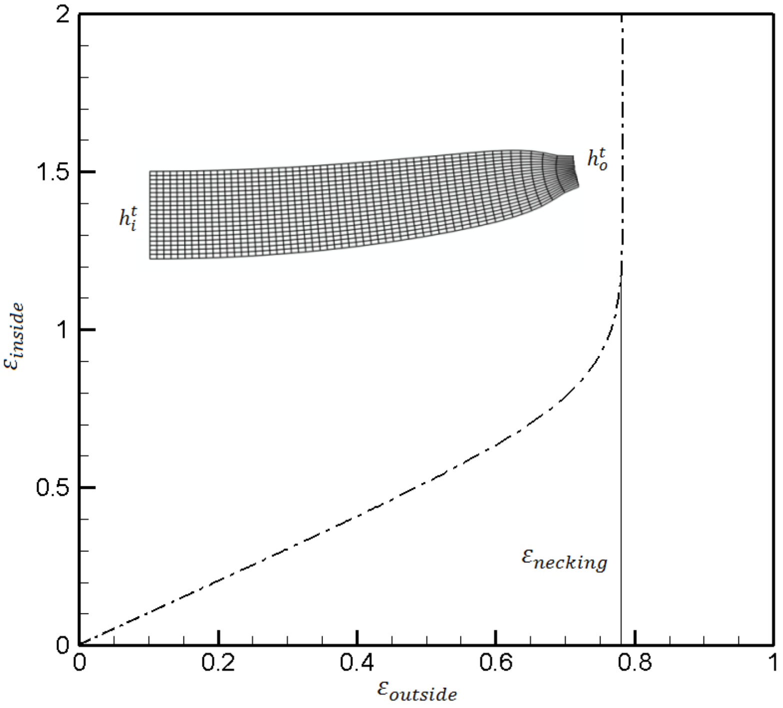

Figure 6.3 Definition of localized necking strain

The localized necking strain can be determined by examining the deformed tube configuration during loading as shown in Fig. 6.3. The height of the thinnest cross-section h_i^t and the height of the thickest cross-section h_o^t will be used to obtain the average major strains at two places, respectively:

$$\varepsilon_{inside} = -\ln \frac{h_i^i}{h_i}\,,\ \varepsilon_{outside} = -\ln \frac{h_o^i}{h_o} \qquad (6.14)$$

where h_i is the initial cross-section height of the imperfect side and h_o is the initial cross-section height of the perfect side and, ε_{inside} and $\varepsilon_{outside}$ are the strains corresponding to the imperfect and perfect sides as denoted by Hutchinson and Neale

(1977). Localization will happen at the imperfect side (thinnest cross-section) and the localized necking strain $\varepsilon_{necking}$ is the strain at the perfect side ($\varepsilon_{outside}$) that satisfies the following expression, as shown in Fig. 6.3:

$$\frac{d\varepsilon_{outside}}{d\varepsilon_{inside}} = 0 \tag{6.15}$$

6.3 Results and discussions

6.3.1 Monolithic material

The bench material employed in this elastic-viscoplastic material model is an aluminum alloy AA6111. The values for the material parameters are taken as:

Table 6.1 Values of material parameters for AA6111

Parameter	Unit	AA6111	Parameter	Unit	AA6111
E	GPa	63.2	s^*	MPa	737
μ		0.33	h_0	MPa	6270
σ_0	MPa	176	τ_s	MPa	122.4
α		3.58	$\dot{\varepsilon}_0$	s^{-1}	0.001
m		0.0005	n		0.0

It is noted that these material constants represent a rate independent material. The selection of a very small rate sensitivity value (m =0.0005) is to avoid a singularity during plastic calculation. In order to study the influence of the strain rate sensitivity m on the necking in dynamic loading, we artificially increase the m value up to 0.1. It should be emphasized, however, that the main purpose of this paper is to develop an elastic-viscoplastic based finite element model to study the effect of rate sensitivity and strain rate on localized necking during tube expansion under rapid dynamic loading and the overall conclusions are not particularly dependent on the values of the material parameters selected. The effects of rate sensitivity m and strain rate $\dot{\varepsilon}$ on the flow stress curves are plotted in Fig. 6.4.

The geometry of the tube is specified as $H_0 = 0.5\ mm$, $R = 4\ mm$. The tube is assumed sufficiently long so that length changes as well as the end effects can be ignored and hence a plane strain analysis can be performed. The tube is meshed by plane strain elements (CPE4R in ABAQUS/Explicit), with 20 elements through thickness and 456 elements along the circumference. This mesh density is high enough to capture the localized strain during necking and will be used throughout the analysis. The desired dynamic loading conditions have been achieved by fixing $F_{\max} = 4.00X10^{11} N/m^3$ and varying the starting strain rate ε_0.

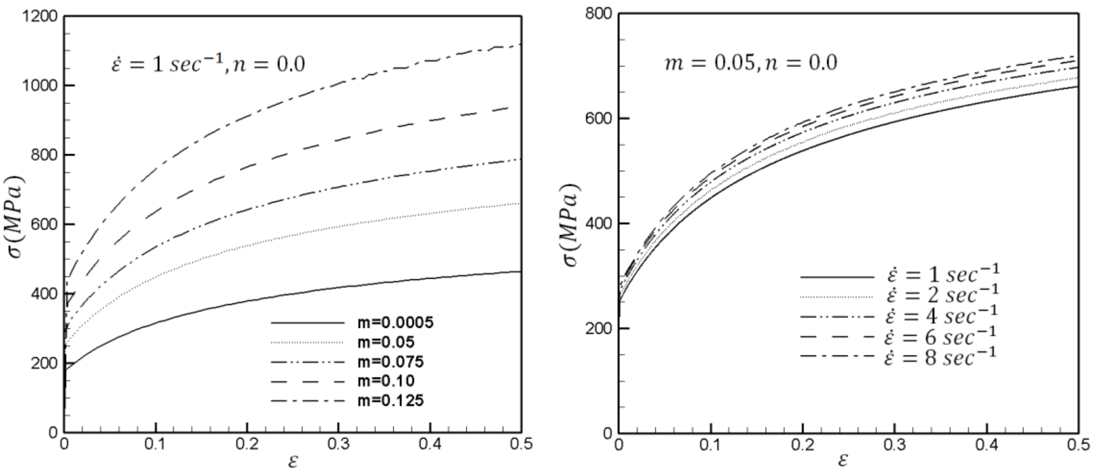

Effect of rate sensitivity m on flow stress   Effect of strain rate on flow stress

Figure 6.4 Predicted flow stress by the elastic-viscoplastic model

We first consider a rate-independent ($m = 0.0005$) material under high speed loading and the specimens are assumed to be geometrically perfect. Fig. 6.5 shows the deformed states of the quadrant of cylindrical tube under three loading speeds, $\dot{\varepsilon}_0 = 1385\ \mathrm{s}^{-1}$, $\dot{\varepsilon}_0 = 100\ \mathrm{s}^{-1}$ and $\dot{\varepsilon}_0 = 10\ \mathrm{s}^{-1}$, respectively. The contour plots of the effective plastic strain in the tube at the stages of necking are also presented. The deformation behaviors are quite different for different loading speeds. Even without any geometrical imperfections, under high speed loading ($\dot{\varepsilon}_0 = 1385\ \mathrm{s}^{-1}$), 10 typical necks are observed at $\Delta R / R_0 = 1.19$, compared with typically 2 necks at $\Delta R / R_0 = 0.51$ at a low speed loading ($\dot{\varepsilon}_0 = 10\ \mathrm{s}^{-1}$). It shows that the stress waves transmitted along the tube play a significant role under high speed loading to delay the onset of necking (high nominal hoop strain) and to facilitate multiple neck formation. The locations of the neck, in these three cases are quite different, depending on stress wave propagation, interaction with the instability points and the effect of inertia in the tube. Although no geometrical imperfections were introduced, there could be some numerical noise accumulated during the calculation in the Explicit FE codes to generate some bifurcation points and stress waves may contribute significantly to further develop such instability points and multiple-point necking. The higher the loading speed applied, the more fragmentation is generated. The nominal hoop strain $\Delta R / R_0$ also was significantly delayed with high-speed loading.

To assess the impact of initial geometrical imperfections on necking behavior, we implemented the idealized initial surface imperfection, described in Eqn. 6.12, into the

FE model. The imperfection profiles are chosen as $\delta = 0.002$ and $N_y = 8$, which generates 8 waves along the circumference of the quadrant of tube.

First, we look at a strain rate independent case. Fig. 6.6 shows the contour plot of the plastic strain at three different loading speeds, with $\dot{\varepsilon}_0 = 50\,\mathrm{s}^{-1}$ for the slowest speed loading and $\dot{\varepsilon}_0 = 1385\,\mathrm{s}^{-1}$ for the fastest. Under low speed loading ($\dot{\varepsilon}_0 = 50\,\mathrm{s}^{-1}$), a single neck is well-developed along with some under-developed necks at $\Delta R / R_0 = 0.47$. The initial outer surface imperfection does trigger the onset of necking at a relatively lower hoop strain level compared with a perfect geometry case (Fig. 6.5), but does not facilitate multiple necking at a low loading speed. The locations of neck are not directly associated with the initial thinnest cross-section regions specified by the imperfection. In the high speed loading ($\dot{\varepsilon}_0 = 1385\,\mathrm{s}^{-1}$), the contour of plastic strain indicates that potential necks are initiated and further developed simultaneously at the initial thinnest cross-section regions introduced by the imperfection. Compared with low-speed loading, the final deformation modes and number of necks are quite different. The multiple necking spots in high-speed loading are triggered by the imperfection and are facilitated by the interaction of the circumferential wave propagation and the specimen geometry change as the hoop strain $\Delta R / R_0$ increases to 0.63. The tube with high speed loading experiences an average high strain rate $\dot{R} / R_0$ in the order of 100 times the strain rate experienced by the low speed in radial expansion. Compared with the ideal geometry with no imperfection (Fig. 6.5), the initial imperfection is an important factor in triggering the onset of necking as the hoop strain levels are reduced when necking develops at three loading speeds.

However, similarly to the perfect geometry case, the loading speed is a dominant factor in determining multiple neck formation and the number of necks. These results are consistent with Madsen and Niordson’s experimental observations (1970) and Han and Tvergaard’s numerical analysis (1995).

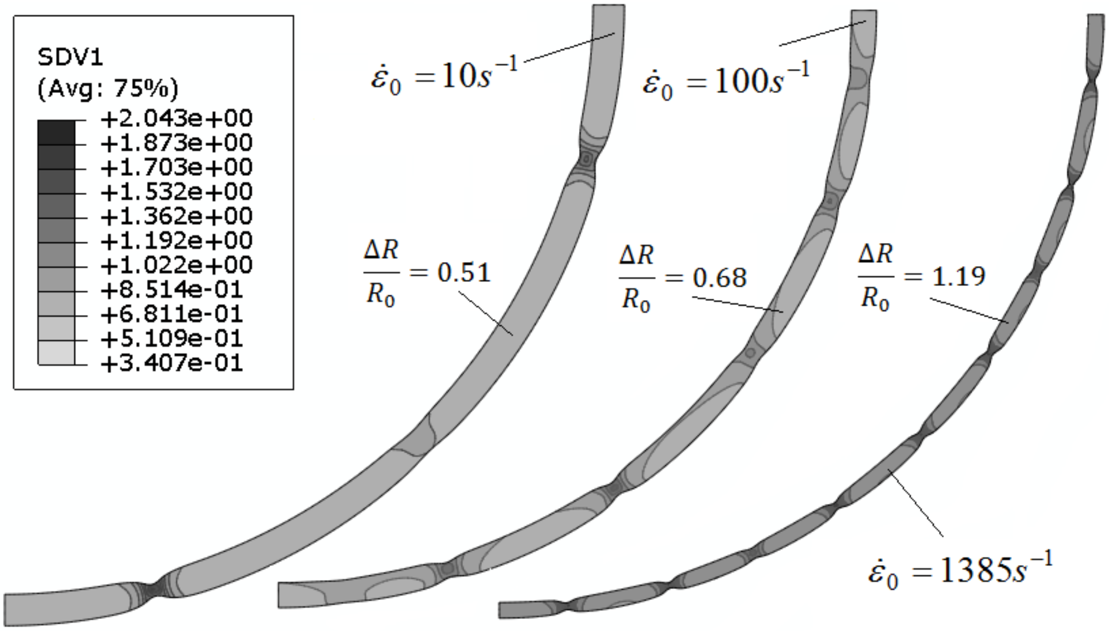

Figure 6.5 Effective plastic strain contour plot, rate independent materials $m = 0.0005$ without imperfection $\delta = 0.0$

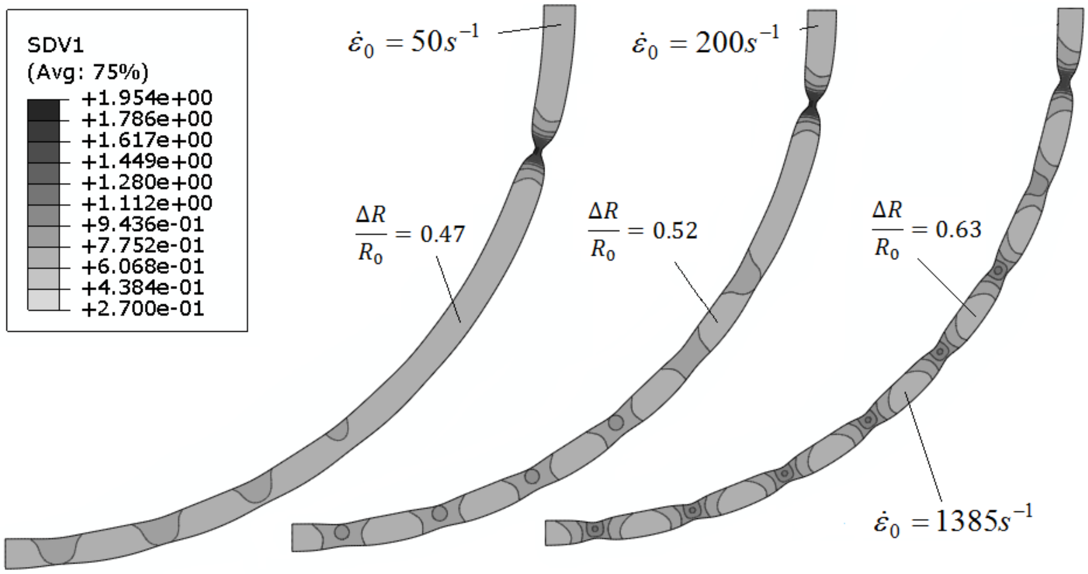

Figure 6.6 Effective plastic strain contour plot, rate independent materials $m = 0.0005$ with imperfection $\delta = 0.002$

The influence of an imperfection on the tube's maximum load and necking behaviors under high speed loading are further quantified in Fig. 6.7, Fig. 6.8, and Fig. 6.9. The obtained ε_{inside} vs $\varepsilon_{outside}$curves for three imperfection parameters are presented in Fig. 6.7. It shows that the localized necking strain is very sensitive to the imperfection coefficient. A near perfect tube has a higher necking strain than a tube with a high initial imperfection. Fig. 6.8 illustrates the effect of three different initial imperfections ($\delta = 0.002$, $\delta = 0.004$ and $\delta = 0.006$) on the loading history (nominal hoop traction T/σ_0) at a high speed ($\dot{\varepsilon}_0 = 1385$ s^{-1}). If we follow Shi et al. (2010) and defines the maximum nominal hoop traction T/σ_0 as the onset of the diffused necking, the diffused necking almost unchanged even though we do see necking retardation for different imperfection coefficients. This necking delay introduced by decreasing the magnitude of imperfection is more obvious in the normalized minimum cross section $A_{\min}/A_0$ plot in Fig. 6.9, where the $A_{\min}/A_0$ is equivalent to the nominal thickness strain. The changes in slope of the $A_{\min}/A_0$ vs $\Delta R/R_0$ plot defines the transition/evolution of diffused necking to localized necking as described in detail in Shi et al. (2010). Zhang and Ravi-Chandar (2008) conducted the rapid ring test and examined inside and outside the neck region; and found that the strain at the onset of diffused necking was found to be independent of the expanding velocity (or strain rate); however, the localized strain for sheet-mode necking increased with the expanding velocity. Using the definition of diffused and localized necking as specified early, we plotted the diffused and localized strains as a function of the initial strain rate $\dot{\varepsilon}_0$ in Fig 6.10. The localized strain increases with respect to the strain rate increase, however the diffused necking strain almost keeps unchanged. This result was attributed to inertial effects—specifically, the time taken for the localization to propagate across the dominant cross-sectional dimension; and agrees well with Zhang and Ravi-Chandar's observations (2008). To make it clear and simple, we will focus on the localized necking and we refer $\varepsilon_{necking}$ as the localized necking strain, or necking strain through the rest of work.

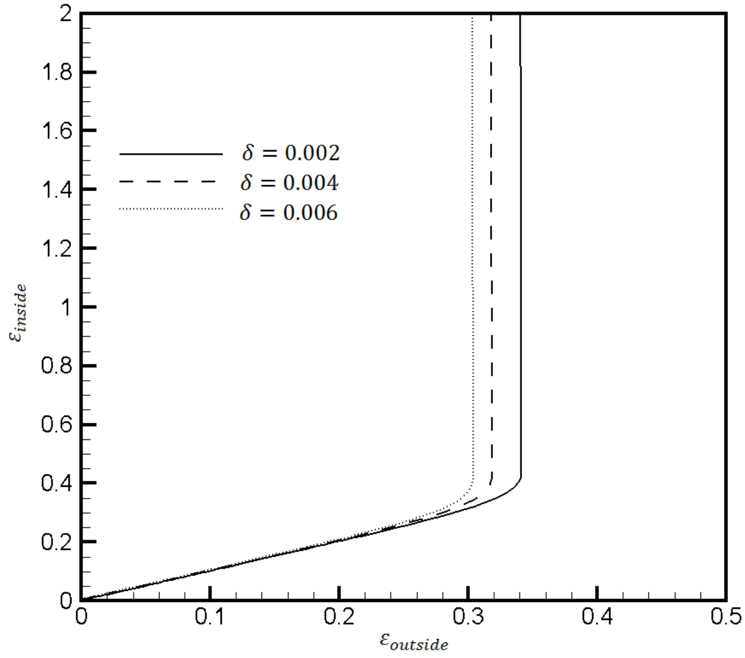

Figure 6.7 Effect of imperfection, ε_{inside} vs $\varepsilon_{outside}$, rate independent materials $m = 0.0005$ and $\dot{\varepsilon}_0 = 1385\ \text{s}^{-1}$.

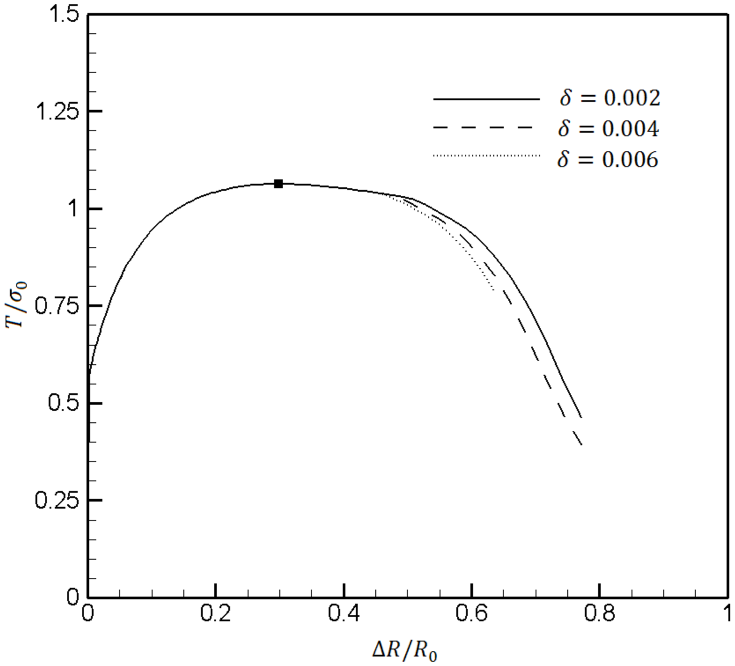

Figure 6.8 Effect of imperfection, nominal hoop traction T/σ_0 vs nominal hoop strain $\Delta R/R_0$, rate independent materials $m = 0.0005$ and $\dot{\varepsilon}_0 = 1385\ \text{s}^{-1}$, the solid square represents the maximum value of T/σ_0.

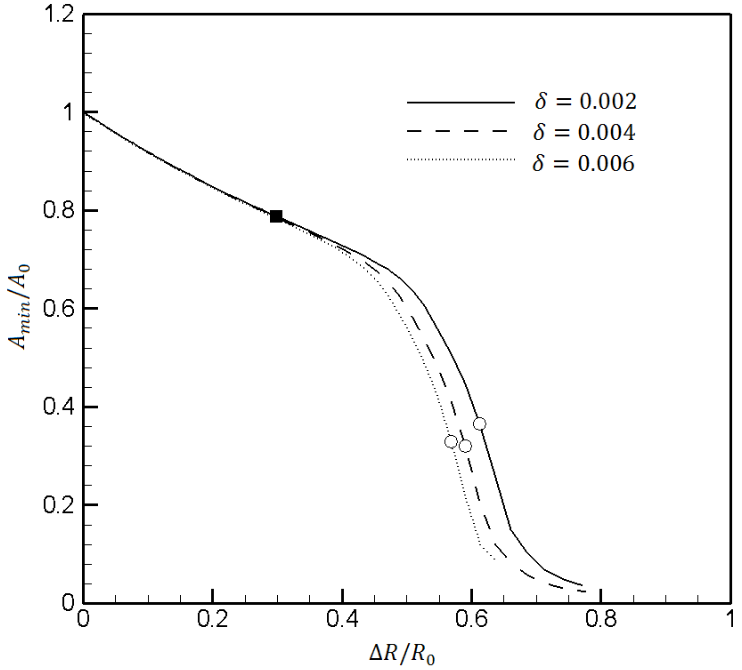

Figure 6.9 Effect of imperfection, nominal minimum cross section $A_{\min} / A_0$ vs nominal hoop strain $\Delta R / R_0$, rate independent materials $m = 0.0005$ and $\dot{\varepsilon}_0 = 1385\ \text{s}^{-1}$, the solid square is the diffused necking point and the open circle is the localized necking point.

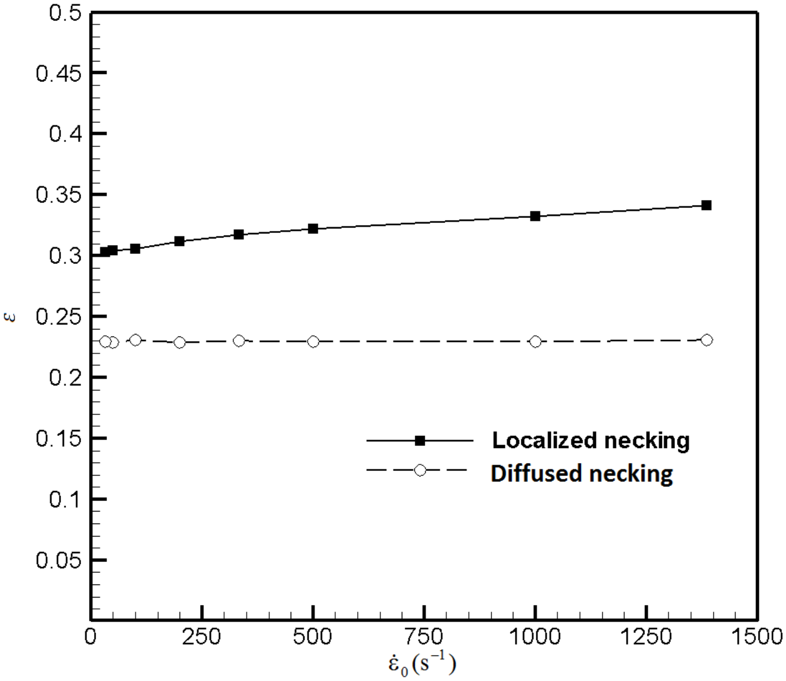

Figure 6.10. Effect of the starting strain rate $\dot{\varepsilon}_0$ on the diffuse and localized necking strain, rate independent materials $m = 0.0005$ and $\dot{\varepsilon}_0 = 1385\ \text{s}^{-1}$.

The study of rate sensitivity on the tube expansion is conducted through a change in the rate sensitivity value m, while keeping the rest of the parameters the same. Tube expansion under dynamic loading in a rate sensitive material is essentially a nonlinear process.

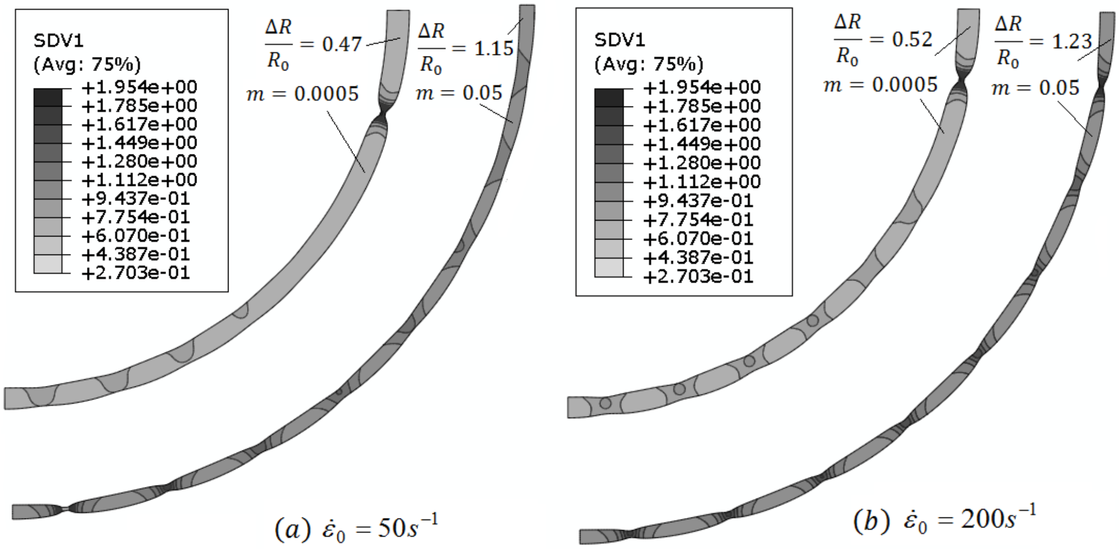

Figure 6.11 Effective plastic strain contour plot, rate independent materials $m = 0.0005$ vs rate sensitive materials ($m = 0.05$) with imperfection $\delta = 0.002$

The effect of rate sensitivity on the multiple necking formation and on the hoop strain at necking is shown in Fig. 6.11, which is a contour plot of the effective plastic strain with different rate sensitivity values ($m = 0.0005$ vs $m = 0.05$) at two different loading speeds with $\dot{\varepsilon}_0 = 50\ s^{-1}$, and $\dot{\varepsilon}_0 = 200\ s^{-1}$. A significant delay in the necking strain was observed as the rate sensitivity m increases from 0.0005 to 0.05. Hutchinson and Neale (1978) has studied the strain-rate dependence on necking retardation in a bi-axially-stretched sheet and pointed out that the strain rate sensitivity substantially increases the predicted necking strain. This phenomenon is also valid in more complicated loading conditions, such as the tube expansion under dynamic loading. Both high speed dynamic loading and high rate sensitivity will increase the ductility and delay necking. Considering multiple necks, high speed loading plays a significant role in the rate independent material (See Fig. 6.6). As the loading speed decreases, the tendency for multiple necks to occur also decreases, with 8 necks at $\dot{\varepsilon}_0 = 1385$ s^{-1}, 5 necks at $\dot{\varepsilon}_0 = 200$ s^{-1}, and 1 full neck with some partially formed necks at $\dot{\varepsilon}_0 = 50$ s^{-1}. For a rate sensitive material with $m = 0.05$, this reduction of number necks with respect to the decrease in loading speed has been delayed. In Fig. 6.11a, at a speed of $\dot{\varepsilon}_0 = 50$ s^{-1}, 6 typical necks are observed for material with a rate sensitivity of $m = 0.05$, compared with a single full neck in rate independent material ($m = 0.0005$); 8 necks are generated for rate sensitive material ($m = 0.05$), compared with 5 necks for the rate independent material ($m = 0.0005$) at a relatively high loading speed ($\dot{\varepsilon}_0 = 200$ s^{-1}). In other words, a high rate sensitivity will facilitate multiple neck formation to some degree. This could be due to the fact that the rate sensitive material experiences high deformation, which leads to a thinner gauge in the final deformation stages. The imperfection or non-uniformity in the thinner gauge tube makes it easier to trigger the onset of necking and further development of multi-necking as the scale of imperfection tends to increase with the decrease in thickness, which make it harder to resist plastic instability during high speed loading.

The effect of rate sensitivity on delay of localized necking has been quantified in the ε_{inside} vs $\varepsilon_{outside}$plot in Fig. 6.12 for materials with imperfection $\delta = 0.002$ at a high loading speed ($\dot{\varepsilon}_0 = 1385$ s^{-1}). Necking strain reaches close to 0.83 for a high rate sensitive material ($m = 0.1$) vs a much lower necking strain 0.34 for a rate independent material ($m = 0.0005$). The extracted necking strains for different rate sensitivity parameters are plotted in Fig. 6.13. For comparison, the necking strains for a relatively low loading speed ($\dot{\varepsilon}_0 = 50$ s^{-1}) are also included. It can be seen that necking strains increase almost linearly with the rate sensitivity m in both cases.

A long wavelength non-linear analysis has been proposed by Hutchinson and Neale (1977) and by Ghosh (1977) for uni-axial tension deformation of a round bar, where the deformation of the region of a small imperfection is monitored in comparison with that of the perfect region based on load equilibrium between the two regions. Their results show a linear relation of necking strain in terms of rate sensitivity, m under static loading condition.

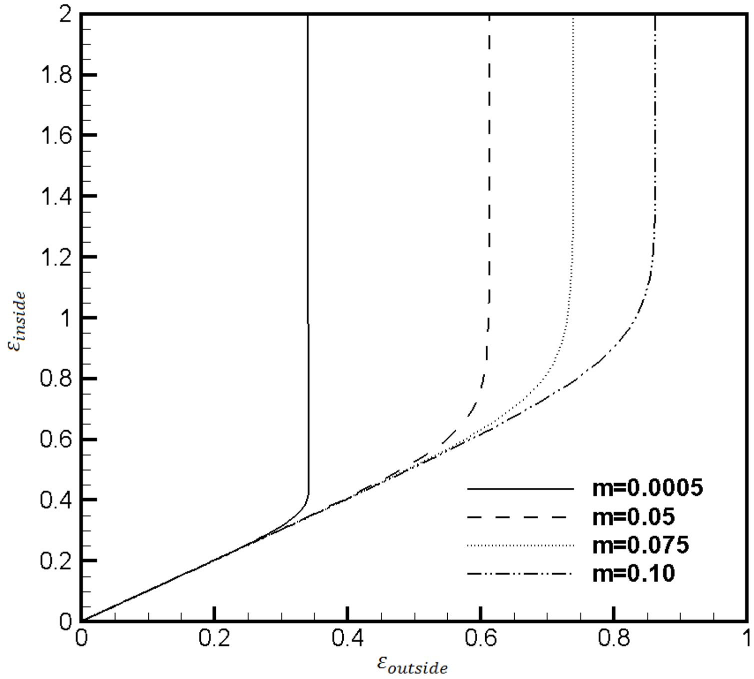

Figure 6.12 Effect of rate sensitivity, ε_{inside} vs $\varepsilon_{outside}$, materials with imperfection $\delta = 0.002$ and $\dot{\varepsilon}_0 = 1385$ s^{-1}.

The same conclusion can be drawn for the tube expansion with plane strain deformation in the dynamic loading condition, which is that the necking strain can be associated with the rate sensitivity as $\varepsilon_{necking} \propto m$. The difference is that in quasi-static loading (low speed loading), the slope of the necking strain in terms of rate sensitivity m is a constant value and is independent of strain rate. In high-speed dynamic loading, the slope of the necking strain curve changes with respect to the change of loading speed. This is because the necking strain retardation due to the dynamic loading and due to the rate sensitivity m both contribute to the overall necking strain delay. But for the same loading profile (a constant $\dot{\varepsilon}_0$), a linear relation of necking strain with respect to the rate sensitivity m is valid and the necking strain is independent of strain rate.

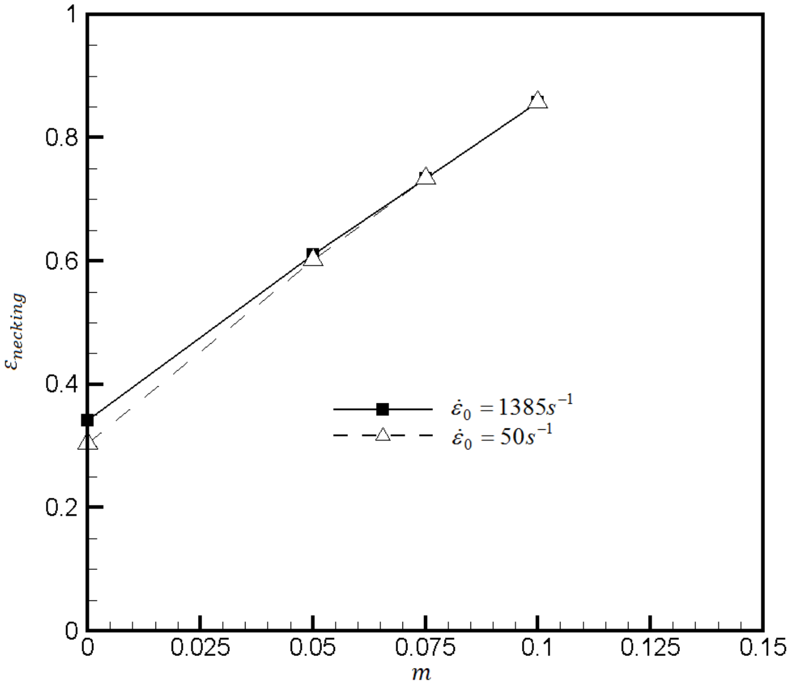

Figure 6.13 Effect of rate sensitivity, localized necking strain $\varepsilon_{necking}$ vs rate sensitivity m, materials with imperfection $\delta = 0.002$

Necking strains in terms of loading speed have been plotted for various rate sensitivities in Fig. 6.14 and normalized in Fig. 6.15 (with initial geometric imperfection: $\delta = 0.002$). Basically, the rate sensitivity determines the overall necking strain. However, for a material with a given rate sensitivity (whether rate dependent or independent materials), necking strain is almost insensitive to the change of loading speed at (or near) the low speed region (the quasi-static/static loading). But under high speed loading ($\dot{\varepsilon}_0 > 50$ s^{-1}, the dynamic loading region), the necking strain increases with respect to the increase in loading speed, but with different ratios. For rate independent material ($m = 0.0005$), the necking stain retardation is significant. The necking strain has increased more than 10% compared with the necking strain under quasi-static loading conditions. However, this influence of necking strain delay for dynamic necking is significantly suppressed as the rate sensitivity m increases. When m reaches 0.1, the necking strain is almost unchanged from static loading to a high-speed loading. The necking strain is dominated by the influence of rate sensitivity m and the influence of dynamic loading on necking can be ignored.

In terms of forming multiple necks, high-speed loading is a dominating factor in forming the multiple necks due to the interaction of stress wave propagation and the effect of inertia around the circumference. Rate sensitive material will facilitate this tendency as the loading speed is reduced.

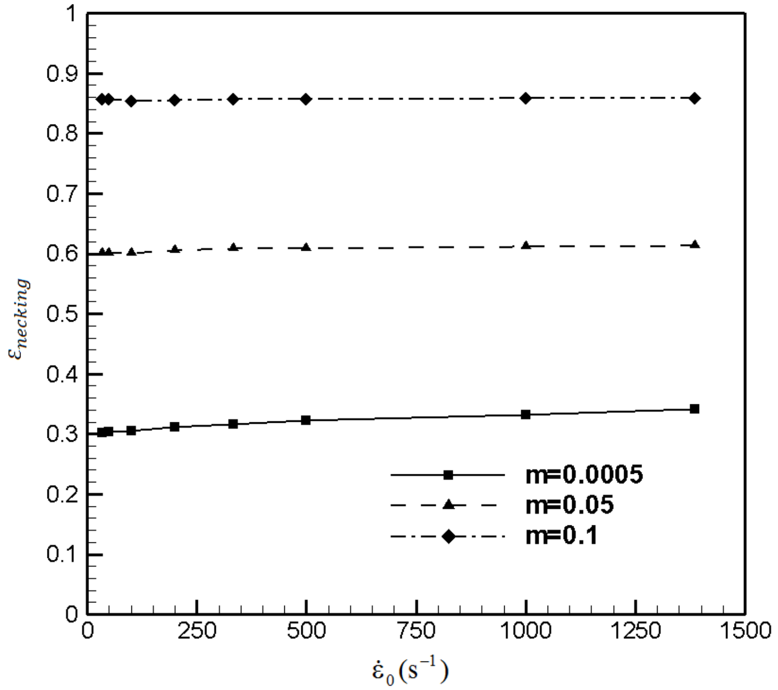

Figure 6.14 Effect of rate sensitivity, localized necking strain $\varepsilon_{necking}$ vs starting strain rate $\dot{\varepsilon}_0$, materials with imperfection $\delta = 0.002$

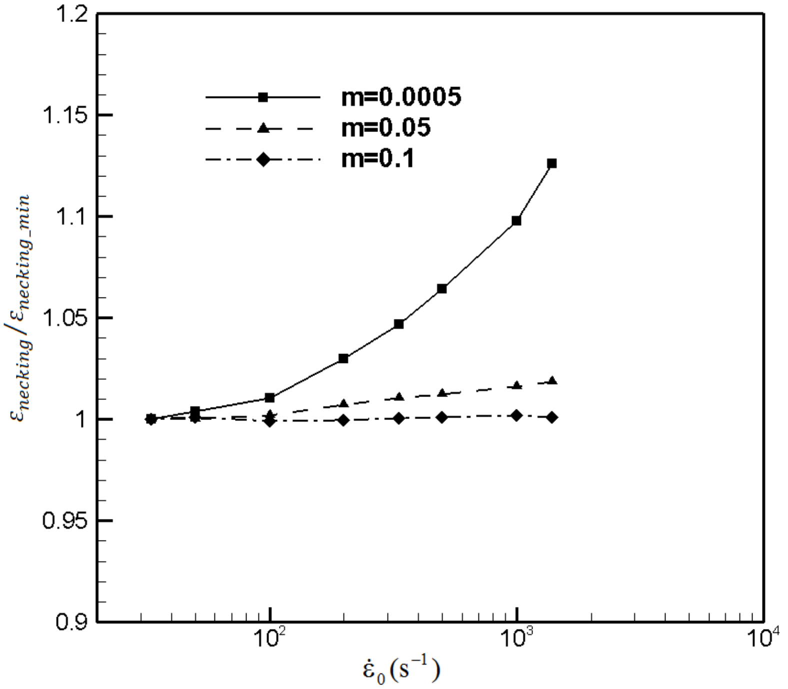

Figure 6.15 Effect of rate sensitivity, $\varepsilon_{necking}/\varepsilon_{necking\_\min}$ vs starting strain rate $\dot{\varepsilon}_0$, materials with imperfection $\delta = 0.002$.

In predicting necking strain, both dynamic loading and rate sensitivity result in necking retardation. But rate-independent material and less rate-dependent materials are more influenced by the loading speed.

6.3.2 Laminated composites

Both industry and research have shown a great interest in a laminated material which provides a wide range of design flexibility by combining materials with different properties. Manoharan (1990) showed laminated composites can considerably enhance fracture toughness, while Lloyd et al (2010) demonstrated improved bendability. Li (2006) and Kim et al. (2003)'s work provided a good insight on improving material formability or ductility through laminating a highly formable material on a base material with low formability. The numerical study of laminated steel sheet on ductility improvement also has been studied by Chen et al. (2007). It has been found that necking is effectively delayed by a clad layer and the improvement in necking strain is approximately proportional to the volume fraction of the clad material. In the current work, we focus on the necking behavior of laminated sheet under rapid dynamic loading. The laminated sheet is assumed to consist of a rate insensitive core material at the center laminated with a more ductile cladding of rate sensitive material on both sides of the core. It is assumed that there is perfect bonding between clad and core materials and no interfacial cracking happens. Fig. 6.16 shows a section of such a system with a core thickness of h_{core} and a clad thickness of h_{clad}. The rate sensitivity of the cladding material (m) and the relative thickness $p = 2h_{clad} / (2h_{clad} + h_{core})$ i.e. volume fraction of the cladding, should play an important role in such a system. These two parameters and their role in ductility will be explored in this finite element study. In this analysis, we apply constant high-speed loading with $\dot{\varepsilon}_0 = 1385$ s^{-1} and the same very small imperfection ($\delta = 0.002$) in all cases. To facilitate comparison, the clad layer has been chosen to have the same material parameters as the core which is rate-independent material, except for the difference in m values.

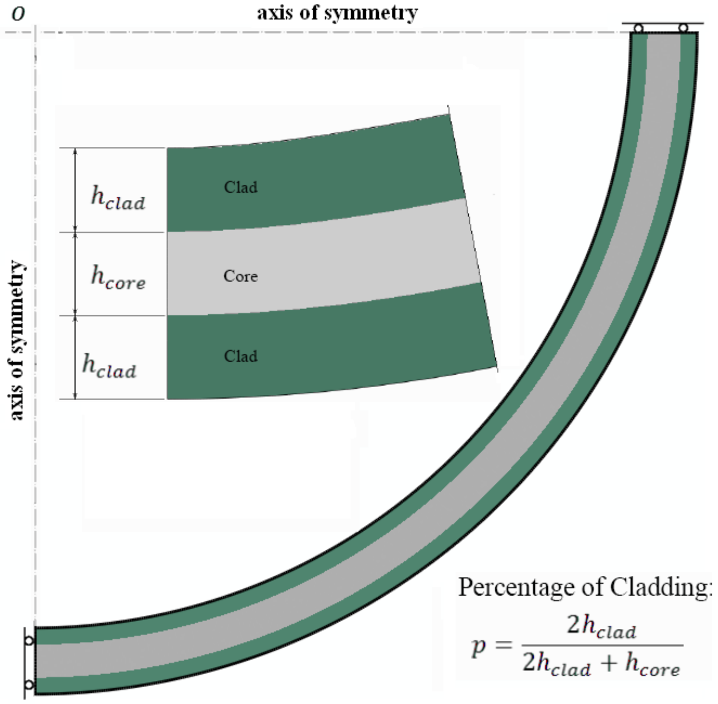

Figure 6.16 The sketch of the laminated composite system

Two types of parameter studies were performed:

(a) Vary the relative thickness p from 0 to 0.5, while fixing the rate sensitivity ($m =$ 0.1 or 0.05) of the cladding material.

(b) Vary the rate sensitivity (m) of clad material from 0 to 0.1, while fixing the relative thickness (p =0.1 or 0.3).

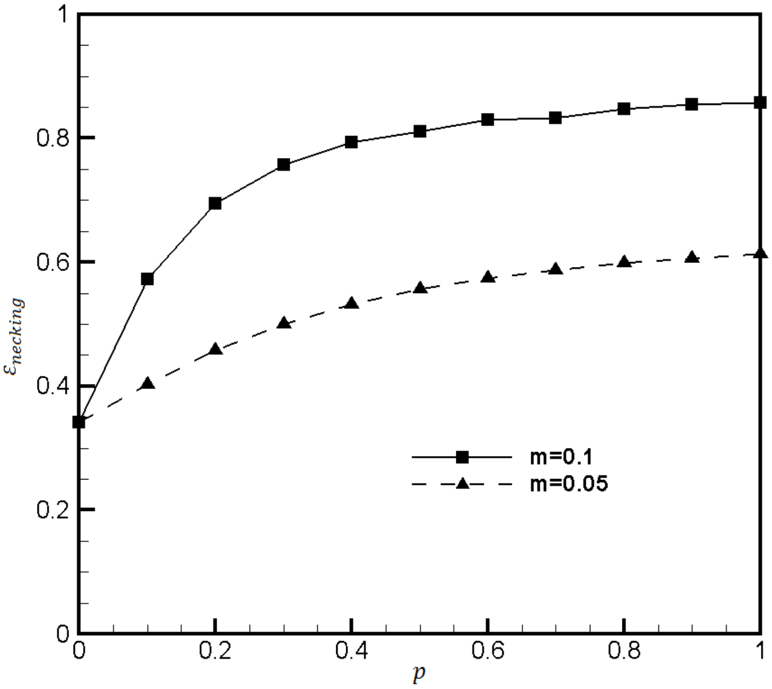

Figure 6.17 Effect of clad percentage p and rate sensitivity m on localized necking strain $\varepsilon_{necking}$, materials with imperfection $\delta = 0.002$ and $\dot{\varepsilon}_0 = 1385\ \mathrm{s}^{-1}$.

The predicted necking results are as shown in Fig. 6.17 and Fig. 6.18 for these two cases. The plots illustrate that the necking strains increase almost linearly with the volume fraction of the clad material in a low rate sensitive case (m =0.05) and parabolically in a high rate sensitivity case (m =0.1). For a high rate sensitive material (m =0.1), the first 10% of cladding significantly improves the ductility and the necking strain has been improved by 80% through the contribution of a 10% clad layer. Beyond the 10% level, the improvements are diminished, even though the clad percentage proportionally increases. The final 10% increase of clad percentage (from 90% to 100%)

can only contribute less than 5% improvement in the necking strain. When the volume fractions are fixed at 0.1 and 0.3, the necking strains increase monotonically with the strain rate sensitivity.

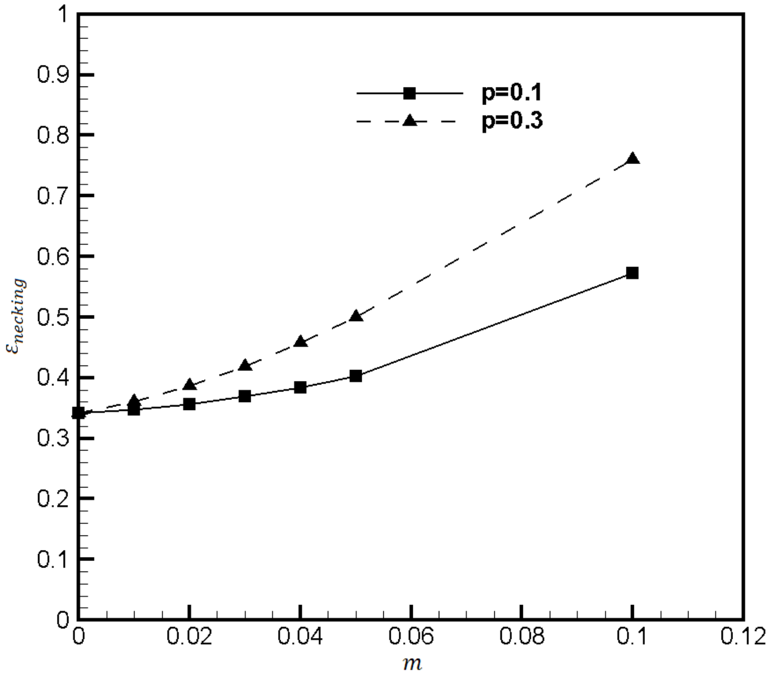

Figure 6.18 Effect of clad percentage p and rate sensitivity m on localized necking strain $\varepsilon_{necking}$, materials with imperfection $\delta = 0.002$ and $\dot{\varepsilon}_0 = 1385$ s^{-1}.

Fig. 6.19 shows the predicted necking strain in the clad layer with two different rate sensitivity values, a low m case (m=0.05) and a high m case (m=0.1). As shown in Fig. 6.14 and Fig. 6.15, for a monolithic rate independent material, the necking strain increases significantly as the loading speed increases. However such improvement diminishes for rate sensitive material as m increases. But, in a laminated system with a high rate sensitivity value in the clad layer, the high speed dynamic loading still results in a higher necking strain. Due to strain compatibility at clad-core interface, even though the clad layer benefits the overall ductility of the material, a high volume fraction core still dominates the necking strain level of the whole tube because the volume fraction of clad layer (10% in this case) is small compared with the whole laminated system. Obviously, as the rate sensitivity values in the clad layer increases, the overall necking strain level improves accordingly.

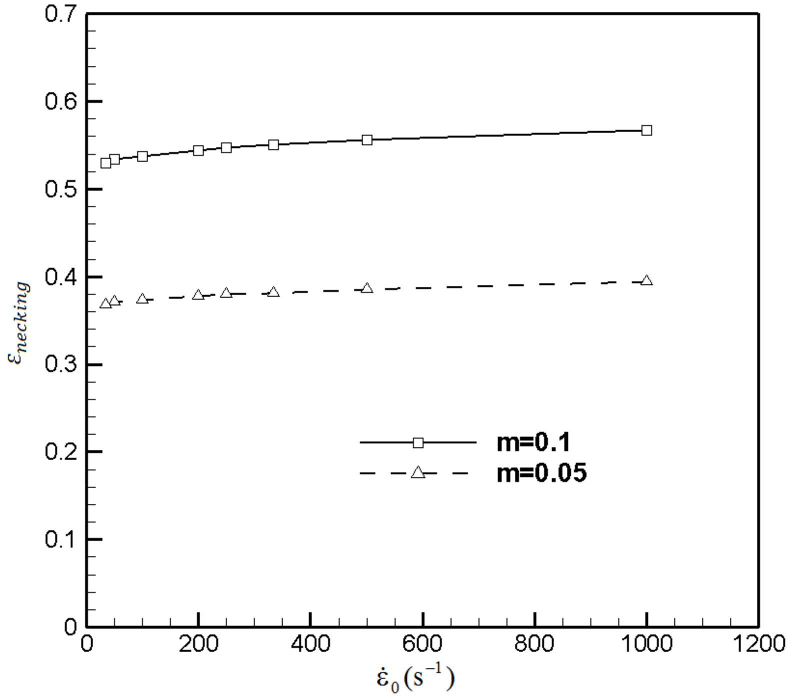

Figure 6.19 Effect of rate sensitivity m on localized necking strain $\varepsilon_{necking}$ in the laminated composite system, materials with imperfection $\delta = 0.002$ and $\dot{\varepsilon}_0 = 1385\ s^{-1}$.

6. 4 Conclusions

A plane strain elastic-viscoplastic based finite element model has been developed to simulate rapid tube expansion under dynamic loading conditions. For rate independent materials, it was found that the strain at the onset of diffuse necking was found to be independent of the expanding velocity (or strain rate); however, the localization necking strain increased with the expanding velocity. This finding agrees well with with Zhang and Ravi-Chandar's observations (2008).

The effect of the rate sensitivity on the necking strain and formation of multiple-necking has been studied for the monolithic material. It was found that both loading speed and rate sensitivity will contribute to the necking strain retardation from quasi-static loading to dynamic loading. However, as the rate sensitivity increases, the effect of dynamic loading is reduced. In predicting multiple necking, high speed dynamic loading is the key factor to generate the multiple-necks due to the interaction of stress wave propagation and effect of inertia in the tube. Previously, Ghosh (1977) and Hutchinson and Neale (1978) found that the necking strains was independent of the loading speed and strain rate for a material with constant strain rate sensitivity. This conclusion is only valid under the quasi-static loading condition. In dynamic loading, a linear relationship between the necking strain and rate sensitivity m is observed for a specific loading profile. The slope of this linear relation is dependent on the loading speed/profile changes.

The influence of strain rate sensitivity on laminated material during dynamic loading has also been studied through FE modeling. Unlike the monolithic materials with constant rate sensitivity, the necking behaviors of laminated material with a rate-dependent cladding on a rate independent core are highly dependent on the loading speed and the cladding percentage. With the assumption of constant rate sensitivity of the cladding material, higher loading rate and high rate sensitivity can significantly delay necking initiation and development in the laminated system. This conclusion is reasonable, since the contribution of the cladding material to the total force increases due to the increase of flow stress with higher strain rate, leading to a more dominant role of the rate dependent cladding material on necking behaviors. This conclusion gives an important indication for the design of the forming processes where higher forming rate would be beneficial for the formability of such a laminated sheet.

It should be noted that the strain rate sensitivity is a function of alloy, strain rate, strain and temperature and may vary differently between cladding and core. Therefore, such complexity over the constitutive behavior of the material needs to be addressed in future analyses for predicting more precisely the necking instability and formability of a material under dynamic loading condition.

This research work is under preparation for submission.

Chapter 7

Conclusions and Future Work

The research presented in this thesis has focused on an effort to incorporate different physical models (dislocation based MTS models, crystal plasticity and rate sensitivity plasticity) into a framework to simulate the plastic deformation and failure behavior of aluminum tubes under various loading conditions.

In the study of aluminum plastic deformation behavior under high temperature and various strain rates, we used a dislocation based MTS model to capture thermal-mechanical behavior and response of aluminum sheet at 300°C to 400°C forming temperature. The pressure ram forming process has been simulated by implementing the MTS model in ABAQUS through a user material subroutine (UMAT). The predicted shape, thickness distribution and backing load of the PRF aluminum bottle and its forming process were found to be in good agreement with measurements.

In the study of aluminum tube failure under pressurization, a crystal plasticity based FE model has been used to demonstrate the origins of strain localization. The work is devoted to the study of mechanical instabilities, which give rise to microstructure pattern formation and eventual failure of stressed solids, because of the strong link between mechanical instabilities and failure. A plane strain crystal plasticity based finite element model has been developed to simulate localized necking in an aluminum tube under internal pressure. The measured EBSD data for the sheet are mapped onto the tube and then directly incorporated into the finite element model and the constitutive response at an integration point is described by the single crystal plasticity theory. Localized necking in tubes under internal pressure has been associated with surface instability and the onset of unstable thinning. It has been demonstrated that such a surface instability/necking and surface roughening are the natural outcome of the present approach, and an artificial initial imperfection required by other approaches is not necessary in the present analysis. The effects of spatial orientation distribution, strain rate sensitivity, work hardening, and initial surface topography on necking and surface roughening have been discussed. It has been demonstrated that while the initial surface topography has little influence on localized necking which depends strongly on both the initial texture and its spatial orientation distribution, it contributes significantly to the surface roughness on the hydro-formed tube.

The present research has provided a methodology for including physical mechanisms of plastic deformation into the framework of finite element crystal plasticity. As such, we have shown that this framework is successful in predicting the formation of localized shear bands in single crystals. The spatial distribution of local plastic shear strain has been shown to be quite heterogeneous within grains, even though the applied strain is initially uniform in the crystal. Future work may be able to shed more light on the physical origins of plastic instabilities in 3D crystals with more advanced dislocation models, such as incorporating MTS models into the crystal plasticity framework so more complicated deformation (high temperatures, high strain rate) can be modeled at a microstructure level.

A plane strain elastic-viscoplastic based finite element model has been developed to simulate tube rapid expansion in dynamic loading conditions. The effect of rate sensitivity on necking strain prediction and formation of multiple necks has been studied for the monolithic material. It was found that both loading speed and rate sensitivity will contribute to necking strain retardation from quasi-static loading to dynamic loading. However, as rate sensitivity increases, the effect of dynamic loading will be reduced. In predicting the multiple necks, high speed dynamic loading is the key factor to generate the multiple necks due to the interaction of stress wave propagation and effect of inertia in the tube.

It has been addressed previously by Ghosh (1977) and Hutchinson and Neale (1978) that necking strains calculated are independent of the actual loading speed and strain rate for a material with constant strain rate sensitivity. This conclusion is only valid in the quasi-static loading condition. In dynamic loading, the linear relationship between the necking strain and rate sensitivity m is observed for a specific loading profile. The slope of this linear relation could change as the loading speed/profile changes. The assumption of constant strain rate sensitivity, however, cannot usually be guaranteed in ordinary rate dependent materials. For many superplastic materials such as the fine grained Al, Mg and Ti alloys deformed at elevated temperatures, ductility depends on the strain rate and strain rate sensitivity usually changes with strain rate. Ductility is usually larger for deformation at relatively slower strain rates due to the higher strain rate sensitivity at lower strain rate.

The influence of strain rate sensitivity on laminated material during dynamic loading also has been studied through FE modeling. Unlike the monolithic materials with constant rate sensitivity, the necking behaviors of laminated material with rate-dependent cladding on the rate independent core materials are highly dependent on the loading speed and cladding percentage.

It should be noted that strain rate sensitivity is a function of alloy, strain rate, strain and temperature and may vary differently between cladding and core. Therefore, such complexity over the constitutive behavior of the material needs to be addressed in future analyses for predicting more precisely the necking instability and formability of a material in dynamic loading conditions.

List of References

ABAQUS Inc. (2006). *ABAQUS Manual*, Version 6-5.1.

Ahmetoglu, M. and Altan, T. (2000). Tube hydroforming: state-of-the-art and future trends, *J. Mater. Process. Technol.*, 98, 25-33.

Anand, L. and Kalidindi. S. R. (1994). The process of shear band formation in plane strain compression of fcc metals: effect of crystallographic texture, *Mech. Mater.*, 17.

Anand, L. and Kathari, M. A. (1996). A computational procedure for rate independent crystal plasticity, *J. Mech. Phys. Solids*, 44.

Asaro, R. J. (1983a). Micromechanics of crystal and polycrystals, *Adv. Appl. Mech*., 23, 1–115.

Asaro, R. J. (1983b). Crystal plasticity, *ASME J. Appl. Mech.*, 50, 921–934.

Asaro, R. J. and Needleman, A. (1985). Texture development and strain hardening in rate dependent polycrystals, *Acta Metall.*, 33.

Asaro, R. J. and Rice, J. R. (1977). Strain localization in ductile single crystals, *J. Mech. Phys. Solids*, 25, 309–338.

Asnafi, N. and Skogsgardh, A. (2000). Theoretical and experimental analysis of stroke-controlled tube hydroforming, *Mater. Sci. Eng.*, A279, 95–110.

Bammann, D. (1990). Modeling temperature and strain rate dependent large deformation of metals, *Applied Mechanics Review*, 43, S312-S319.

Bammann, D. and Dawson, P. (1993). Modeling the initial state of a material and its effect on further deformation, In *Material Parameter Estimation for Modern Constitutive Equations*, 13-20.

Bammann, D., Chiesa, N. and Johnson, G. (1996). Modeling large deformation and failure in manufacturing process, In *Theoretical and Applied Mechanics---Proceeding of the XIXth international Congress of Theoretical and Applied Mechanics*.

Banerjee, B (2007). The Mechanical Threshold Stress model for various tempers of AISI 4340 steel, *Int. J. Solids and Structures*, Volume 44, Issues 3–4, 834–859.

Banovic, S. W. and Foecke, T. (2003). Evolution of strain-induced microstructure and texture in commercial aluminium sheet under balanced biaxial stretching, *Mater. Trans. A*, 34A, 657-671.

Beaudoin, A. J., Bryant, J. D. and Korzekwa, D. A. (1998). Analysis of ridging in aluminum auto sheet metal, *Metall. Mater. Trans.* A, 29, 2323–32.

Becker, R. (1998). Effect of strain localization on surface roughening during sheet forming, *Acta Metall.*, 46, 1385–1401.

Becker, R. (2002). Ring fragmentation predictions using the Gurson model with material stability conditions as failure criteria, *Int. J. Solids and Structures*, 39, 3555-3580.

Bonet, J. and Wood, R. (1997). *Nonlinear continuum mechanics for finite element analysis*, Cambridge University Press, United Kingdom.

Borja, R. I. and Wren, J. R. (1993). Discrete micromechanics of elastoplastic crystal, *Int. J. Numer. Methods Eng.*, 36, 3815–3840.

Bronkhorst, C. A., Kalidindi, S. R. and Anand, L. (1992). Polycrystal plasticity and evolution of crystallographic texture in face-centered cubic metals, *Phil. Trans. Royal Soc., London A*, 341, 443–477.

Chen, A. Y., Zhang, J. B., Lu, J., Lun, W. and Song, H. W. (2007). Necking propagated deformation behavior of layer-structured steel prepared by co-warm rolled surface nanocrystallized 304 stainless steel, *Materials Letters*, 61, 5191-5193.

Chen, G., Shen, H., Hu, S. and Baudelet, B. (1990). Roughening of the free surfaces of metallic sheets during stretching forming, *Mat. Sci. Eng*. A, 128, 33–38.

Chen, S. F., Kocks, U. F., MacEwen, S. R., Beaudoin, A. J. and Stout, M. G. (1998). Constitutive modeling of a 5182 aluminum as a function of strain rate and temperature, In *Hot Deformation of Aluminum Alloys II, The Minerals, Metal and Material Society*, 205-216.

Chen, X. X., Wu, P. D., Embury, J. D., Huang, Y., (2010a). Enhanced ductility in round tensile bars produced by cladding a ductile ring, *Modelling and Simulation in Materials Science and Engineering 18*, article number 025005.

Chen, X. X., Wu, P. D., Lloyd, D. J., Embury, J. D., Huang, Y., (2010b). Enhanced ductility in sheet metals produced by cladding a ductile layer, *Journal of Applied Mechanics-Transaction of The ASME 77*, article number 041015.

Chen, A. Y., Zhang, J. B., Lu, J., Lun, W., and Song, H. W., (2007). Necking propagated deformation behavior of layer-structured steel prepared by co-warm rolled surface nanocrystallized 304 stainless steel, *Materials Letters*, 61, 5191-5193.

Christoffersen, J. and Hutchinson, J. W. (1979). A class of phenomenological corner theories of plasticity, *J. Mech. Phys. Solids*, 27, 465e487.

Chu, C. C. (1979). Bifurcation of elastic-plastic circular cylindrical shells under internal pressure, *J. Appl. Mech. Trans.*, ASME 46, 889e894.

Cook, R. and Malkus, D. (2002). *Concept and application of finite element analysis*, John Wiley & Sons Inc., United States.

Cuitino, A. M. and Ortiz, M. (1992). Computational modeling of single crystals, *Modeling and Simulation in Materials Science and Engineering*, 1, 225–263.

Dai, Y. Z. and Chiang, F. P. (1992). Effects of deformation mode on surface roughening of austenitic stainless steels, *J. Eng. Mater. Technol.*, 114, 432-438.

Dawson, P. R., Mika, D. P. and Barton, N. R. (2002). Finite element modeling of lattice misorientations in aluminum alloys, *Scripta Mater.*, 47, 713–717.

Fineberg, J., Sharon, E. and Gross, S. P. (2003). Crack front waves in dynamic fracture, *Int. J. of Frac.*, 119, 247-261.

Follansbee, P. S. and Kocks, U. F. (1988). A constitutive description of the deformation of copper based on the use of mechanical threshold stress as an internal state variable, *Acta Metall.*, 36, 81-93.

Fyfe, I. M. and Rajendran, A. M. (1980). Dynamic pre-strain and inertia effects on the fracture of metals, *J. Mech, Phys. Solids*, 28, 17-26.

Ghosh, A. K. (1977). Tensile instability and necking in materials with strain hardening and strain-rate hardening, *Acta Metall*, 25, 1413-1424.

Ghosh, A. K. (1980). A physically-based constitutive model for metal deformation, *Acta Metall*, 28, 1443-1465.

Goerdeler, M. and Gottstein, G. (2001). A microstructure work hardening model based on three internal state variables, *Mater. Sci. Eng. A*, 309-310, 337-381.

Gong, K., Hamstra, P., MacEwen, S., Mallory, R. and Moulton, J. D. (2004). Method of and apparatus for Pressure-Ram-Forming metal containers and like, US Patent: US 6,802,196 B2.

Grady, D. E. and Bensen, D. A. (1983). Fragmentation of metal rings by electromagnetic loading, *Exp. Mech*., 12, 393–400.

Guan, Y., Pourboghrat, F. and Barlat, F. (2006). Finite element modeling of tube hydroforming of polycrystalline aluminum alloy extrusions, *Int. J. Plasticity*, 22, 2366e2393.

Han, J. B. and Tvergaard, V. (1995). Effect of inertia on the necking behavior of ring specimens under rapid expansion, *Eur. J. Mech. A/Solids*, 14, 287-307.

Hartl, C. (2005). Research and advances in fundamentals and industrial applications of hydroforming, *J. Mater. Process. Technol.*, 167, 383e392.

Hill, R. (1958). A general theory of uniqueness in stability in elastic-plastic solids, *J. Mech. Phys. Solids*, 6, 236e249.

Hill, R. (1966). Generalized constitutive relations for incremental deformation of metal crystals by multislip, *J. Mech. Phys. Solids*, 14:95–102, 1966.

Hill, R. and Rice, J. R. (1972). Constitutive analysis of elastic-plastic crystals at arbitrary strain, *J. Mech. Phys. Solids*, 20, 401–413.

Hughes, T. (1984). Numerical implementation of constitutive models: rate-independent deviatoric plasticity, In *Theoretical foundation for large-scale computations of nonlinear material behavior*, Martinus Nijhoff Publishers, 29-57.

Huang, H., Gao, H., Nix, W. D. and Hutchinson, J. W. (2000). Mechanism-based strain gradient plasticity ii. Analysis, *J. Mech. Phys. Solids*, 48, 99128.

Huang, Y. (1991). A User-Material Subroutine Incorporating Single Crystal Plasticity in the ABAQUS Finite Element Program, *Mech. Report 178, Division of Applied Sciences*, Harvard University, Cambridge, MA, USA.

Hutchinson, J. W. and Neale, K. W. (1977). Influence of strain-rate sensitivity on necking under uniaxial tension, *Acta Metall*., 25, 839-846.

Hutchinson, J. W. and Neale, K. W. (1977). Influence of strain-rate sensitivity on necking under uniaxial tension, *Acta Metall*., 25, 839e846.

Hutchinson, J. W. and Neale, K. W. (1978). Sheet necking-III, strain-rate effects, *Mechanics of Sheet Metal Forming*, 269-285.

Inal, K., Wu, P. D. and Neale, K. W. (2002a). Instability and localized deformation in polycrystalline solids under plane strain tension, *Int. J. Solid Struct*., 39, 983e1002.

Inal, K., Wu, P.D. and Neale, K.W. (2002b). Finite element analysis of localization in FCC polycrystalline sheets under plane stress tension, *Int. J. Solid Struct*., 39, 3469e3486.

Jansson, M., Nilsson, L. and Simonsson, K. (2005). On constitutive modeling of aluminum alloys for tube hydroforming applications, *Int. J. Plasticity*, 21, 1041e1058.

Johnson, G. R. and Cook, W. H. (1983). A constitutive model and data for metals subjected to large strains, high strain rates, In *Proceedings of the 7th International Symposium on Ballistics*, 541–547.

Johnson, G. R. and Cook, W. H. (1985). Fracture characteristics of three metals subjects to various strains, strain rates, temperatures and pressures, *Eng. Fract. Mech*., 21, 31–48.

Kalidindi, S. R., Bronkhorst, C. A. and Anand, L. (1992). Crystallographic texture evolution in bulk deformation processing of FCC metals, *J. Mech. Phys. Solids*, 40, 537e569.

Kim, K. J., Kim, D., Choi, S. H., Chung, K., Shin, K. S., Barlat, F., Oh, K. H. and Youn, J. R. (2003). Formability of AA5182/polypropylene/AA5182 sandwich sheets, *J. Mater. Process. Technol.*, 139, 1-7.

Kipp, M. E. and Grady, D. E. (1985). Dynamic fracture growth and interactions in one dimension J. Mech. Phys. Solids, 33, 399–415.

Knoche, P. and Needleman, A. (1993). The effect of size on the ductility of dynamically loaded tensile bars, *Eur. J. Mech. A/Solids*, 12, 585-601.

Koc, M. and Altan, T. (2001). An overall review of the tube hydroforming (THF) technology, *J. Mater. Process. Technol*., 108, 384e393.

Kocks, U. F. and Mecking, H. (2003). Physics and phenomenology of strain hardening: the FCC case, *Prog. Mater. Sci.*, 48, 171-273.

Korkolis, Y. P. and Kyriakides, S. (2008). Inflation and burst of anisotropic aluminum tubes for hydroforming applications, *Int. J. Plasticity*, 24, 509e543.

Korkolis, Y. P. and Kyriakides, S. (2009). Path-dependent failure of inflated aluminum tubes, *Int. J. Plasticity,* 25, 2059e2080.

Krieg, R. and Krieg, D. (1977). Accuracies of numerical solution methods for the elastic-perfectly plastic model, *J. pressure Vessel Technol*., 510-515.

Kuwabara, T., Yoshida, K., Narihara, K. and Takahashi, S. (2005). Anisotropic plastic deformation of extruded aluminum alloy tube under axial forces and internal pressure, *Int. J. Plasticity,* 21, 101e117.

Kyriakides, S. and Chang, Y.C. (1990). On the inflation of a long elastic tube in the presence of axial load, *Int. J. Solid Struct.,* 26, 975e991.

Lang, L. H., Wang, Z. R., Kang, D. C., Yuan, S. J., Zhang, S. H., Danckert, J. and Nielsen, K. B. (2004). Hydroforming highlights: sheet hydroforming and tube hydroforming, *J. Mater. Process. Technol.*, 151, 165–177.

Larsson, M., Needleman, A., Tvergarrd, V. and Storakers, B. (1982). Instability and failure of internally pressurized ductile metal cylinders, *J. Mech. Phys. Solids,* 30, 121.

Li, D. and Ghosh, A. (2003). Tensile deformation behavior of aluminum alloys at warm forming temperatures, *Mater. Sci. Eng.,* A352, 279-286.

Li, D. and Ghosh, A., (2004). Biaxial warm forming behavior of aluminum sheet alloys, *J. Mater. Process. Technol.,* 145, 281-293.

Li, T. and Suo, Z. (2006). Deformability of thin metal films on elastomer substrates, *Int. J. Solid Struct.*, 43, 2351-2363.

Lindgreen, B., Tvergaard, V. and Needleman, A. (2008). Dynamic neck development in a polymer tube under internal pressure loading, *Int. J. Solid Struct.,* 45, 580e592.

Lloyd, D. J., Gallerneault, M. and Wagstaff, R. B., 2010. The deformation of clad aluminum sheet produced by direct chill casting, Metall. Mater Trans. vol.519-521, 2093-2103.

Lush, A., Weber, G. and Anand, L. (1989). An implicit time-integration procedure for a set of internal variable constitutive equations for isotropic elasto-viscoplasticity, *Int. J. Plasticity*, 5, 521-549.

Madsen, P. and Nirdson, F. I. (1970). Material properties at high strain rates, *progress report No. 8, to U.S. Air Force Material Lab*.

Mallory, R and Shi, Y. (2011). Methods of PRF forming with thickness gradient controlled perform, Novelis, WO 2011/085472.

Manoharan, M., Ellis, L. and Lewandowski, J. J. (1990). Laminated composites with improved toughness, *Scripta Mater.*, 24, 1515-1519.

Marin, E. B. and Dawson, P. R. (1998). Elastoplastic finite element analyses of metal deformation using polycrystal constitutive models, *J. Comp. Methods in Applied Mech. & Eng.*, 165, 23–41.

Maudlin, P. J., Davidson, R. F. and Henninger, R. J. (1990). Implementation and assessment of the Mechanical –Threshold –Stress Model using the EPIC2 and PINON computer codes, *Report LA-11895-MS*, Los Alamos national laboratory.

Miehe, C. and Schroder, J. (2001). A comparative study of stress update algorithms for rate-independent and rate-dependent crystal plasticity, *Int. J Numer. Methods Eng.*, 50, 273–298.

Mikkelsen, L. P. and Tvergaard, V. (1999). A nonlocal two-dimensional analysis of instabilities in tubes under internal pressure, *J. Mech. Phys. Solids*, 47, 953e969.

Miller, A., Ed. (1987). *Unified constitutive Equations for Creep and Plasticity,* Elsevier Applied Science, London & New York.

Miller, O., Freund, L. B. and Needleman, A. (1999). Modeling and simulation of dynamic fragmentation in brittle materials, *Int. J.Fract*., 96, 101–25.

Mott, N. F. (1947). Fragmentation of shell cases, *Proc. R. Soc. Lond. Ser. A*, 189 300–8.

Nagtegall, J. and Veldpaus, F. (1984). On the implementation of finite strain plasticity equations in a numerical model, In *Numerical analysis of forming processes*, John Wiley & Sons. Inc, 351-371.

Needleman, A. (1991). The effect of material inertia on neck development, *Topics in plasticity*, Yang, W. H. Ed., AM Press, Ann Arbor, MI, 151-160.

Pandolfi, A., Krysl, P. and Ortiz, M. (1999). Finite element simulation of ring expansion and fragmentation: the capturing of length and time scales through cohesive models of fracture, *Int. J. Fract.*, 95, 279–97.

Peirce, D., Asaro, R. J. and Needleman, A. (1982). An analysis of nonuniform and localized deformation in ductile single crystals, *Acta Metall*, 30.

Peirce, D., Shih, C. F., and Needleman, A., (1984). A tangent modulus method for rate dependent solids, *J. Computer & Structures*, 18, 5, 875-887.

Rice, J. R. (1971). Inelastic constitutive relations for solids: an internal variable theory and its application to metal plasticity. *J. Mech. Phys. Solids*, 19, 433–455.

Roters, F., Rabbe, D. and Gottstein, G. (2000). Work hardening in heterogeneous alloys--- a microstructureal approach based on three internal state variables, *Acta Metall.*, 48, 4181.

Saimoto, S. (1989). Examination of the hart-li state variable parameters in terms of thermally activated dislocation --- defect interaction, In *Materials Architecture Proceedings of the Riso International Symposium on Metallurgy and Materials Science*, Riso Natl. Lab, 557-564.

Schroder, J. and Miehe, C. (1997). Aspects of computational rate-independent crystal plasticity. *Comp. Mater. Sci.*, 9, 168–176.

Sewell, M. J. (1967). On configuration-dependent loading, *Arch. Rat. Mech. Anal.*, 23, 327e351.

Sharon, E., Gross, S. P. and Fineberg, J. (1995). Local crack branching as a mechanism for instability in dynamic fracture, *Phys. Rev. Lett*., 74, 5146-5154.

Sharon, E., Gross, S. P. and Fineberg, J. (1996). Energy dissipation in dynamic fracture, *Phys. Rev. Lett.*, 76, 2117-2120.

Sharon, E., Gross, S. P. and Fineberg, J. (2002). Crack front waves and the dynamics of a rapidly moving crack, *Phys. Rev. Lett*., 88, 085503.

Shenoy, V. and Kim, K. S. (2003). Disorder effects in dynamic fragmentation of brittle materials, *J. Mech. Phys. Solids*, 51 2023–35.

Shi, Y., Hamstra, P., Mallory, R., MacEwen, S. R. and Wu, P. D. (2007). Numerical simulation of the pressure ram forming process, *J. Mater. Process. Technol.*, 182, 411–417.

Shi, Y., Wu, P. D. and Lloyd, D. J. (2012). Numerical analysis of surface roughening for aluminum tube under hydroforming based on crystal plasticity, In *Proceedings of 13th International Conference on Aluminum Alloys*, Pittsburgh, USA.

Shi, Y., Wu, P. D., Lloyd, D. H. and Embury, J. D. (2010). Crystal plasticity based analysis of localized necking in aluminum tube under internal pressure, *Eur. J. Mech. A/Solids*, 29 475e483.

Simo, J. and Hughes, T. (1998). *Computational inelasticity,* Springer-Verlag New York, inc. New York.

Simo, J. and Taylor, R. (1985). Consistent tangent operators for rate-independent elastoplasticity, *J. Comp. Methods in Applied Mech. & Eng.*, 48, 101-118.

Sorine, M., Simha, C. H. M., Van Riemsdijk, I. and Worswick, M. J. (2008). Prediction of necking of high strength steel tubes during hydroforming in multi-axial loading, *Int. J. Mech. Sci*. 50, 1411.

Storakers, B. (1971). Bifurcation and instability modes in thick-walled rigid-plastic cylinders under pressure, *J. Mech. Phys. Solids*, 19, 339e351.

Stoudt, M. R. and Ricker, R. E. (2002). The fundamental relationships between grain orientation, deformation-induced surface roughness and strain localization in an aluminum alloy, *Metall. Mater. Trans. A*, 33A, 2883-2889.

Tadmor, E. B. and Durban, D. (1995). Plastic deformation and burst of pressurized multilayered cylinders*, J. Press. Vessel Technology, Trans.* ASME 117, 85e91.

Taylor, G. I. (1938a). Analysis of plastic strain in a cubic crystal. *Stephen Timenoshenko 60th Aniversary Volume*, 218–224.

Taylor, G. I. (1938b). Plastic strain in metals, *J. Institute of Metals*, 62, 307–324.

Taylor, G. I. and Elam, C. F. (1923). The distortion of an aluminum crystal during a tensile test, *Proc. Royal Soc. London* A, 102, 643–667.

Taylor, G. I. and Elam, C. F. (1925). The plastic extension and fracture of aluminum single crystals. *Proc. Royal Soc. London A*, 108, 28–51.

Tomita, Y., Shindo, A. and Kitagawa, H. (1981). Bifurcation and post bifurcation behavior of internally pressurized elastic-plastic circular tubes under plane strain conditions, *Int. J. Mech. Sci.,* 23, 723e732.

Tugcu, P. (1995). Failure of internally pressurized cylindrical tubes for strain-rate dependent materials, *Int. J. Engng. Sci.,* 33, 1581e1594.

Tugcu, P. (1996). Inertial effects in ductile failure of cylindrical tubes under internal pressure, *Int. J. Impact Eng.,* 18, 539e563.

Tugcu, P., Neale, K. W., Wu, P. D. and Inal, K. (2004). Crystal plasticity simulation of the hydrostatic bulge test, *Int. J. Plasticity,* 20, 1603e1653.

Turkmen, H. S., Dawson, P. R. and Miller, M. P. (2002). The evolution of crystalline stresses of a ploycrystalline metal during cyclic loading, *Int. J. Plasticity*, 18, 941–969.

Tvergaard, V. (1990). Bifurcation in elastic-plastic tubes under internal pressure, *Eur. J. Mech. A/Solids,* 9, 21e35.

Varma, N. S. P., Narasimhan, R., Luo, A. A. and Sachdev, A. K. (2007). An analysis of localized necking in aluminum alloy tubes during hydroforming using a continuum damage model, *Int. J. Mech. Sci.,* 49, 200e209.

Verdier, M. and Matlock, D. (1992). Application of the bending-under-tension friction test to coated sheet steels, *J. Mater. Eng. and Performance,* 1, 685-693.

Weber, G. and Anand, L. (1990). Finite deformation constitutive equations and a time integration procedure for isotropic, hyperelastic-viscoplastic solids, *J. Comp. Methods in Applied Mech. & Eng*, 79, 173-202.

Wilson, D. V, Mirshams, A. R. and Roberts, W. T. (1983). An experimental study of the effect of sheet thickness and grain size on limit-strains in biaxial stretching, *Int. J. Mech. Sci.*, 25, 859-870.

Wilson, D. V., Roberts, W. T. and Rodrigues, P. M. B. (1981a). Effects of grain anisotropy on limit strains in biaxial stretching: part ii. sheets of cubic metals and alloys with well-developed preferred orientations, *Metall. Trans. A*, 12A, 1603-1611.

Wilson, D. V., Roberts, W. T. and Rodrigues, P. M. B. (1981b). Effect of grain anisotropy on limit strains in biaxial stretching: Part I. Influence of sheet thickness and grain size in weakly textured sheets, *Metall. Trans. A*, 12A, 1595-1602.

Wu, P. D. and Lloyd, D. J. (2003a). Modelling surface roughening with crystal plasticity, In *Proceedings of 1st Illinois Section of the Mathematical Association of America*, 15–20.

Wu, P. D. and Lloyd, D. J. (2004). Analysis of surface roughening in AA6111 automotive sheet, *Acta Mater.*, 52, 1785e1798.

Wu, P. D. and Lloyd, D. J. (2004a). Analysis of surface roughening in AA6111 automotive sheet, *Acta Mater*., 52 1785–1798.

Wu, P. D., Lloyd, D. J. and MacEwen, S. R. (2003b). A simple model describing roping in Al sheet, *Scripta Mater.*, 48, 1243–8.

Wu, P. D., Lloyd, D. J., Bosland, A., Jin, H. and MacEwen, S. R. (2003c). Analysis of roping in AA6111 automotive sheet, *Acta Mater.,* 51, 1945e1957.

Wu, P. D., Lloyd, D. J., Jain, M., Neale, K. W. and Huang, Y. (2007). Effects of spatial grain orientation distribution and initial surface topography on sheet metal necking, *Int. J. Plasticity* ,23, 1084e1104.

Wu, P. D., MacEwen, S. R., Lloyd, D. J. and Neale, K. W. (2004b). Effect of cube texture on sheet metal formability, *Mater. Sci. Eng*., A364, 182e187.

Wu, P. D., Neale, K. W. and Van der Giessen, E. (1996). Simulation of the behavior of FCC polycrystals during reversed torsion, *Int. J. Plasticity*, 12, 1199-1219.

Wu, P. D., Neale, K. W. and Van der Giessen, E. (1997). On crystal plasticity FLD analysis, *Proc. R. Soc.,* London A453, 1831e1848.

Xue, Z. and Hutchinson, J. W. (2007). Neck retardation and enhanced energy absorption in metal-elastomer bilayers, *Mech. Mater*, 39, 473-487.

Xue, Z., Vaziri, A. and Hutchinson, J. W. (2008), Material aspects of dynamic neck retardation, *J. Mech. Phys. Solids*, 56, 93-113.

Yoshida, K., Ishizaka, T., Kuroda, M. and Ikawa, S. (2007). The effects of texture on formability of aluminum alloy sheets, *Acta Mater.*, 55, 4499e4506.

Yoshida, K., Tadano, Y. and Kuroda, M. (2009). Improvement in formability of aluminum alloy sheet by enhancing geometrical hardening, *Comp. Mater. Sci.*, 46, 459e468.

Zhang, H. and Ravi-Chandar, K. (2006). On the dynamics of necking and fragmentation: I. Real-time and post-mortem observations in Al 6061-O, *Int. J. Fract.,* 142, 183–217.

Zhang, H. and Ravi-Chandar, K. (2008). On the dynamics of necking and fragmentation: II. Effect of material properties, geometrical constraints and absolute size, *Int. J. Fract.*, 150, 3–36.

Zhang, H., Liechti, K. M. and Ravi-Chandar, K. (2009). On the dynamics of localization and fragmentation: III. Effect of cladding with a polymer, *Int. J. Fract.,* 155, 101–18.

Zhuang, W., Wang, S., Lin, J., Balint, D. and Hartl, Ch. (2011). Experimental and numerical investigation of localized thinning in hydroforming of micro-tubes, *Eur. J. Mech. A/Solids*, 31 67e76.